

---

Martina Marchetti-Deschmann



TECHNISCHE  
UNIVERSITÄT  
WIEN  
Vienna University of Technology

## DIPLOMARBEIT

# Identifying proteins from the glue of the salamander *Plethodon shermani*

Ausgeführt am Institut für  
Chemische Technologien und Analytik  
der Technischen Universität Wien

unter Anleitung von  
Associate Prof. Mag. rer.nat. Dr.rer. nat. Martina Marchetti-Deschmann

durch  
**Max Kosok**  
Schleifmühlgasse 15/14, A-1040 Wien

14. 03. 2014, Wien

---

Max Kosok

# Abstract

---

As a defense mechanism, the salamander species *Plethodon shermani* secretes a sticky fluid to immobilize predators. Such biological glues work under a large variety of conditions and show a high bonding strength, therefore they are of interest to help developing new adhesive systems for industrial or medical applications. To understand the bioglue of *P. shermani*, its protein components were analyzed by means of peptide mass fingerprinting and peptide sequencing, using a matrix assisted laser desorption/ionization time-of-flight mass spectrometer. So far, the genome of *P. shermani* is not sequenced, therefore the protein identification was hampered. Nevertheless it could be shown by two-dimensional gel electrophoresis that the bioglue consists of a rather complex protein mixture and sample preparation indicated a high carbohydrate content.

Furthermore within this thesis a method for ion mobility mass spectrometry imaging was developed, which allows the differentiation of isobaric molecules and the characterization of various analyte species within just one experiment. This method will be used to directly analyze the glands within skin tissue of *P. shermani*, which are responsible for bioglue segregation. However, the gained lateral resolution of the developed ion mobility imaging method is at the moment not good enough to analyze the salamander skin glands, but it allowed to distinguish molecules of interest from matrix or background molecules as well as to differentiate between peptide and lipid species and therefore has a high potential to be further improved for other imaging experiments.

# Kurzfassung

---

Als Abwehrmechanismus scheidet der Salamander *Plethodon shermani* eine klebrige Flüssigkeit aus, um Angreifer bewegungsunfähig zu machen. Solche biologischen Klebstoffe funktionieren unter einer Vielzahl unterschiedlichster Bedingungen und verfügen über eine starke Bindungskraft. Daher sind sie für die Entwicklung neuartiger Klebstoffsysteme in der Industrie oder Medizin von Interesse. Die Proteinbestandteile des Bioklebstoffs des *P. shermani* wurden durch Peptidmassen-Fingerprinting und Peptidsequenzierung mit Hilfe eines Matrix-unterstützten Laser-Desorption/Ionisation Flugzeitmassenspektrometers untersucht. Das Genom des *P. shermani* wurde bis jetzt noch nicht sequenziert, wodurch die Proteinidentifizierung erschwert wurde. Nichtsdestotrotz konnte mit Hilfe von zweidimensionaler Gelelektrophorese gezeigt werden, dass der Biokleber aus einem komplexen Proteingemisch besteht. Des Weiteren deutete die Probenvorbereitung auf einen hohen Kohlehydratanteil hin.

In dieser Arbeit wurde ebenfalls eine Methode zur bildgebenden Ionenmobilitäts-Massenspektrometrie entwickelt, welche die Unterscheidung isobarer Moleküle, sowie die Charakterisierung verschiedener Analytklassen in nur einem Experiment ermöglicht. Mit Hilfe dieser Methode können die Hautdrüsen des *P. shermani*, welche für die Ausscheidung des Bioklebstoffes verantwortlich sind, direkt analysiert werden. Zurzeit ist die laterale Auflösung der entwickelten bildgebenden Ionenmobilitäts-Methode nicht fein genug um einzelne Hautdrüsen zu analysieren. Dennoch konnten Matrix-, bzw. Hintergrundmoleküle, sowie Peptide und Lipide unterschieden werden. Aufgrund dessen weist die entwickelte Methode ein hohes Potential zur Weiterentwicklung für kommende Experimente auf.

# Danksagung

---

An dieser Stelle möchte ich mich bei Professor Günter Allmaier für die Aufnahme in seine Arbeitsgruppe bedanken.

Ebenfalls danke ich auch meiner Betreuerin Martina Marchetti-Deschmann die es mir ermöglicht hat an diesem zum Teil vom FWF unterstützten Thema zu arbeiten. Ich weiß ihre tatkräftige Unterstützung trotz dichtgedrängten Terminplans, sowie die großen Freiheiten die sie mir bei dieser Arbeit gegeben hat, sehr zu schätzen.

Dr. Janek von Byern von der Universität Wien danke ich für die Bereitstellung der Proben und Unterstützung im Bereich der Biologie.

Der Firma Waters danke ich für die Gerätebereitstellung so wie die technische Unterstützung.

Natürlich möchte ich mich auch bei all meinen Freunden hier in Wien bedanken. Ihr habt mir eine super Studienzeit beschert, standet mir immer zur Seite und habt mich wenn nötig angetrieben und aufgemuntert. Ohne euch wäre ich heute vermutlich noch nicht soweit! Ebenso danke ich auch meiner Familie die während meiner gesamten Studienzeit zu mir hielt.

# Table of Contents

---

1	Introduction.....	1
1.1	<i>Plethodon shermani</i> .....	2
1.1.1	Data Available from Preceding Analyses.....	3
1.2	Aims of this Study.....	6
1.3	Gel-Electrophoresis.....	7
1.4	Mass Spectrometry.....	10
1.4.1	Matrix Assisted Laser Desorption/Ionization.....	11
1.4.2	Time-of-Flight Mass Analyzer.....	13
1.4.3	Tandem Mass Spectrometry.....	17
1.5	Protein/Peptide Identification using MALDI-MS.....	20
1.5.1	Peptide Mass Fingerprinting.....	21
1.5.2	Peptide Sequencing.....	23
1.6	Lipid Identification using MALDI-MS.....	24
1.7	Ion Mobility Mass Spectrometry.....	25
1.7.1	The MALDI Synapt G2 HDMS.....	28
1.8	MALDI Mass Spectrometry Imaging.....	34
2	Materials and Methods.....	36
2.1	Chemicals.....	36
2.2	Equipment / Instruments.....	40
2.3	Sample Collection.....	41
2.4	Protein Concentration – Bicinchonin Acid Assay (BCA).....	42
2.5	Protein Concentration – Bradford Assay.....	42
2.6	1D-PAGE.....	43
2.7	2D-PAGE.....	43

2.8	Silver Staining/Destaining .....	45
2.9	Enzymatic Digestion, Desalting and Preparation for MS .....	46
2.10	MALDI-TOF/TOF-MS for Protein Identification .....	47
2.10.1	Peptide Mass Fingerprinting .....	48
2.10.2	Peptide Sequencing .....	48
2.10.3	Data Analysis .....	48
2.11	MALDI – IM-MS Imaging.....	50
2.11.1	Evaluation of Ion Mobility Parameter .....	50
2.11.2	Sample Preparation for MALDI-IM-MS-Imaging .....	51
2.11.3	MALDI-IM-MS-Imaging Parameter .....	53
2.11.4	Data Analysis .....	53
3	Results and Discussion.....	55
3.1	Protein Analysis of Bioglue Samples Derived from <i>P. shermani</i> .....	55
3.1.1	Sample Preparation and Protein Concentration .....	55
3.1.2	1D-PAGE.....	64
3.1.3	2D-PAGE.....	69
3.1.4	Summary & Conclusion.....	81
3.2	MALDI – IM-MS Imaging .....	82
3.2.1	Evaluation of Ion Mobility Parameter .....	82
3.2.2	Ion Fragmentation coupled with IM Separation .....	93
3.2.3	Mass Sensitivity for Ion Mobility .....	101
3.2.4	IM-MS Imaging of Peptide/Lipid Standard.....	103
3.2.5	IM-MS Imaging of Bioglue .....	108
3.2.6	IM-MS Imaging of Tissue Samples .....	111
3.2.7	Summary & Conclusion.....	120
4	References.....	123

# 1 Introduction

Biological adhesives have played a major role in nature ever since. For over thousands of years plants, for example, developed strategies to heal wood defects and protect themselves against intrusion of parasites, while animals developed adhesive secrets as defense mechanism against predators or for hunting purposes (Keckes et al. 2003; Flammang 2006). Further do microorganisms or marine organism like mussels use adhesive materials for settlement, surface attachment and colonization (Lee et al. 2006; Flammang et al. 2009), while humans and other higher organisms use the inducible adhesive system of fibrinogen for wound healing (Berlind et al. 2010).

All of those many biological adhesive systems have the advantage over common technical adhesives of not needing any surface preparations or specific curing conditions. Some even work under humid condition or under water and are also able to bond with various types of surfaces without special activation, including materials like glass, plastic, metal and even Teflon (Graham et al. 2005; Rischka et al. 2010).

Those remarkable formations of adhesive systems by nature have recently drawn great attention to chemists and scientist as inspiration for biomimetic materials. The demand for biomimetic materials is growing each day, since they represent a potential for being renewable, have a lower impact on nature and being if necessary completely degradable or not (Lee et al. 2006).

The development of new adhesive systems is not only interesting for many areas of technology, but also for medical applications like wound healing in both soft and hard tissues. The currently used medical adhesives include mainly fibrin and cyanoacrylate which show on the one hand high bonding strength, but on the other hand major downsides as well. Fibrin for example bears the possibility of blood-borne disease transmission like hepatitis or HIV (Saltz et al. 1991), while cyanoacrylates can cause acute and chronic inflammation due to formaldehyde release upon degradation (Turß 1978; Tseng et al. 1990).

Therefore the aim is to gain detailed understanding of the features and mechanisms of biological adhesive systems, to develop new biomimetic/biocompatible adhesives.

## 1.1 *Plethodon shermani*

Up to now, marine organisms were the main focus of research on biological adhesive systems (Lee et al. 2006; Flammang et al. 2009), whereas for adhesive systems of terrestrial animals only some frog species reached attention in the recent years (Williams et al. 2000; Graham et al. 2006; Philips and Shine 2007; Tyler 2010). Studies on other amphibian are still rare, even though this class seems promising, since the secreted adhesive of the Australian frog genus *Notaden* reached bonding strength up to 2,8 MPa, which is among the strongest within the animal kingdom and comparable to industrial cyanoacrylates (Graham et al. 2005).

*Plethodon shermani* or the red-legged salamander is besides *Ambystoma* spp., *Batrachoseps* spp. and *Bolitoglossa* spp. one of the few North American salamander species which are reported to secrete adhesives as antipredator strategy (Brodie 1983). Apart from other defense strategies, the secretion of adhesive material has been demonstrated as effective (Brodie et al. 1969). When the salamander gets grabbed, for example, by a snake, it loops its tail and covers the snakes head with the sticky secret which hardens immediately and immobilizes the predator, upon which the salamander can escape (Arnold 1982).

The sticky secret of *P. shermani* is suggested by Largen and Woodley (2008) to be expressed by granular glands along the dorsal side of the tail, whereas granular glands along the ventral tail skin are responsible for scent making. Histological examination and staining with periodic acid Schiff base (PAS) indicated a neutral glycoprotein secretory product by dorsal granular glands, while on the ventral tail skin two types of granular glands could be identified. One, similar to the dorsal granular glands and a second one, marked as modified granular gland with a high carbohydrate content, which is indicated by strong staining with naphthol yellow and PAS (Figure 1). Further could mucous glands in both dorsal and ventral tail skin be identified, showing content of neutral and acidic carbohydrates by staining with PAS and Alcian Blue. It could not be determined, if those mucous glands contribute to the sticky secret. Largen and Woodley (2008) further performed a first gel electrophoretic analysis of the secreted glue by *P. shermani*, which revealed prominent bands at approx. 40kDa and 120kDa.

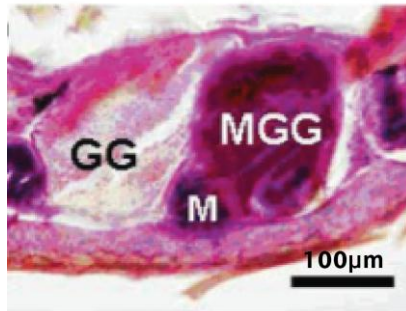


Figure 1: Naphthol yellow and PAS staining of ventral tail skin (*P. shermani*), showing two types of granular glands, quad stain. M = mucous gland, GG = granular gland, MGG = modified granular gland, FAT = fat deposit. Scale bars = 100  $\mu\text{m}$ .

Adapted from Largen and Woodley (2008)

Apart from this relatively recent study, only proteinaceous pheromones expressed by mental glands in several species of plethodontid salamanders have been characterized so far (Feldhoff et al. 1999)

### 1.1.1 Data Available from Preceding Analyses

Previous to this work studies regarding *P. shermani* and its adhesive secret were conducted and are to some part submitted to the Journal of Morphology under the title “Gluing to survive – Morphological characterization of the glue-producing system in the salamander *Plethodon shermani* (Caudata, Plethodontidae)” by von Byern and Grundwald (2012). In these studies the granular glands were measured to have an average length of 200-400  $\mu\text{m}$  in the dorsal and 90-150  $\mu\text{m}$  in the ventral tail skin. Mucous glands were determined to have an average length of 80-130  $\mu\text{m}$  on the dorsal and 20-50  $\mu\text{m}$  on the ventral side of the tail. It was also shown that the adhesive secret is not toxic using a LIVE/DEAD<sup>®</sup> Cell Viability Assay after cultivation of different cell types on foils with secreted glue for up to 7 days.

Furthermore, a first overview of low molecular weight molecules present in the bioglue was gained from unpublished data provided by Sophie Fröhlich<sup>1)</sup> using a matrix-assisted laser desorption/ionization – time-of-flight (MALDI-TOF) mass spectrometer (Axima TOF<sup>2</sup>; Shimadzu Biotech Kratos Analytical; Manchester, UK). Several molecules at approx. 2kDa,  $\approx 3.7$  kDa,  $\approx 5.9$ -6.5 kDa,  $\approx 9$  and 11 kDa could be observed (see Figure 2), as well as some lipids, which were identified based on high-energy collision induced dissociation (HE-CID) fragmentation (see Figure 3).

<sup>1)</sup>Institute of Chemical Technologies and Analytics, Technical University Vienna, Austria

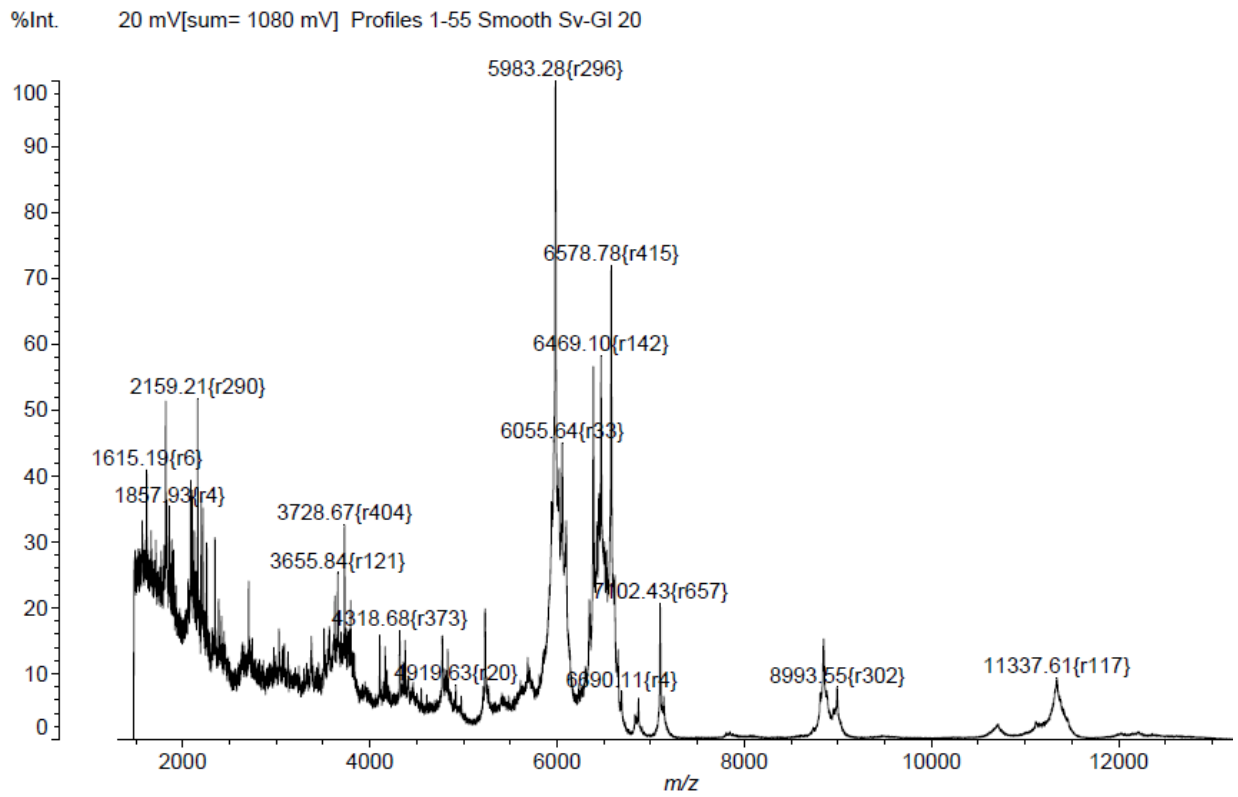


Figure 2: Molecules in the low molecular mass range (0-12 kDa) detected with a Shimadzu Biotech Kratos Analytical (Manchester, UK) Axima TOF<sup>2</sup> in linear mode, using 6 mg/ml  $\alpha$ -Cyano-4-hydroxycinnamic acid as matrix in acetonitrile / 0.1% trifluoroacetic acid (50/50) (unpublished data provided by Sophie Fröhlich<sup>1</sup>)

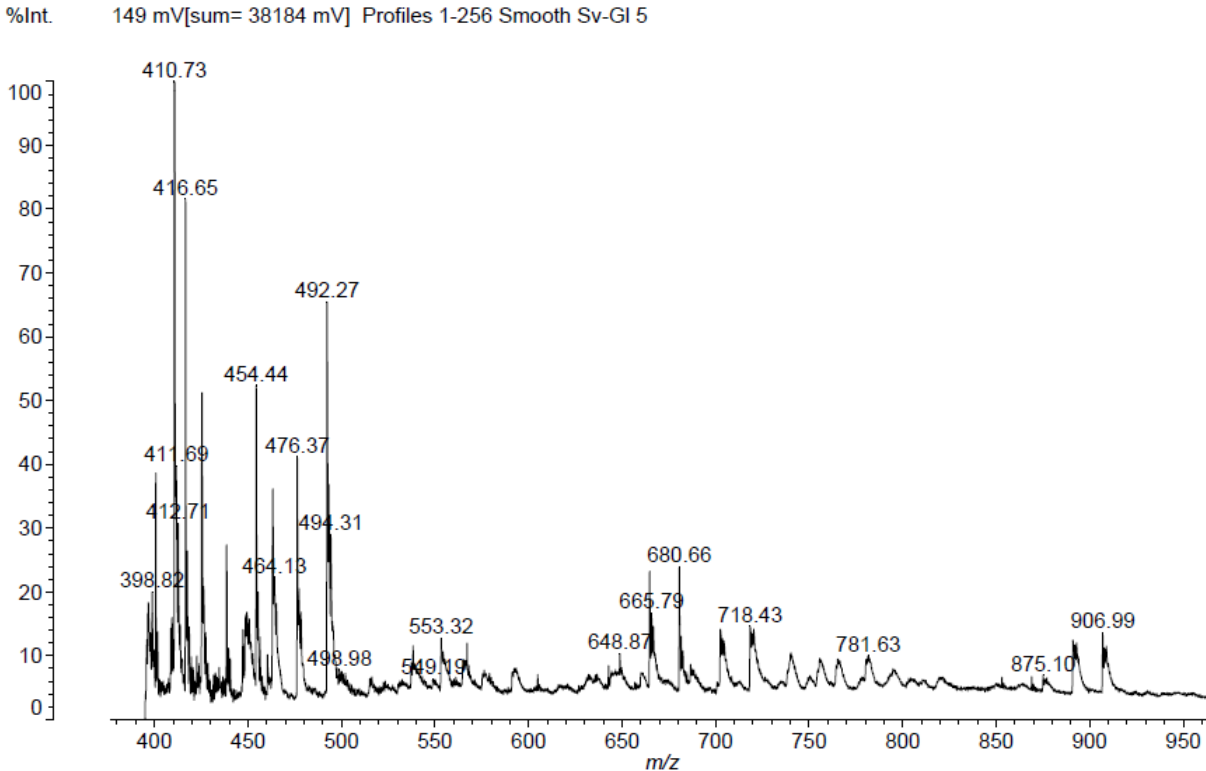


Figure 3: Using MALDI mass spectrometry various lipids were identified directly from the bioglue sample representing different lipid classes (e.g. PS, PE or Gyl-Cer) amongst which species with different side chain length (e.g. 6:0/6:0, 30:0/30:0, 18:0/24:0) were found. Lipids were identified by HE-CID. Samples were prepared with  $\alpha$ -Cyano-4-hydroxycinnamic acid as matrix in 2-propanol (6 mg/ml). Unpublished data was provided by Sophie Fröhlich<sup>1)</sup>

The total amino acid composition of the isolated glue was also analyzed by an external company (Institut Kuhlmann GmbH, Ludwigshafen am Rhein, Germany). This was done for bioglue sampled from several *P. Shermani* individuals living in captivity, as well as for bioglue from a different plethodontid species "*P. glutinosus*" for comparison. The analysis was performed according to SOP AS 03/04/05 and the results are shown in Table 1. Compared to *P. glutinosus*, the glue of *P. shermani* shows a lower concentration of aspartic acid and glutamic acid, the nonpolar/hydrophobic amino acids alanine and valine as well as the polar/neutral amino acid glycine. But *P. shermani* also shows an increased concentration of the amino acid histidine, as well as the presence of L-DOPA which is the precursor to some neurotransmitters.

Table 1: Amino acid composition of the secreted glue by *P. shermani* and *P. glutinosus*

Amino acid [g/100 g]	<i>P. shermani</i>	<i>P. glutinosus</i>
Aspartic acid	7,90	11,90
Threonine	5,01	5,77
Serine	4,27	4,37
Glutamic acid	8,32	17,90
Proline	4,17	7,91
Glycine	7,79	12,30
Alanine	3,32	10,50
Valine	5,68	11,60
Cysteine	0,54	0,70
Methionine	1,33	1,18
Isoleucine	4,21	6,96
Leucine	5,57	9,78
Tyrosine	4,45	7,29
Phenylalanine	4,14	7,62
Histidine	4,60	1,36
Tryptophan	1,35	--
Lysine	5,10	6,06
Arginine	2,78	2,50
L-DOPA	0.12	

## 1.2 Aims of this Study

To develop new biomimetic adhesives, biological sources can be used as model systems, for which the salamander *Plethodon shermani* was chosen in this work. However, a deeper understanding of the salamander glue's biochemical composition and its mechanical principles for highly effective bonding is needed.

The first step, which was handled by this work, is therefore to identify proteins present in the adhesive secret. To do so, a proteomics approach including gel-electrophoresis in combination with MALDI-TOF – mass spectrometry (MALDI-TOF-MS) was chosen.

The second part of this work was to systematically study the possibilities of ion mobility mass spectrometry and develop a method for MALDI – ion mobility – MS-Imaging, which could then be used to generate images displaying the lateral distribution of biomolecules, both proteins and lipids, in tissue samples of salamander glands.

### 1.3 Gel-Electrophoresis

Electrophoresis is described as a separation method, which uses the phenomenon that charged particles experience different mobilities in an electric field according to their mass, charge and molecule structure. It is an effective tool to separate proteins and enhance subsequent analysis.

Forces responsible for the movement of charged particles in the electric field are the acceleration- and friction-force. The acceleration-force is a function of the particles charge  $q$  and the electric field  $E$ , whereas the decelerating friction-force is a function of the migration velocity  $v$  and the friction-coefficient  $f_c$ . The friction-coefficient is further defined by the dynamic viscosity and if applicable the pore size of the medium as well as the Stokes radius of the hydrated ion. Forming an equilibrium, those two forces result in a constant velocity of a charged particle proportional to the applied electric field, whereas the proportionality factor  $u$  is defined as the electrophoretic mobility (Lottspeich and Engels 2009), (see equ. [1.1]).

$$v = \frac{q * E}{f_c} = u * E \quad [1.1]$$

The electrophoretic mobility of non-globular molecules can further be estimated in an empiric relation to the molecular mass  $M$  as shown in equation [1.2].

$$u \approx \frac{q}{M^{2/3}} \quad [1.2]$$

There are different realizations of this concept like discontinuous gel electrophoresis which was used in this work and is therefore described in detail.

Gel-electrophoresis is mostly carried out with agarose-gels or polyacrylamide-gels. While agarose is primarily used for separation of particles larger than 500 kDa, like DNA-fragments, polyacrylamide (PA) is used for proteins and smaller DNA-fragments, showing in this way the strongest resolving capacity. PA is an inert polymer and completely transparent with the major advantage of generating specific pore size gradients by means of controlled polymerization. Possible modifications for the use of PA gels include the use of charge suppressing additives in the sample buffer for the analyte molecules as well as the use of denaturing or non-denaturing buffer conditions during separation. During discontinuous gel electrophoresis, an electric current is applied for a certain time to generate an electric field which forces the analyte particle to migrate through the gel according to its mobility. The gels are usually embedded in a buffer system with separate anode and cathode buffer reservoirs. As a result of physical-, chemical-

and structural differences of the analytes, the gel configuration, buffer system and voltage or amperage have to be adapted to gain the best possible resolution.

In this thesis discontinuous sodium-dodecyl-sulfate – polyacrylamide – gel-electrophoresis (SDS-PAGE) introduced by Laemmli (1970) was used. SDS is a strong anionic detergent used for sample preparation prior to electrophoretic separation. By heating samples with an excess of SDS to 95 °C, it has the capability not only to form protein/SDS-micelles with a constant ration of 1.4 g SDS/g protein, but also to disintegrate tertiary and secondary structures by breaking hydrogen-bonds. Furthermore are disulfide-bonds between cysteine residues reduced by addition of dithiothreitol (DTT) or 2-mercaptoethanol, to completely unfold the proteins. By forming those micelles of linear proteins and SDS, a constant mass-to-charge ratio is generated, which results in protein separation by molecular weight only. The use of protein standards with a well-defined molecular mass and a SDS-PAGE containing 0.1% SDS allows to draw a linear correlation of the protein's migration distance in the gel to the common logarithm of the molecular masses and therefore to determine molecular masses of analyte molecules in question.

To maintain protein solubility, which is a requirement for electrophoretic separation, iodoacetamide (IAA) is often added after reduction of the disulfide-bonds. IAA acts as alkylation reagent and prevents reformation of disulfide-bonds at the cysteine residues by carbamidomethylation. Another approach to enhance solubility, especially for hydrophobic proteins, is to use detergents like CHAPS or chaotropic agents like urea. However, the latter one degrades upon heating to iso-cyanate which can then covalently modify protein N-termini or  $\epsilon$ -amines of lysine under basic conditions, resulting in possible carbamylation (Kollipara and Zahedi 2013). Besides this introduced protein modifications, other variable protein modifications like N-terminal acetylation or oxidation of methionine can occur during the process of sample analysis and have to be taken into account for subsequent evaluation.

SDS-PAGE can also be deployed in a 2-dimensional way (2D-SDS-PAGE). Hereby isoelectric focusing (IEF) of the analyte molecules is performed as a first dimension before separation of analytes according to their molecular mass, being the second dimension. IEF is also an electrophoretic separation method liable to the same principles as described earlier. The principle of separation for this method is that the migration of proteins/peptides in an electric

field applied to a medium (e.g. PA gels) with a pH-gradient, occurs according to their isoelectric points (pIs).

The pI of a molecule is defined as the pH at which its net electric charge is zero. The net electric charge of a molecule is the sum of all its allocated positive and negative charges. In case of proteins or peptides, three dimensional conformation and post-translational modifications like phosphorylations or glycosylations play a critical role as well. If molecules are separated in a pH-gradient by applying an electric field, they migrate until they reach their respective pIs. At this point the net charge is zero and further migration is no longer possible. This electrophoretic separation method is time independent and proteins are not only kept at the specific location of their pIs on the gel, but are also focused and therefore concentrated.

The resolving power of IEF is defined as  $\Delta pI$  in equation [1.3] and represents the minimal pH difference at which two neighboring proteins can still be separated with a given medium and electric field  $E$ . The medium is thereby defined by its diffusion coefficient  $D$  and its pH gradient  $d(pH/dx)$  whereas  $du/d(pH)$  describes the mobility gradient of a protein at its pI (Lottspeich and Engels 2009).

$$\Delta pI = \sqrt{\frac{D[d(pH)/dx]}{E[-du/d(pH)]}} \quad [1.3]$$

The required pH gradient can be realized in various ways. In this work an immobilized-pH-gradient (IPG) was used. It shows a relatively stable pH-gradient and a larger loading capacity compared to a carrier ampholyte pH gradient (Wilkins et al. 1997). IPGs are also quite commonly used in 2D-SDS-PAGE. It consists of a PA gel matrix which is co-polymerized with so called *Immobilines* which are acrylamide derivatives as illustrated in Figure 4. The residue, R, consists of buffering groups like carboxy- or tertiary-amino-groups. Therefore *Immobilines* are either weak acids or weak bases. By creating a continuous variation of the ratio of basic and acidic *Immobilines* in the matrix, IPG-strips for IEF can be generated (Bjellqvist et al. 1982).

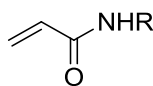


Figure 4: Structure of *Immobilines*

After isoelectric focusing which represents the first dimension, where the analyte molecules are separated in the IPG-strip according to their pI, subsequent separation by SDS-PAGE concludes in a second dimension.

After effective protein separation by gel-electrophoresis, the proteins have to be visualized. Generally this is gained by covalent or non-covalent interactions between a reagent and the analyte molecule. This visualization reagent has to have a higher binding affinity to the protein than to the gel molecules, it should be sensitive in detection, have a wide dynamic range, should be easy to use, non-toxic, environment friendly and compatible to subsequent analysis (Winkler et al. 2007). There are various well-established pre- and post-staining methods available, which either use UV/Vis- or fluorescence-dyes.

Silver staining with silver nitrate was the method of choice for this thesis (Shevchenko et al. 1996). It is a sensitive non-covalent post-staining method with a limit of detection (LOD) of approx. 0.5 ng for BSA (bovine serum albumin) and in the used way it has the advantage of compatibility with subsequent MS analysis, which will be described in the following chapter.

## 1.4 Mass Spectrometry

Mass spectrometry is an analytical technique to separate ions in a high-vacuum according to their mass-to-charge ratio and determine their molecule masses.

In principle MS instruments consist of three modules, an ion source to produce gas-phase ions of sample molecules, a mass analyzer which separates the ions according to their mass-to-charge ratio ( $m/z$ ) and a detector to indicate the ions separated by the mass analyzer (Figure 5).



Figure 5: Scheme of a mass spectrometer; dark blue indicates the main modules

As said, the ion source generates ions from sample molecules. This is necessary because only charged molecules can be separated in an electric- or electromagnetic-field. The ionization technique is a key part and determines what sample type can be analyzed. There are two distinctive kinds of ionization techniques, hard- and soft-ionization, differing in the used energy levels to transfer the charge on the molecules. For biological samples, soft-ionization methods like electrospray ionization (ESI) and MALDI are most common. In chapter 1.4.1 the latter is described in more detail. The use of high-vacuum at the ion-source is preferred due to a better ion transfer into the mass analyzer, however it is optional and its implementation depends on the type of instrument in use. Nevertheless a sample-injection-system to insert the sample from the ion source to the mass analyzer and thus into high vacuum is obligatory as ion separation occurs best at  $10^{-5}$  to  $10^{-8}$  mbar or lower. This maximizes the mean free length of path of ions

for high mass resolution and minimizes the collisions with gas molecules to reduce unwanted fragmentations.

There are different possibilities of ion separation like determination of flight time in a field-free flight region. Instruments using this separation technique are known as a time-of-flight (TOF) mass analyzer and will be described in chapter 1.4.2. Such instruments were used in this work since they can be combined with ESI or MALDI to analyze biomolecules like peptides, proteins or lipids resulting in high sensitivity, excellent mass accuracy and resolution.

The final element of the MS-instrument is the detector. It either records the induced charge or produced current when an ion passes or hits the detector. The most commonly used detectors are secondary-electron-multiplier or micro-channel plate detectors (MCP).

#### 1.4.1 Matrix Assisted Laser Desorption/Ionization

MALDI is a soft desorption/ionization method to measure intact, non-fragmented molecule ions from a condensed phase, especially biomolecules and large organic molecules (Karas et al. 1989). This is accomplished by exposing the sample to a pulsed laser beam, whereas pulsed monochromatic ultraviolet (UV) or infrared (IR) lasers are usually used, while the addition of matrix substances, which have the ability to almost completely absorb the laser energy, supports desorption and ionization (Gross and Strupat 1998).

The matrix is mixed with the analyte molecules in a molar excess of 1:1 000 to 1:10 000. By evaporation of the solvent, the analyte molecules not only just co-crystallize with the matrix, but the high molar excess of matrix also leads to singularized molecules (analyte molecules completely surrounded by matrix molecules) and therefore reduces interactions between individual analyte molecules. The incorporation of analyte molecules into the matrix's Bravais lattice is a basic requirement for efficient desorption/ionization (Kaufmann 1995).

There are several theories about the desorption- and ionization-process (Dreisewerd 2003; Karas and Krüger 2003). Most likely the matrix absorbs the laser energy with its  $\pi$ -electron system. The stored energy then relaxes into the lattice system which leads to strong disturbances and dilatations. Thereby an explosive desorption from parts of the crystal surface occurs, which leads to a phase transition. Apparently the stimulating energy for this process can be low enough that even thermal unstable molecules survive without fragmentation. By this event, matrix is ionized by the addition of a proton. It is then hypothesized, that the proton is transferred to the analyte molecule, generating most likely a single protonated quasi-molecular

ion  $[M+H]^+$ . Multi protonation ( $[M+nH]^{n+}$ ) or the addition of sodium (forming  $[M+Na]^+$ ) or potassium (forming  $[M+K]^+$ ) can occur as well. The, by this way generated ions in the gas phase, are then accelerated by an electrostatic field towards the mass analyzer (Kaufmann 1995; Stults 1995; Mann and Talbo 1996; Gross and Strupat 1998; Lottspeich and Engels 2009). Figure 6 illustrates the schematic process of desorption and ionization.

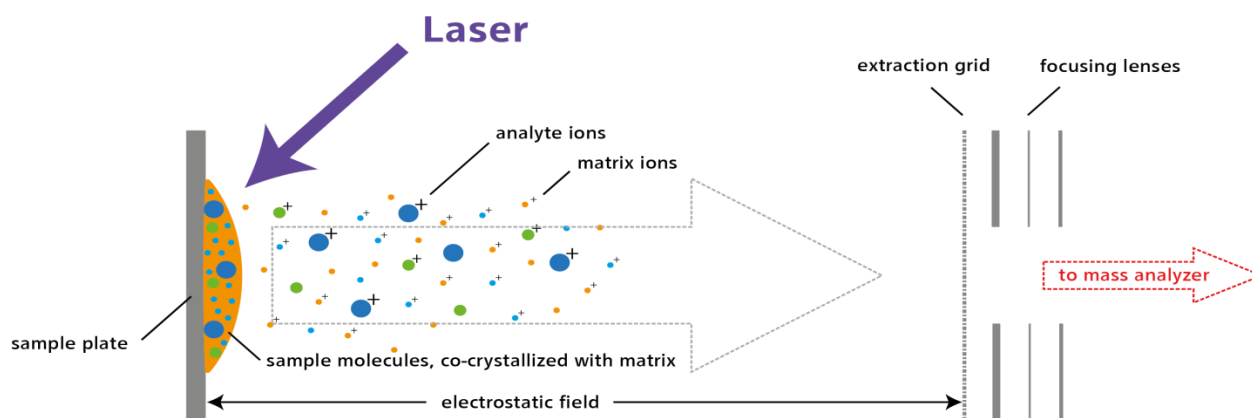


Figure 6: Schematic process of desorption and ionization in a MALDI ion source

Small organic molecules are used as matrix systems. For good absorbance they usually possess  $\pi$ -electron systems which consist mostly of aromatic compounds and further conjugated double bounds. Commonly used matrixes are  $\alpha$ -cyano-4-hydroxycinnamic acid ( $\alpha$ -CHCA), 3,5-dimethoxy-4-hydroxycinnamic acid (sinapinic acid, SA) or 2,5-dihydroxybenzoic acid (DHB) which structures are illustrated in Figure 7.

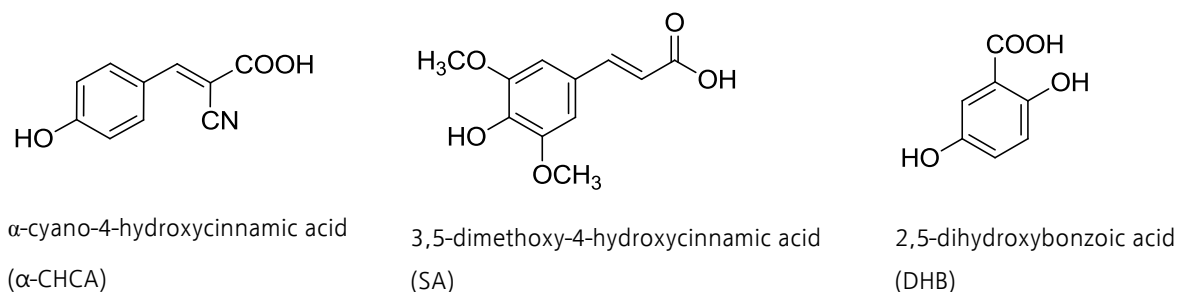


Figure 7: Three common MALDI matrix substances;  $\alpha$ -CHCA, SA and DHB

For these matrices MALDI typically uses UV lasers such as ND:YAG-lasers (neodymium-doped yttrium-aluminum-garnet,  $Nd:Y_3Al_5O_{12}$ ) for wavelengths of 266 nm or 355 nm as well as nitrogen lasers for a wavelength of 337 nm (Lottspeich and Engels 2009). UV laser are preferred for proteomics, since their shorter wave length results in higher sensitivity and longer

sample life, while IR laser like manually Q-switched Erbium-YAG laser for wavelengths of 2.94  $\mu\text{m}$  are preferred for large oligonucleotide analyses whereas different matrices are necessary as well (Overberg et al. 1990; Cha et al. 2007).

### 1.4.2 Time-of-Flight Mass Analyzer

TOF mass analyzers separate the analyte ions after an initial acceleration from the ion source towards the separation zone, according to their velocity in a high-vacuum field-free flight region, which will further be referred to as flight tube. This is possible since the acceleration of the analyte ions occurs in a constant electrostatic field, thus receiving all the same kinetic energy. The determination of the  $m/z$  itself is based on the exact electronic measurement of the time an ion needs to pass the distance of the flight tube. This concept is based on the following equations (equ. [1.4] – [1.6]) and the basic layout of a TOF-mass analyzer is illustrated in Figure 8.

An electrostatic field with the constant acceleration voltage  $U$  transfers kinetic energy  $E_{kin}$  onto the analyte ions depending on their charge  $q$ . The transfer of kinetic energy results in different velocities  $v$  depending on the ions mass  $m$ . The ions charge  $q$  can also be expressed as the quantity  $z$  of elementary charges  $e$  (equ. [1.4]). The velocity is on the other hand defined as the time  $t$  it takes for a molecule to cover the distance  $L$  (equ. [1.5]). Therefore with a constant acceleration voltage and a known length of the field-free flight distance,  $m/z$  values of analyte molecules can be calculated by measuring the exact flight time (see equ.[1.6]). This also means, that the  $m/z$  of an analyte ion is proportional to the square of its flight time (Wiley and McLaren 1955; Lottspeich and Engels 2009).

$$E_{kin} = \frac{1}{2} * m * v^2 = z * e * U \quad [1.4]$$

$$v = \frac{L}{t} \quad [1.5]$$

$$\frac{m}{z} = \frac{2 * e * U}{L^2} t^2 \quad [1.6]$$

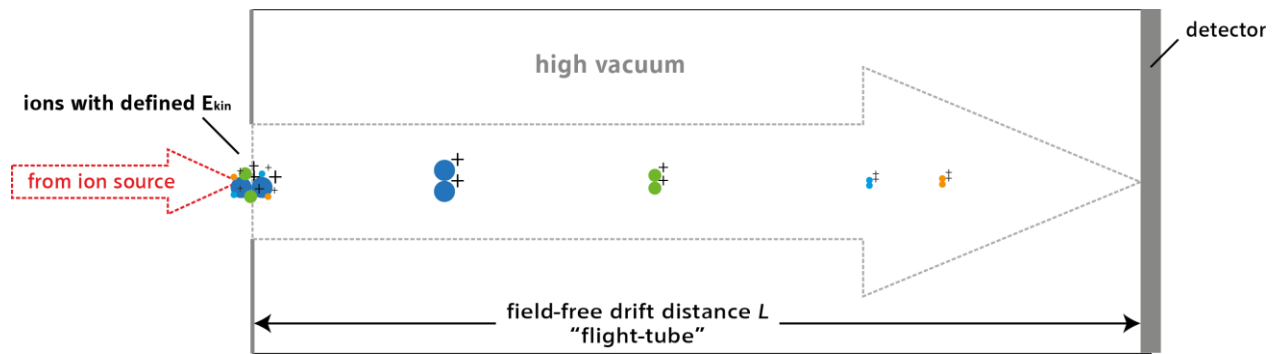


Figure 8: Scheme of a linear TOF-mass analyzer

Due to the explosive desorption process in the MALDI ion source as well as place and time delayed desorption/ionization based on crystallization variances, there is no discrete kinetic energy distribution for ions with the same  $m/z$  after constant acceleration, but rather a Gaussian distribution. This energy uncertainty leads to broadening of the detected signal, plotted as a peak.

Therefore mass resolution  $R$  is an important characteristic of mass analyzers. It is the ability to detect two ions differing only by a small mass difference separately. Mass resolution is defined as the quotient of the ions mass  $m$  and the mass difference  $\Delta m$  to the next still separately detectable ion (equ. [1.7]).

$$R = \frac{m}{\Delta m} = \frac{m_1}{m_2 - m_1} \quad [1.7]$$

For this definition the peak maxima of two peaks have to be exactly determined. However, for TOF-instruments this definition is not suitable as two neighboring peaks are essential but not always available. So  $\Delta m$  is deduced as full width at half maximum (FWHM, see Figure 9). Unfortunately this does not necessarily mean that a mono-isotopic separation can be accomplished (Lottspeich and Engels 2009). For example with a mass resolution of  $R=1\,000$ , the mass of  $1\,000$  and  $1\,001$  cannot be separated, since both peaks overlap each other at their half width (see Figure 10). Nowadays TOF mass analyzers reach resolutions of  $40\,000$  and higher.

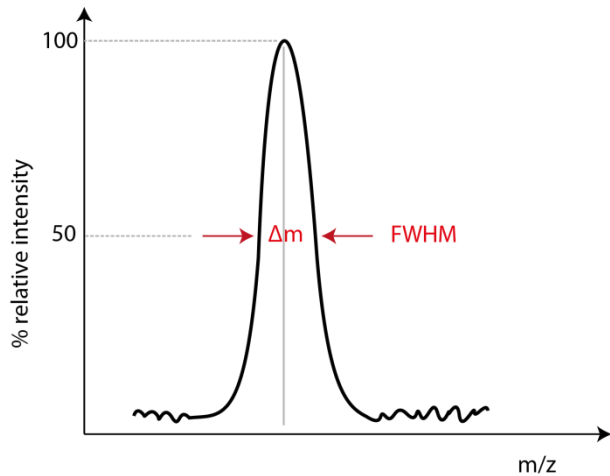


Figure 9: Definition of FWHM, scheme taken from Lottspeich and Engels (2009)

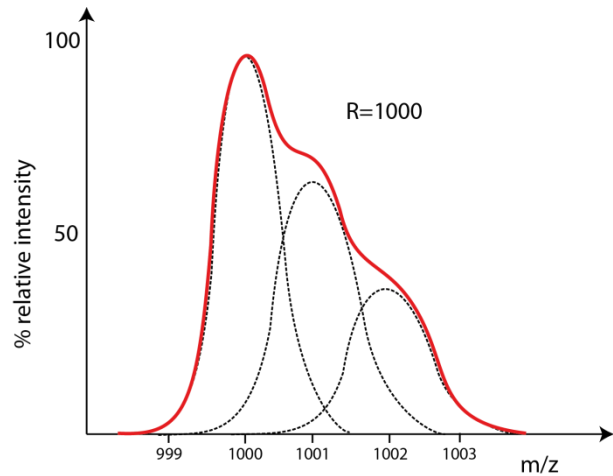


Figure 10: Exemplary isotope pattern of  $m/z=1000$  for a mass resolution  $R=1000$ , scheme taken from Lottspeich and Engels (2009)

To enhance mass resolution of TOF instruments, pulsed or rather delayed extraction can be used, as well as different instrument configurations like a reflectron TOF (RTOF) or even orthogonal acceleration RTOF (see chapter 1.7.1).

### Delayed extraction

As described earlier, a constantly applied electrostatic acceleration field results in a rather broad energy distribution for ions with the same  $m/z$  due to various effects during desorption/ionization. To minimize the energy distribution, the onset of the electric field responsible for the acceleration of the ions into the flight tube is delayed to the MALDI laser pulse for ionization and desorption. This way, ions which experience a higher forward momentum due to the ionization/desorption event and therefore have already spread further towards the flight tube, start to be accelerated at a lower potential. Conversely ions with lower forward momentum are accelerated at a higher potential when the extraction field is turned on. So after delayed extraction these ions enter the flight tube with higher velocity and therefore are able to catch up with ions started with higher momentum. With properly adjusted ion source parameters, ions of different kinetic energy but same  $m/z$  can be detected at the same time, resulting in an improving mass resolution (Brown and Lennon 1995; Lottspeich and Engels 2009).

## Reflectron TOF

Instrument configuration in reflectron mode is another way to improve mass resolution. The principle setup is illustrated in Figure 11. The characteristics of this setup are lenses at the end of the field-free drift region, which deploy a retarding electric field. Those lenses are referred to as reflector or ion mirror, since they deflect the ions back towards the flight tube in a slightly changed angle. Consequently the detector has to be located at the source side of the mirror, to detect the reflected ions.

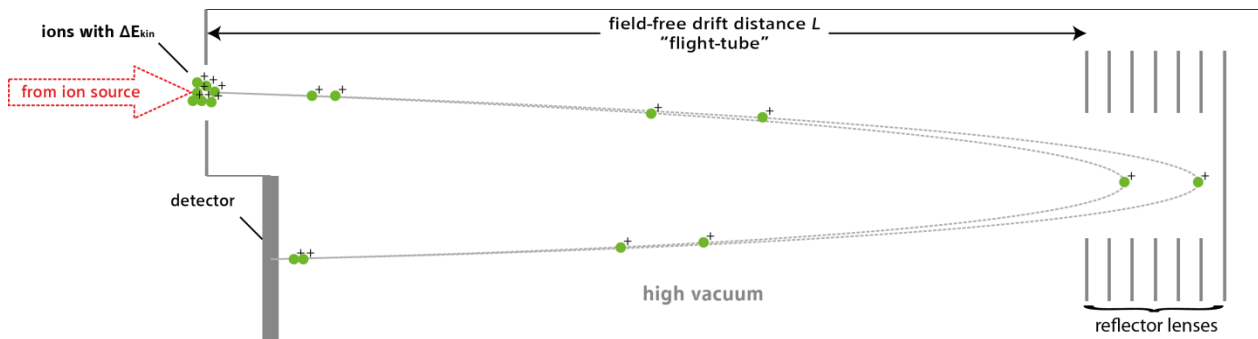


Figure 11: Principle setup of R-TOF mass analyzers

This setup also enables the reduction of kinetic energy distribution. Ions with a higher kinetic energy penetrate deeper into the retarding electric field of the reflector than ions with the same  $m/z$  ratio but lower kinetic energy. Consequently this means faster ions with a longer flight path and slower ions of the same  $m/z$  with a shorter flight path, reach the detector at the same time. Besides minimizing the energy uncertainty for given  $m/z$  ratios, this instrument setup also extends the length of the field-free drift region. A longer flight path means a more significant time difference for ions with similar velocities, thus an improvement in mass resolution is accomplished as well. Unfortunately it has to be taken into account that RTOF instruments cannot detect the whole  $m/z$  range since the reflector can only cover certain kinetic energies and instrument sensitivity also decreases with the use of a reflector due to transmission loss of ions (Wiley and McLaren 1955; Mamyrin 2001; Lottspeich and Engels 2009). To improve the performance of the ion mirror, a dual-stage reflectron is proposed. It consists of two subsequent homogeneous electric fields with a different potential. The first potential is responsible for a strong deceleration and the second potential imposes a weaker electric field for better separation. Dual-stage reflectrons are more compact and have an improved homogeneity of the electric field (Cotter et al. 2007; de Hoffmann and Stroobant 2007).

Other commercially available implementations of RTOF instruments like the Curved Field Reflectron (CFR) by Shimadzu will be further described in the next chapter.

### 1.4.3 Tandem Mass Spectrometry

Tandem Mass Spectrometry or MS/MS is a method which involves analyte fragmentation and the implementation of two subsequent mass analyzers.

Fragmentation of analyte ions can result from high energy transfer by means of the MALDI laser during the desorption/ionization process, which creates metastable ions with a short half-life time. Since fragmentation helps to identify the analyte ion, it also can be caused within a collision-cell and is known as collision-induced dissociation (CID). For information on identification by means of fragmentation see chapter 1.5.2 and 1.6.

If the lifetime of an ion is shorter than its time spent in the ion source, all product ions are accelerated with the same kinetic energy and can be detected independently from the type of mass analyzer. This kind of fragmentation is known as in-source decay (ISD) and occurs all the time during MALDI-MS. If the lifetime of an ion is longer than its time in the source, but shorter than its flight time in the field free drift region, the fragmentation is called post-source decay (PSD). Since the fragmentation occurs in the field-free region, all product ions have the same velocity as their precursor ion and thus cannot be distinguished with linear TOF mass analyzers (see Figure 12/a). This is where the instrumental setup of a tandem mass spectrometer comes into play. The first mass analyzer is used to select a specific precursor ion and the second mass analyzer to separate the product ions (de Hoffmann and Stroobant 2007). For this setup, different mass analyzer can be implemented like a in following more detail described TOF/RTOF instrument, or for example a quadrupole/orthogonal acceleration RTOF instrument (see 1.7.1).

The selection of the precursor ion in the first mass analyzer allows assigning its product ions. This is accomplished by application of a blocking potential on a mass selection gate, which is only cut off for a short time corresponding to the flight time of the desired precursor ion. By using two succeeding gates, the resolution is increased. Hereby the first gate is used to cut-off the faster ions and the second gate is used to cut off the slower ions. A Bradbury-Nielsen shutter, another type of ion gate, can also be used. The precursor ion and the product ions are always selected together, since they have the same flight time. The position of the mass selection gates within the first TOF mass analyzer is therefore variable. It can be located after

the collision cell like in the TOF/RTOF instruments by Bruker Daltonics as illustrated in Figure 13/a or before the collision cell, which minimizes loss from low angle scattering (Figure 13/b/c).

As described previously, all product ions possess the same velocity as their precursor, but in order to fulfill equation [1.4] they have different kinetic energies. This fact can be used to separate the product ions with the use of a RTOF, which also focuses the ions at the same time. Here again ions with different kinetic energy spend different time in the reflecting field of the ion mirror and therefore reach the detector at different times according to their  $m/z$  ratio (see Figure 12/b).

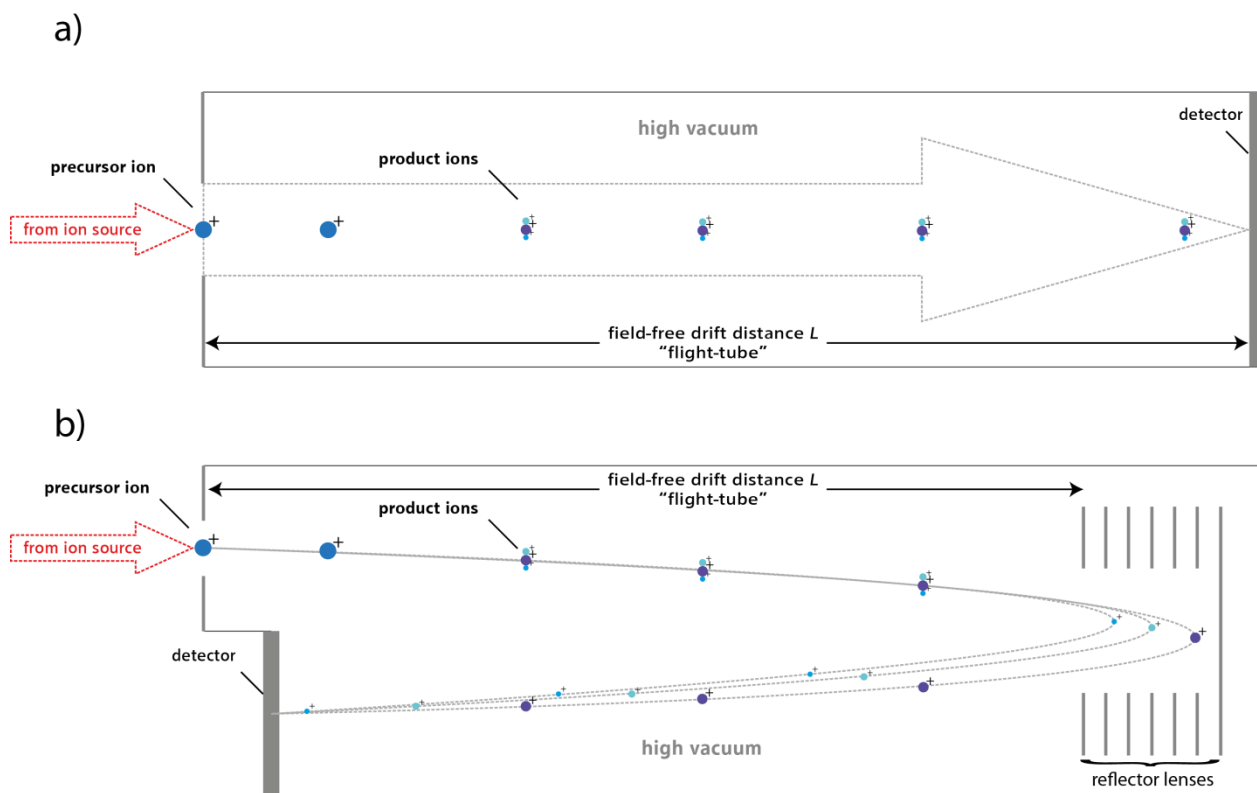


Figure 12: Behavior of product ions after fragmentation in a) linear TOF or b) R TOF

Unfortunately, product ions have a wide spread of kinetic energy, which lies well outside the range of ion mirrors with a linear retarding field. Since not the full kinetic energy range can be covered, the potential at the reflector has to be adapted stepwise and thus the recorded spectra have to be summed-up to observe the entire mass range of the product ions. This necessity wastes precious sample, consumes a lot of time and complicates the calibration process (Cotter et al. 2007; de Hoffmann and Stroobant 2007). One solution to solve this

problem is to extract and accelerate the ions orthogonally to the first mass analyzer, which results in a new, closer kinetic energy distribution (for instrument setup see chapter 1.7.1). Another approach is to raise the kinetic energy of the product ions by re-acceleration before they enter the second reflectron. This setup is implemented by Bruker Daltonics and Applied BioSystems (see Figure 13/a/b). Bruker Daltonics applies an 8 keV potential for acceleration of the precursor ion in the first TOF mass analyzer, where it also can be fragmented by means of CID if desired. After ion selection, the product ions enter a so called "LIFT" cell, where they are accelerated to a kinetic energy range of 15-23 keV and enter the second mass analyzer, the RTOF with a constant electric field. Applied BioSystems accelerates its precursor ions to 20 keV and positions its ion selector and subsequent deceleration lenses before the collision cell. Hereby collision energy is limited to approx. 1 keV. The product ions then enter a second ion source with lenses for re-acceleration and refocusing by pulsed extraction, which also leads to a narrow spread of kinetic energy.

Shimadzu developed another method to solve this problem (see Figure 13/c). They deploy a non-linear, or rather a curved electric field, at their reflectron of the second mass analyzer, which allows to cover the whole range of kinetic energy and to reflect all product ions without deceleration or re-acceleration. This also enables the use of collision energies of up to 20keV and subsequent measurement of fragment ions of rather low energies.

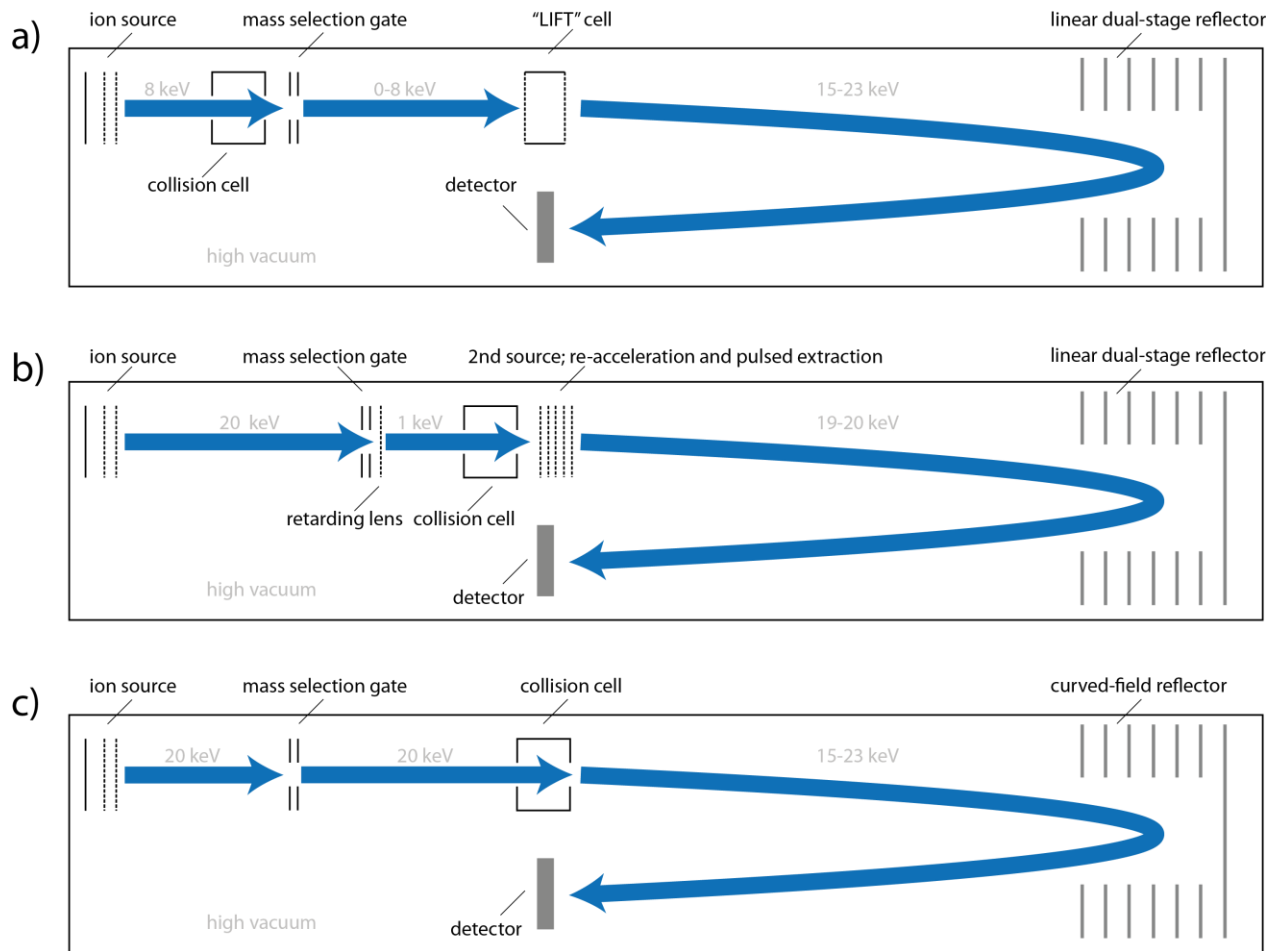


Figure 13: Schematic setup of TOF/RTOF instruments on the basis of Cotter et al. (2007): a) Bruker Daltonics, b) Applied BioSystems, c) Shimadzu

## 1.5 Protein/Peptide Identification using MALDI-MS

MALDI-MS is besides liquid chromatography – ESI-MS (LC-ESI-MS) a widely used technique to identify proteins or peptides. There are two strategies used for both, LC-ESI-MS and MALDI-MS (see Figure 14)

One is described as Top-Down approach, in which the intact protein is analyzed, resulting not only in information about its total molecular weight (MW), but in combination with analyte fragmentation also results in information on the protein's primary structure and modifications. Unfortunately this approach deals with some major difficulties like the introduction of large intact proteins into the gas-phase and the lack of extensive fragmentation for sufficient structure information using generally available fragmentation techniques, i.e. the collision with inert gas molecules.

The second, more commonly used method is described as Bottom-Up approach. Hereby, prior to mass analysis, the intact protein is cleaved into smaller peptides by proteolytic or chemical cleavage, resulting in smaller molecules which can be transferred into the gas-phase more easily. Besides information on the MW of the peptides, here again peptides can be further fragmented by means of MS/MS resulting in sometimes even complete sequence information (Aebersold and Mann 2003; Chait 2006) (see Figure 14).

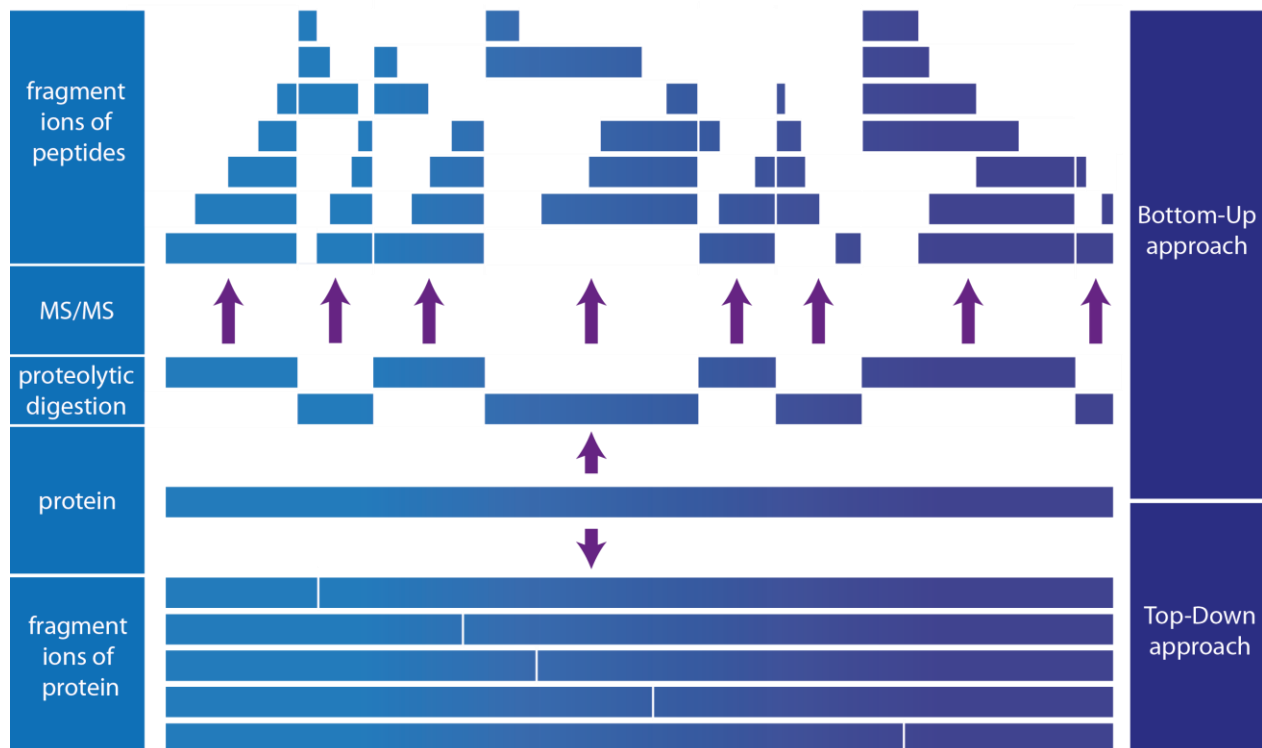


Figure 14: Bottom-Up and Top-Down approaches

The Bottom-Up approach was used in this thesis, hereby the first step of determining protein specific peptide masses is also known as “Peptide Mass Fingerprinting”.

### 1.5.1 Peptide Mass Fingerprinting

Peptide Mass Fingerprinting (PMF) is an effective tool to identify proteins after specific cleavage by means of database comparison. Since it often fails to identify protein mixtures, it usually includes protein purification by liquid chromatography or like in this thesis, electrophoresis. Specific cleavage can be chemical degradation using mild acids or cyanogen bromide or a proteolytic degradation using specific enzymes. Proteolytic digestion can be either carried out in solution or directly in the PA gel after electrophoresis (in-gel digestion). For digestion, enzymes like Chymotrypsin, LysC, proteinase K or trypsin, the most common one, can be used.

Trypsin, which is also used in this work, is a serine protease, which cleaves peptide bonds at the C-termini of lysine or arginine (see Figure 15) except if either is followed by proline. Lysine and arginine are not so frequently occurring amino acids and therefore trypsin generates a very specific peptide pattern with not too small peptides. This protein specific peptide pattern acts like a protein's fingerprint and helps during identification.

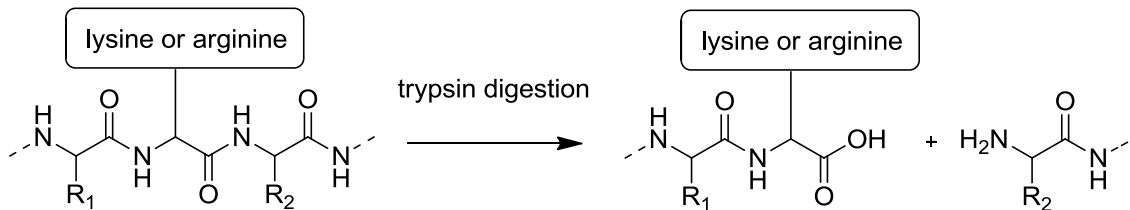


Figure 15: Protein cleavage by trypsin

To retrieve sufficient cleavage, proteins have to be denaturated prior to digestion, since secondary and tertiary structures hamper enzymatic activity by steric hindrance of cleavage sites. As described in chapter 1.3, disulfide-bonds are cleaved by reduction with DTT or 2-mercaptoethanol and further alkylated using IAA to prevent reformation.

After successful protein digestion, the MW of the specific peptides is investigated by means of MS. Due to its high mass accuracy, a high resolution RTOF instrument (see chapter 1.4.2) was chosen in this work to generate a mass list of peptide masses belonging to a protein which can be compared to theoretical peptide masses retrieved from *in-silico* digestion of proteins stored in databases like NCBI (http://www.ncbi.nlm.nih.gov/) or UniProt (Leinonen et al. 2004). The comparison can occur in an automated way by using freely accessible, web-based search engines like Mascot (Koenig et al. 2008). Such search engines allow the definition of specific search parameters to restrict the search and increase the significance of its results. Those parameters usually include the cleavage enzyme and its expected number of missed cleavages. Also fixed and variable modifications can be specified (Perkins et al. 1999), those are biological relevant, like phosphorylations, or occur during sample preparations, like oxidation (methionine) or protein N-terminal acetylation. If IAA was used, fixed modification of carbamidomethylation at cysteine has to be taken into account and for the use of urea or thiourea a variable modification of carbamylation at lysine or the protein N-terminus is usually considered (see chapter 1.3). Another important parameter to increase the significance of search results is to specify the analyte's taxonomy as well as the peptide mass tolerance. This way a high probability to identify proteins by comparing experimentally retrieved peptide

masses with *in-silico* digested peptide masses from database entries is achieved. However, this method is restricted to proteins already mentioned in the database, or which can be translated from known genomes or transcriptomes. Furthermore there is the likeliness of false-positive protein identification due to multiple protein samples or the presence of contaminations. Therefore corresponding peptides have to be sequenced to acknowledge positive search results.

### 1.5.2 Peptide Sequencing

As mentioned previously, the peptides from proteolytic digestion can be further analyzed by fragmentation within the mass analyzer using PSD or CID experiments (see 1.4.3). The fragmentation of a selected precursor ion (peptide) occurs at specific locations of the peptide backbone and amino acid side chains, which allows deducing the peptide's amino acid sequence and possible modifications. The preferred site of fragmentation depends on the energy transferred to the peptide. Biemann et al. (1966) and Roepstorff and Fohlman (1984) defined a fragmentation nomenclature, which is illustrated in Figure 16. At the peptide backbone, cleavage can occur at three different positions, between the  $C_\alpha$ -C, the C-N and the N- $C_\alpha$  resulting respectively in  $a_n/x_n$ ,  $b_n/y_n$  or  $c_n/z_n$  ions, whereas  $a_n$ ,  $b_n$ ,  $c_n$  represent fragments where the charge is kept at the N-terminal side of the peptide and  $x_n$ ,  $y_n$ ,  $z_n$  represent fragments where the charges is kept at the C-terminal side of the peptide. Fragment ions regarding amino acid side chains are referred to as  $v_n$ ,  $w_n$ , and  $d_n$ .

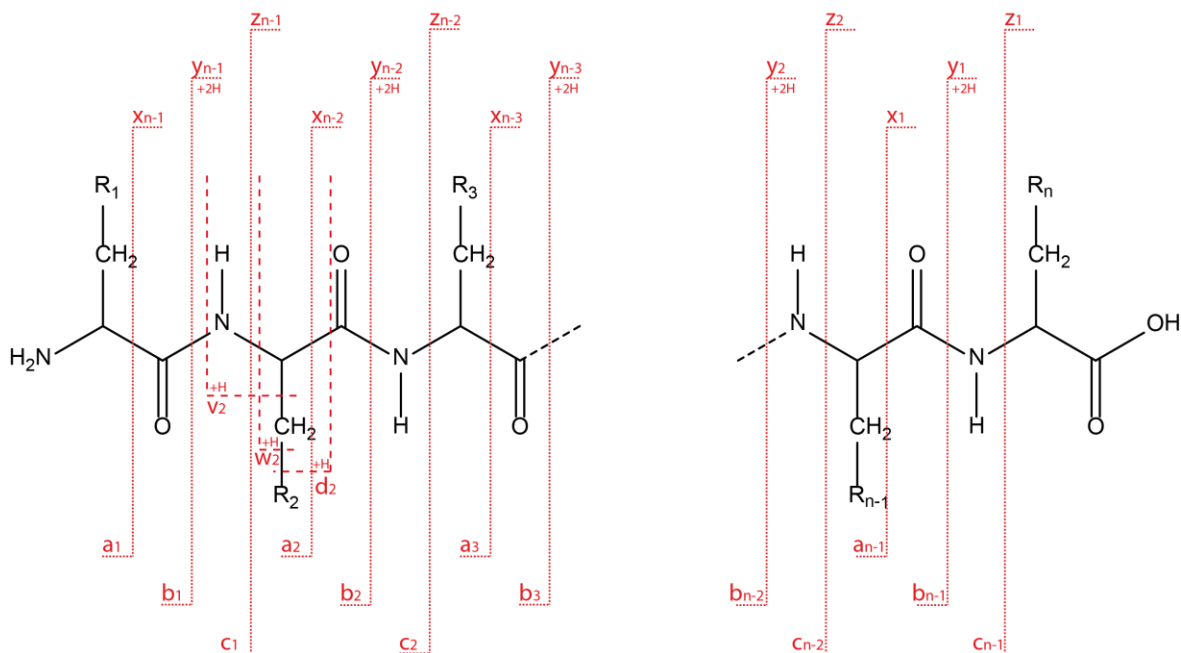


Figure 16: Nomenclature of peptide fragmentation by Roepstorff and Fohlman (1984)

The mass differences between the ions of a specific fragmentation type allow identifying consecutive amino acids and therefore identification of the amino acid sequence of the precursor ions. PSD fragmentation due to the soft ionization technique of MALDI mainly results in b-type and their corresponding y-type ions, a- and x-type ions are also possible, whereas c- and z-type ions usually can only be observed at high-energy CID fragmentation. In a certain fraction, fragmentation also results in the formation of immonium ions, which are single amino acid side chains formed by a combination of C<sub>α</sub>-C and C-N cleavage and can be used as indicator for the peptides AS composition.

Similar to PMF, a database comparison using web-based platforms can be performed for analyte identification. Here again specific parameters are defined and experimentally retrieved consecutive mass differences are compared to theoretical amino acid sequences stored within the database. In contrast to PMF, this method allows to identify homolog proteins, since only partial amino acid sequences of the intact protein are compared (Papayannopoulos 1995; Clauser et al. 1999). In addition, this method also allows manual assignment of consecutive amino acids for proteins still unknown to the database. Unfortunately manual assignment is very time consuming and computer based algorithms are not well established so far.

## 1.6 Lipid Identification using MALDI-MS

Fragmentation by CID can also be used to identify and characterize lipids, whereas high-energy CID even allows determining the location of double bonds at the fatty acid side chains. Unfortunately fragmentation of lipids is not as straight forwards as for proteins. Fragmentation behavior is strongly depending on the lipid class and on the type of precursor ion. Protonated precursor ions usually only yield molecular masses of the fatty acid substituents, as well as loss of the polar head group, allowing to identify the classes of lipids. While mono- or even double- or triple-sodiated precursor ions can yield further fragmentation of the fatty-acid substituents, which in some cases allows determining the position of double bonds or hydroxyl groups. Detailed study of the fragmentation behavior of triacylglycerols was first done by Cheng et al. (1998) who also proposed a fragment nomenclature. Further studies for different lipid classes were also published by Pittenauer and Allmaier (2009) and (2011).

## 1.7 Ion Mobility Mass Spectrometry

Ion mobility coupled to mass spectrometry (IM-MS) is becoming a technique of increased interest, since it represents a powerful tool to investigate structure and conformation of biomolecules in correlation to their MW. This allows not only distinguishing different classes of isobaric biomolecules like peptides or lipids, but also structural isomers and chiral compounds, which play a major role for biological activity.

The technique of ion mobility spectrometry (IMS) is a rather old one. It was introduced in the 1960s by E. W. McDaniel and was basically described as a gas-phase ion separation technique (McDaniel et al. 1962). Hereby ions were separated by their charge, size and shape characteristics, which are summed up as collision cross section. At the original setup, the ions were pushed into a gas-filled drift tube (usually an inert gas such as helium or nitrogen) where a weak constant axial field was applied. Hereby small ions can pass this drift tube faster than large ions due to lower collision frequency and are therefore detected separately in respect to their velocity or rather drift time which is directly proportional to the electric field  $E$  (Kanu et al. 2008; Santos et al. 2010). The proportionality factor  $K$  is defined as the ion mobility and is related to the ion's collision cross section  $\Omega$  (equ. [1.8]). The ion's charge is defined as  $q$ , the density of the buffer gas as  $N$ ,  $k$  is the Boltzmann's constant,  $T$  the absolute temperature,  $m$  the mass of the buffer gas and  $M$  is the mass of the ion of interest.

$$K = \left(\frac{3q}{16N}\right) * \left(\frac{2\pi}{kT}\right)^{\frac{1}{2}} * \left(\frac{m+M}{mM}\right)^{\frac{1}{2}} * \left(\frac{1}{\Omega}\right) \quad [1.8]$$

Those early drift time IMS (DT-IMS) systems showed poor sensitivity due to a low duty cycle, which lead to the development of various ion mobility separation methods like differential mobility analysis (DMA), field asymmetric waveform IMS (FAIMS) or traveling wave IMS (TW IMS). It has to be noted, that drift time IMS is the only method allowing direct measurement of the collision cross-section (CCS). All other methods have to be calibrated in a mathematical and/or numerical way (Kanu et al. 2008; Shvartsburg and Smith 2008).

Determination of ion mobility used to be restricted to mass selected ions by a fixed mass spectrometer or in the reversed way, mass spectra were recorded for defined ion mobilities. The coupling and development of a TOF mass spectrometer having a high acquisition rate enabled the simultaneous recoding of mass-resolved mobilities for all present ions. This is possible since flight times are much shorter than drift times. In other words, the frequency in which ion packets are pushed into the drift tube is much lower than the frequency in which

exiting ions can be pushed into the flight tube of the TOF mass analyzer. Each observed mass spectrum therefore represents all  $m/z$  species within a specific drift time window of the ion mobility spectrum (Hoaglund et al. 1998).

TW-IMS is a commercial available method integrated into an orthogonal acceleration TOF (oaTOF) mass spectrometer (see chapter 1.7.1). The travelling wave mobility cell shows a design similar to traditional DT cells. It is constructed as a series of stacked ring ion guides, but instead of a low electric field stretching over the whole drift cell, a high electric field is applied to a pair of adjacent ring electrodes (see Figure 17). To propel the ions through the cell, the field is thereby subsequently moved to the next pair of electrodes in the direction of ion migration, thus generating waves of the electric field which carries the ions and sweep them through the cell as illustrated in Figure 18 (Giles et al. 2004; Shvartsburg and Smith 2008). Applying inert gas, like nitrogen, in the mobility cell results in separation of the ions according to their mobility by being unable to keep up with the wave front. Ions thereby slip periodically behind the wave, whereas species with low mobility slip behind more often than species with high mobility resulting in longer drift times (Pringle et al. 2007).

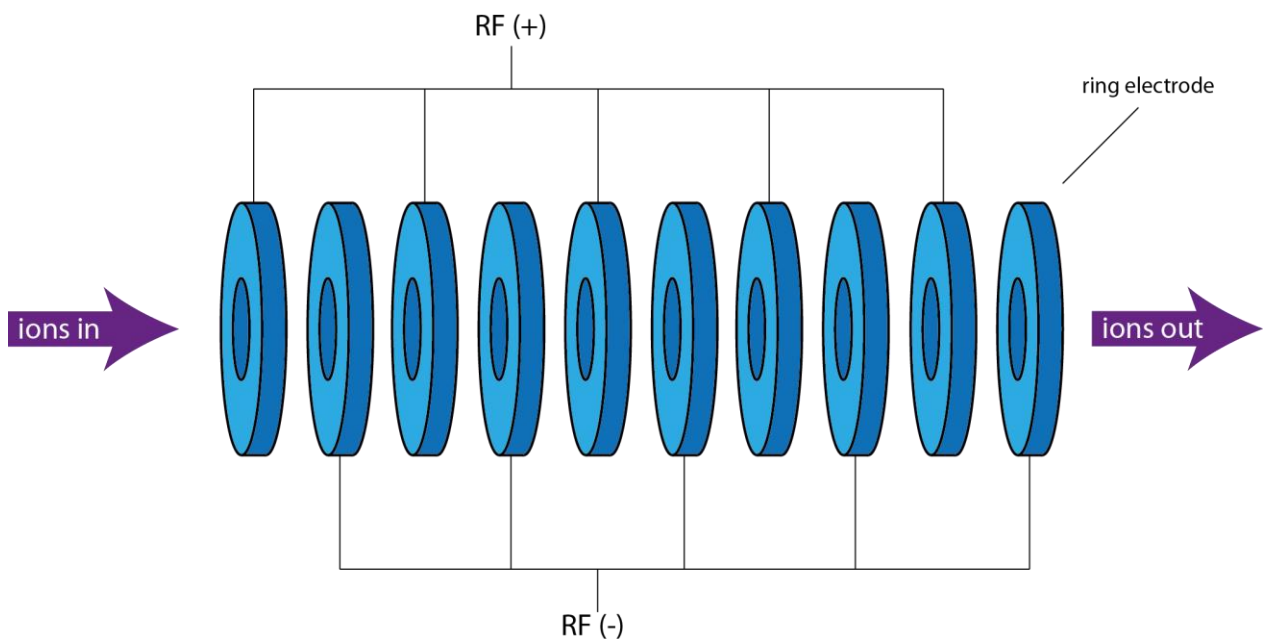


Figure 17: Stacked ring ion guide

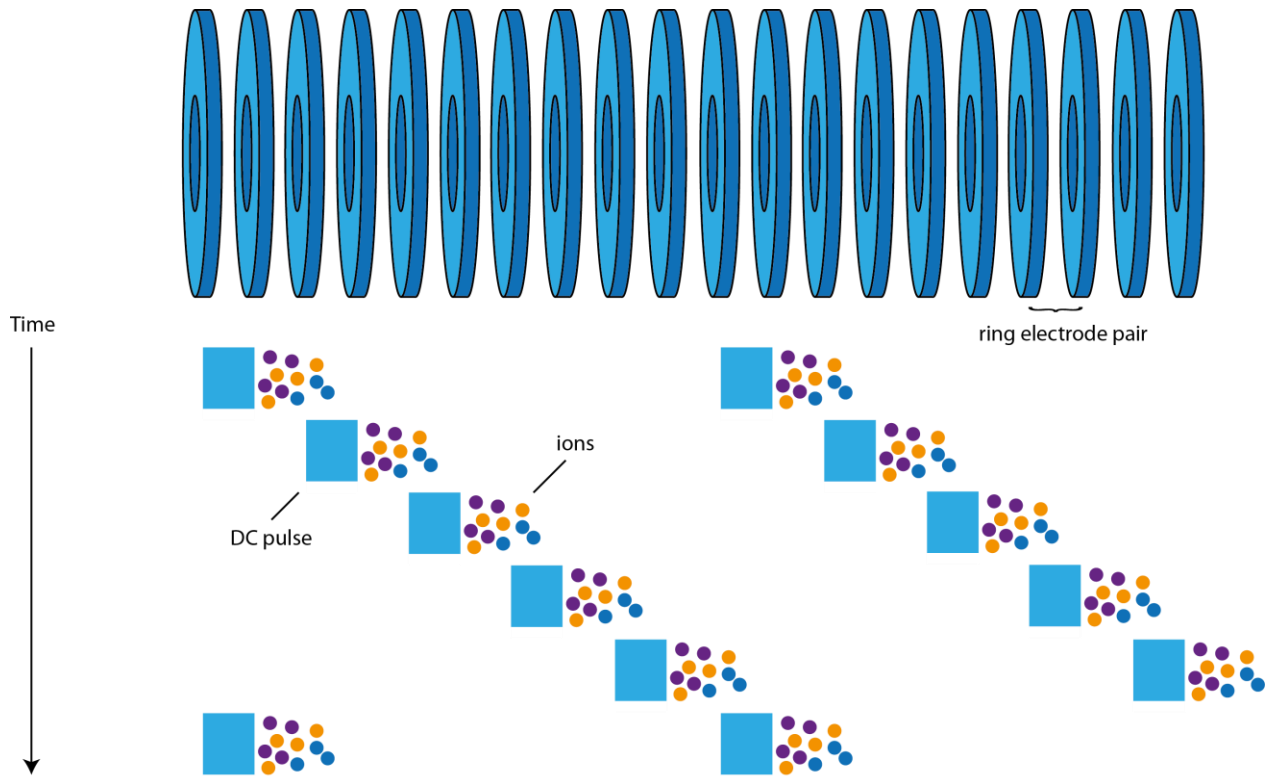


Figure 18: Illustration of a travelling wave carrying ions

The implementation of new methods for separation by ion mobility, resulting in better ion transmission, monitoring ion mobility in a continuous manner or high IMS resolving power, as well as the commercial implementation of coupling IMS with TOF-MS makes IMS an interesting and powerful tool for new applications. For example it can be used for medical research to analyze protein missfolds which are a common feature of diseases, or to identify stereoisomers of pharmaceutical products. Since IMS is a slower separation method than TOF-MS, the implementation of CID after mobility separation allows fast fragmentation of all ions and allocation of their corresponding product ions, representing an upcoming alternative to LC-ESI-MS. It also can be used to differentiate biomolecules in a first overview according to their category and if combined with MS imaging as a second dimension used for separation, easily illustrates the lateral distribution of various biomolecule species.

### 1.7.1 The MALDI Synapt G2 HDMS

The Synapt G2 HDMS is a commercially available MS instrument developed by Waters (Manchester, UK), which can operate in both, IMS- and MS-mode. This mass spectrometer consists of four main components: the ion source, a quadrupole, a Triwave device and an orthogonal acceleration RTOF mass analyzer (see Figure 19). The Triwave device can also be used for fragmentation analysis.

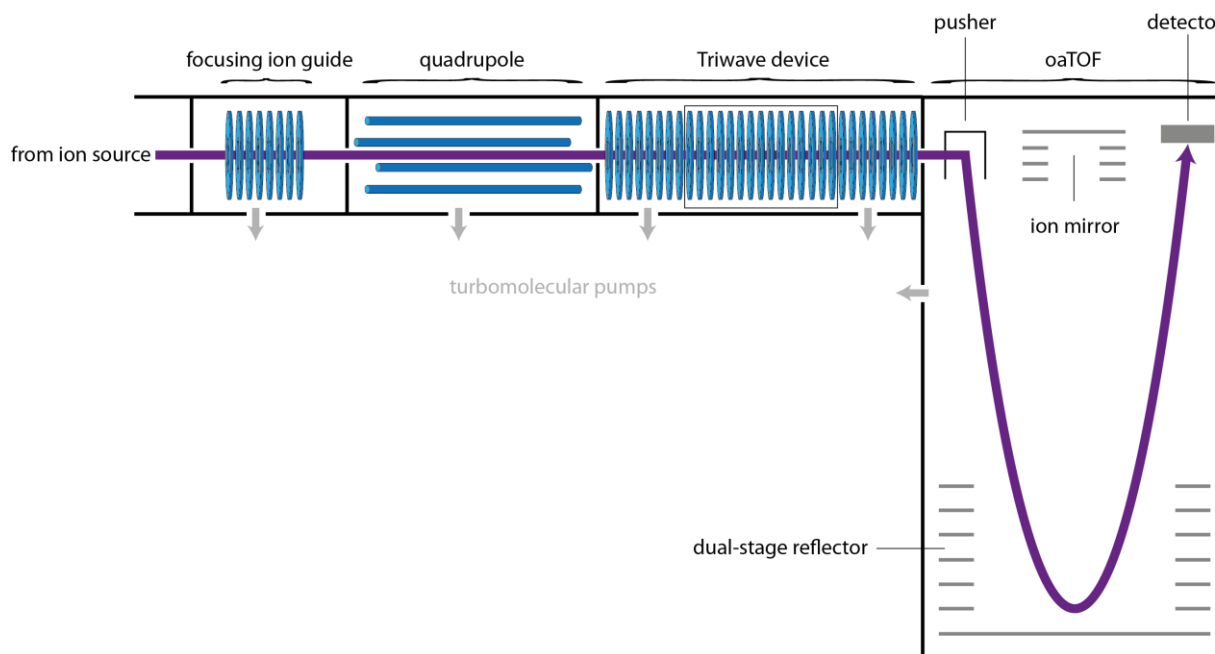


Figure 19: Schematic diagram of the Synapt G2 HDMS

#### Ion Source:

This Instrument can either use an ESI ion source, or a MALDI ion source. In this thesis the implemented MALDI source was used, which works with a Nd:YAG high repetition laser, with a wavelength of 355 nm and a variable pulse energy up to 100  $\mu\text{J}$  at 1 kHz. The laser spot size can be switched between 250  $\mu\text{m}$  and 75  $\mu\text{m}$  (Waters 2010; Waters 2011).

#### Quadrupole:

Formed in the ion source, the ion beam is focused by an ion guide and enters the quadrupole. During normal TOF-MS acquisition this quadrupole operates in an RF-only mode, passing the ions to the TOF mass analyzer. The RF voltage is thereby applied 180 degree out of phase to each pair of opposite rods. To guarantee good ion transmission over the desired  $m/z$  range, a RF profile over the scan time is generated (Waters 2007).

For tandem MS experiments, this quadrupole operates in RF and DC mode, acting as the first mass analyzer to select ions of interest. According to the applied DC voltage, only ions with the desired  $m/z$  ratio will pass the quadrupole, while all other ions spiral out and are lost (Waters 2007; Waters 2009).

### **Triwave device:**

The Triwave device consists of three consecutive travelling wave ion guides (TWIGs) as illustrated in Figure 20, whereby each is performing a distinct function.

The first TWIG is referred to as Trap, which traps, accumulates and releases the ions periodically into the subsequent TWIG if the instrument is operated in mobility mode. The Trap is typically operated at low argon pressure of approx.  $10^{-2}$  mbar (Waters 2009). A constant RF-voltage, but no travelling wave is applied and on the final electrode of the Trap a modulated DC-only voltage is applied, acting as ion gate. For TOF-MS operation the Trap acts as an efficient Transfer ion guide without trapping (Pringle et al. 2007).

The second ion guide is called the IMS TWIG and can operate in two modes. For standard TOF-MS operation the IMS TWIG acts as a transfer device with highly effective ion transmission to the TOF mass analyzer. Operating in mobility mode, a travelling wave is applied and, compared to the TOF mode, the gas pressure is elevated using nitrogen resulting in mobility based separation. The IMS TWIG consists of almost the same number of electrodes as the Trap and the subsequent Transfer-TWIG together and represents, except for the ion entrance and exit, a gas tight cell allowing operation pressures of up to 1 mbar. At the front of the IMS TWIG, a helium cell is implemented to transfer the ions from the low pressure of the Trap to the region of elevated IMS pressure with a minimum of fragmentation (Waters 2007; Waters 2008; Waters 2009). Hereby helium is mandatory, to result in maximum efficiency.

The Transfer TWIG is the final ion guide. It efficiently transfers the ions to the orthogonal acceleration TOF using a continually travelling wave to maintain the mobility separation. Its composition is similar to the Trap TWIG and the same argon pressure is applied.

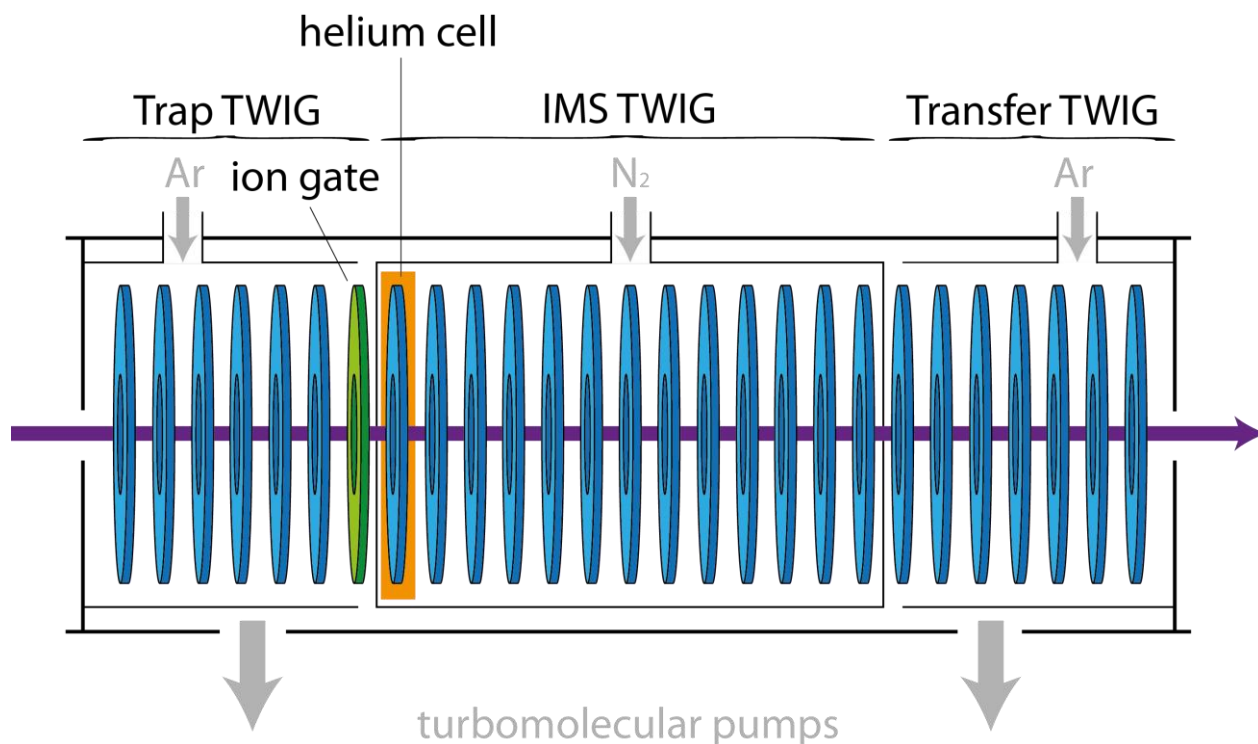


Figure 20: Schematic diagram of the Triwave device

Operating in mobility mode, the drift times of detected ions are determined by subtracting the time of their gated release into the IMS TWIG from the time of their push into the field free drift region of the TOF mass analyzer.

#### Orthogonal Acceleration RTOF:

The ion flight path of this mass analyzer is set in a 90 degree angle to the previous flight path through the quadrupole and Triwave device, thus a pusher is necessary to change the flight direction of the ions. This setup has the major advantage to separate and detect fragmentation product ions without the use of further acceleration lens optics or a curved field reflector as described in chapter 1.4.3, while still maintaining rather high collision energy (de Hoffmann and Stroobant 2007). Two ions with the same  $m/z$  ratio might still not receive the same “push” resulting in different velocities. This will be corrected by the use of a RTOF.

In this instrument a two-reflectron geometry is implemented and the mass analyzer can operate in two ways. For standard resolution and high sensitivity the instrument operates in “V” mode, one dual-stage reflector deflects the ions coming from the pusher to the detector (see Figure 21/a). To achieve higher resolution and exact mass calibration a second ion mirror is used in addition to the dual-stage reflector (operation in “W” mode), thus generating a

longer flight path for better ion separation (see Figure 21/b). Unfortunately the double reflecting mode is less sensitive than the single-reflecting mode, due to higher ion transmission loss

(Waters 2009). The frequency, with which the pusher sends ions into the field free flight region, depends on the selected  $m/z$  range. For a large  $m/z$  range it takes more time for all ions to reach the MCP detector, therefore varying amounts of mass spectra can be accumulated for one ion laser pulse or one ion mobility package (Waters 2007).

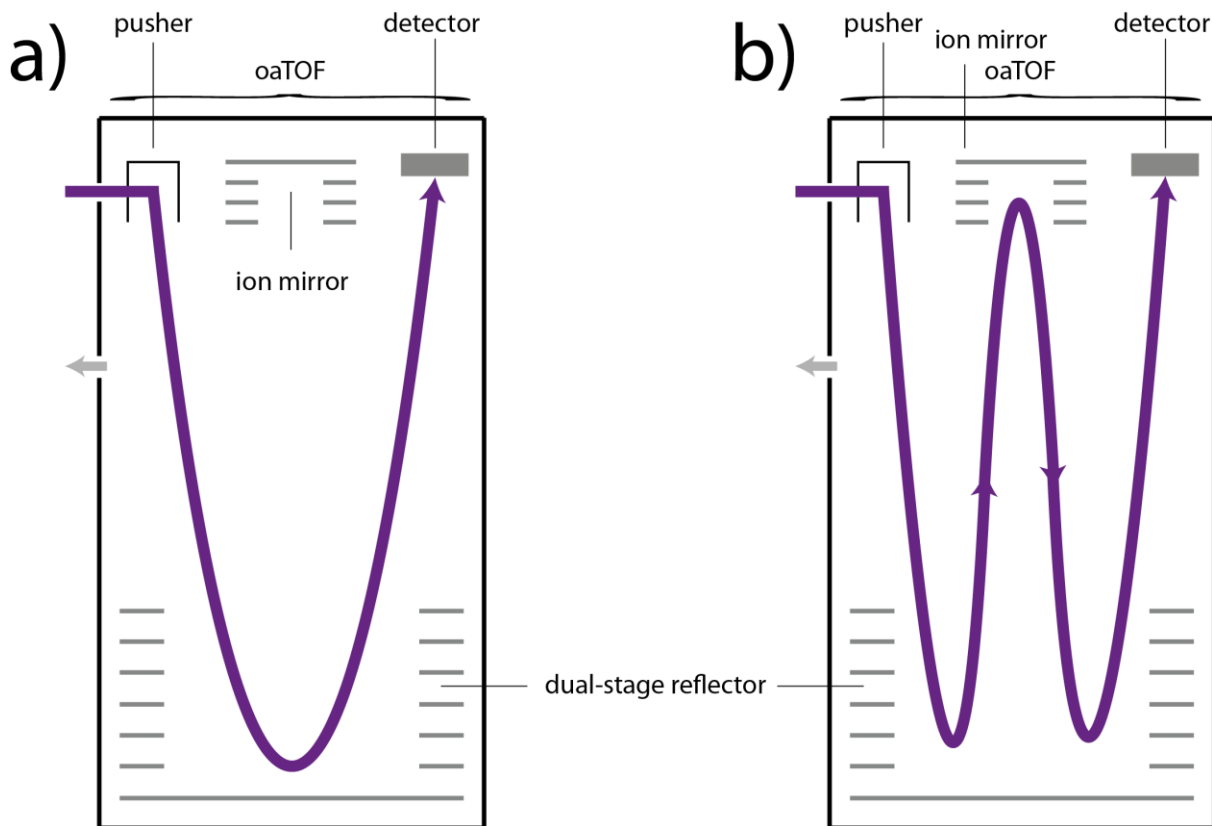


Figure 21: Operation modes of the oaTOF; a) V mode, b) W mode

### 1.7.1.1 "Perfect Wave"

To generate mass resolved ion mobility data, ions are periodically gated into the mobility cell and each period of a gated release is divided into 200 subsequent orthogonal acceleration pushes of the mass analyzer. One mobility separated ion package is therefore resolved into 200 mass spectra which are referred to as bins. This process is repeated for a defined time and the generated mass spectra for each bin are accumulated generating a three dimensional dataset of  $m/z$  value, drift time and intensity (Waters 2009).

To optimize the ion mobility separation certain parameters in the mobility cell have to be adapted. The “perfect wave” for best results separates one ion packet within the time-window of 200 bins. Best practice leaves the first and the last 20 bins empty (not containing separated ions) in order to prevent ion carry over from one ion package to the next. For optimization, mainly the gas pressure within the IMS cell as well as its inherent wave velocity and the wave height are used. By increasing the gas pressure or decreasing the wave height, the ions need longer time to pass the IMS cell. In contrast by decreasing gas pressure and increasing wave height, much shorter drift times are accomplished, but results in bad separation. The wave velocity of the IMS cell also influences the separation quality, but has a more equal impact on all ion species, thus shifts all ions to higher or lower drift times (Waters 2007; Waters 2009).

It is also possible to vary the wave height and velocity of the IMS cell over the 200 bin window by setting a linear or proportional ramp. This can help to improve mobility separation since the effective length of the IMS cell increases.

#### 1.7.1.2 Fragmentation

Due to the particular setup of this instrument, various fragmentation experiments can be performed. Both, the Trap and the Transfer TWIG, are basically constructed like collision cells and operate at the necessary collision cell pressure, therefore high-energy (collisions at energy levels up to 240 V are possible) ion fragmentation can be performed in either one, or both of these regions.

Standard MS/MS experiments are performed by selection of a precursor ion in the quadrupole and using just the Trap TWIG as CID fragmentation cell. Hereby the product ions can be separated according to their mobility as well (see Figure 22/a).

Since IMS is able to separate isobaric analyte ions, fragmentation in the Transfer TWIG gives a major advantage. Isobaric ions selected by the quadrupole, or ions with rather close  $m/z$  ratios, are further separated according to their drift time by the IMS TWIG and subsequently fragmented in the Transfer TWIG (Waters 2009). The generated product ions keep the same drift time as their precursor ions, thus fragments and precursor can be allocated in the same spectrum (see Figure 22/b).

Both described fragmentation applications can be combined, representing a Pseudo-MS<sup>3</sup> experiment. Hereby CID fragmentation occurs in both, the Trap and the Transfer TWIG. A precursor ion is selected by the quadrupole and product ions are generated in the Trap TWIG.

The product ions are then separated according to their mobility and further fragmented in the Transfer TWIG. This MS<sup>3</sup>-type experiment has the advantage, that all first and second generation product ions are recorded at the same time (Waters 2009). Second generation product ions are allocated to their first generation product ions by identical drift time (see Figure 22/c).

The last possible operation mode is called High Definition Mass Spectrometry Experiment (HDMS<sup>E</sup>) by Waters. Hereby high energy CID fragmentation occurs in the Transfer TWIG after mobility separation, but “no” precursor ion is selected, thus all analyte ions are fragmented. In order to increase the intensity of all precursor ions, fragmentation is only applied to every second ion package entering the Triwave device (Claude et al. 2012). This mode shows a lower sensitivity, respectively only half the ions produce a signal which can be accumulated. But it also shows a major advantage in time and sample consumption, since MS and MS/MS information from all detectable ions are acquired within a single experiment. Precursor and product ions are again allocated by identical drift time (see Figure 22/d).

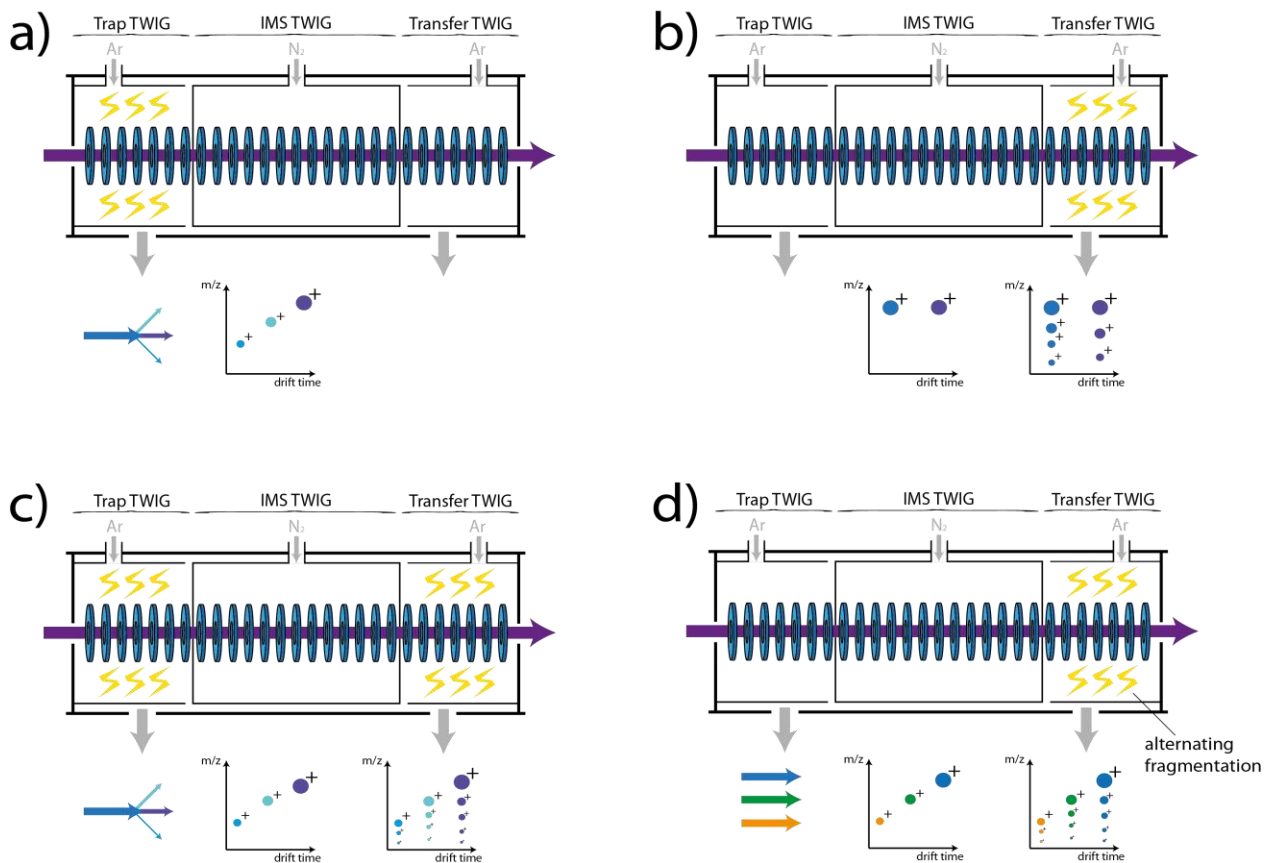


Figure 22: Possible fragmentation modes in a SYNAPT G2 HDMS instrument: a) Trap fragmentation, b) Transfer fragmentation, c) MS<sup>3</sup>-type, d) HDMS<sup>E</sup>

## 1.8 MALDI Mass Spectrometry Imaging

MS imaging is a powerful tool to directly obtain mass related information from atomic to macromolecular ions on surfaces and to subsequently generate visual information on lateral distribution without the requirement of labeling. It combines the determination of intensity and localization of  $m/z$  values on the sample surface. The generated images can be aligned to light microscopic images to correlate chemical information with physical features (McDonnell and Heeren 2007; Stauber et al. 2010). Secondary ion mass spectrometry (SIMS), desorption electrospray ionization MS (DESI-MS) and MALDI-MS are the most common used techniques, while MALDI is primarily used for biological application since it has been proven to be an effective and a rather sensitive method to desorb and ionize lipids, peptide, proteins, polymers and a wide range of other organic molecules (Karas et al. 1989). Also matrix can easily be distributed on biological surfaces using methods like airbrush spraying or chemical inkjet printing, latter with high positioning accuracy to facilitate the ionization process.

MALDI-MS imaging represents new opportunities like the differentiation of tumor tissue from adjacent non-tumor tissue (Schwartz et al. 2005) or mapping drugs or other metabolites in specific tissues like brain, kidney or even whole body sections (Stoeckli et al. 2007). Nevertheless there are several limitations regarding MALDI-MS imaging. One limitation is the huge amount of data which is collected, since every pixel of the image represents an ion mass spectrum (i.e. a voxel). Another limitation is the large number of different potential analytes present in biological tissue, which makes peak assignment and evaluation difficult. This is also hindered by ionized material which is not correlated to the analyte of interest and is therefore responsible for a high background signal. Complex samples like tissues also include various classes of biomolecules like lipids or proteins, making the presence of isobaric masses likely. For certain identification of questionable Signal, MS/MS experiments can usually be performed. Unfortunately this can only be done for a limited number of analytes, since the available amount of sample is quite limited. This effect increases with higher lateral resolution, since the sample amount at each position decreases (McLean et al. 2007; Kiss and Heeren 2011).

These limitations can be overcome partly by the two dimensional separation method of MALDI-IM-MS imaging. This approach adds the dimension of molecular structure to the imaging experiment and even allows simultaneous MS and MS/MS analysis as described in the previous chapter. Combination of MS imaging with ion mobility also represents a possibility for

proteomic bottom-up approaches (see chapter 1.5) by proteolytic digestion of surface proteins and subsequent characterization by fragmentation (Stauber et al. 2010).

## 2 Materials and Methods

### 2.1 Chemicals

Castor bean oil; obtained from local pharmacy

#### **AppliChem (Darmstadt, Germany)**

SDS (sodium dodecylsulfate); molecular biology grade

Prod# A2263, 1000                      LOT# 2k001571

#### **Fluka Biochemik (Buchs, Switzerland)**

ACN (Acetonitrile); LC-MS CHROMASOLV®

Prod# 34967-2,5l                      LOT# SZBC219 AV

Ammonium hydrogen carbonate; Ultra  $\geq 99.0\%$

Prod# 09830                              LOT# 446338

DHB (3,5-Dihydroxybenzoic acid);  $\geq 97\%$

Prod# 37600

#### **GE Healthcare (Little Chalfont, UK)**

IPG buffer ampholyte pH 3-10 NL

Prod# 17-6000-88                      LOT# 10067121

IPG strip (Immobiline™ DryStrip pH 3-10 NL, 7 cm)

Prod# 17-6001-12                      LOT# 10046162

#### **Life technologies, former Invitrogen (Carlsbad, CA, USA)**

BenchMark™ Protein Ladder

Prod# 10747-012                      LOT# 470011

Molecular Weight Standard Mixture, Recombinant

Prod# M-0671                              LOT# 043k1474

Novex™ Sharp Pre-Stained Protein Standard

Prod# LC5800                              LOT# 921621A

NuPAGE® 4-12% Bis-Tris 1.0mm X15 well

Prod# NP0323BOX

NuPAGE® 4-12% Bis-Tris 1.0 mm 2D-well  
Prod# NP0326BOX                      Lot# 10032972

NuPAGE® LDS Sample Buffer (4x)  
Prod# NP0007                              LOT# 934122

NuPAGE® MOPS SDS Running Buffer (20x)  
Prod# NP0001                              LOT# 1257781

NuPAGE® Reducing Agent (10x)  
Prod# NP0004                              LOT# 1085151

**Merck KGaA (Darmstadt, Germany)**

Acetone; for analysis  
Prod# 1.00014.2500                      LOT# k44241114

EtOH (Ethanol); absolute for analysis  
Prod# 1.00983.2500                      LOT# k43900883 242

Formic acid; 98-100 % pro analysi  
Prod# 1.00264.1000                      LOT# k32314764 332

Glycerol; for Analysis  
Prod# 1.04092.1000                      LOT# k42075192 110

MeOH (Methanol); LiChrosolv®, gradiend grade for LC  
Prod# 1.06007.2500                      LOT# I649107 230

Paraffin; highly liquid  
Prod# 1.07174.2500                      LOT# k42966074 204

Silver nitrate; p.A.  
Prod# 1.01512.0025                      LOT# k42613112 131

Tris(hydroxymethyl)aminomethane  
Prod# 1.08387.2500                      LOT# k42846187 209

Urea; p.A.  
Prod# 1.08487.1000                      LOT# k35769587 620

**Milipore (Bedford, MA, USA)**

UHQ (ultra high quality water), conductivity parameter 18.2 mΩ\*cm ( at 25 °C)

ZipTip C18

Prod# ZTV18S960                      LOT# RZHA12629

**Riedel-de Haën Ag (Seelze, Germany)**

Sodium thiosulfate-5-hydrate; p.A.

Prod# 31459                              LOT# 11280

**Roche (Penzberg, Germany)**

Trypsin rec.; proteomics grade

Prod# 03 708 985 001              LOT# 13798721

**Sigma-Aldrich (St. Louis, MO, USA)**

α-CHCA (α-cyano-4-hydroxycinnamic acid); ≥98 %

Prod# C2020-10G                      LOT# MKBF4800V

Acetic acid; ≥99,8 %

Prod# 33209-2.5L                      LOT# SZBB3220V

Aniline; ACS reagent ≥ 99.5%

Prod# 242284-5ML                      LOT# 5TBD5561V

Bromophenol blue, sodium salt; Electrophoresis Reagent

Prod# B-8026 5G                        LOT# 29H3653

Cardiolipin; sodium salt in MeOH (4.8 mg/ml)

Prod# C-5646                              LOT# 11H8359

CHAPS (3-[(3cholamiopropyl)dimethylammonio]-1-prpanesulfonate; ≥98 % (TLC)

Prod# C9426-5G                        LOT# 041M53035V

DTT (DL-dithiothreitol); Bio Ultra ≥99.0 %

Prod# 43817-5G                        LOT# BCBD 9063V

Formaldehyde; 36.5-38 % for molecular biology, in H<sub>2</sub>O containing 10-15% MeOH as stabilizer

Prod# F8775-25ML                      LOT# SZBC0620V

IAA (iodoacetamide); Bio Ultra  
Prod# I1149-25G                      LOT# 040M53241V

L- $\alpha$ -Phosphatidylcholine; C22:0  
Prod# S7004-5MG                      LOT# 27H8398

Potassium hexacyanoferrate (III)  
Prod# P8131-100G                      LOT# MKBH1447V

Sodium carbonate  
Prod# 71350-1KG                      LOT# BCBD3064V

TFA (trifluoroacetic acid); 99 % for protein sequencing  
Prod# 537-25G                      LOT# BCBF6765V

Thiourea; minimum 99.0 %  
Prod# 7875-500G                      LOT# 033k0123

### Thermo Scientific (Rockford, IL, USA)

Albumin Standard, 2.0 mg/ml bovine serum albumin in 0.9% saline and 0.05% sodium azide  
Pod# 23209                      LOT# LB142239

Coomassie Plus – The Better Bradford Assay™ Reagent  
Prod# 23238                      LOT# JK127950

Pierce® BCA Protein Assay Kit – Reducing agent compatible  
Prod# 23250                      LOT# LC141858

Content:

**BCA Reagent A**, 250 ml containing sodium carbonate, sodium bicarbonate, bicinchoninic acid and sodium tartarate in 0.1 M sodium hydroxide

**BCA Reagent B**, 25 ml containing 4% cupric sulfate

**Compatibility reagent**, 10 x 20 mg tubes

**Reconstitution buffer**, 15 ml

**Albumin standard**, containing bovine serum albumin at 2.0 mg/ml in 0.9 % saline and 0.05 % sodium azide

### VWR (Fontenay-sous-Bois, France)

Chloroform; 99.2 % SPECTRONORM, stabilized with 0.6% Ethanol

Prod# 22715.293

LOT# 11C070500

### Waters (Manchester, UK)

Q-ToF Product Sample Kit; PEG (polyethyleneglycol) Maldi Ready Mixed Solution (10 mg/ml)

Prod# 700003276-11

LOT# W16041212

## 2.2 Equipment / Instruments

- 500 µl and 1.5 ml Eppendorf® sample vials
- AirbrushAC-55 by Conrad Electronic (Wels, Austria)
- Chemical Inkjet Printer CHIP-1000 by Shimadzu Biotech Kratos Analytical (Manchester, UK)
- Electrophoresis Power Supply EPS 3501 XL by Amersham Bioscience (Uppsala, Sweden)
- ITO glass slides (indium tin oxide coated glass slides) (Bremen, Germany)
- Lab-Centrifuge SIGMA 1-14 by SIGMA (Osterode am Harz, Germany)
- MSP Big Anchor 96 BC microScout Target by Bruker Daltonik (Bremen, Germany)
- Multiphor II by Amersham Bioscience (Uppsala, Sweden)
- Nano Photometer by Implen (Munich, Germany)
- PowerEase™ 500 by Novex (CA, USA)
- Thermomixer comfort by Eppendorf AG (Hamburg, Germany)
- Ultrasonic cleaner by VWR (Leuven, Belgium)
- Vacuum centrifuge UNIVAPO 100H with UNICRYO MC2L-60°C by UNI EQUIP (Planegg, Germany)
- XcellSurelock® Mini Cell by Invitrogen (CA, USA)

**UltrafleXtreme** by Bruker Daltonics (Bremen, Germany):

A MALDI-TOF/RTOF instrument operating with a 2 kHz Smartbeam laser (modified Nd:YAG laser, 355 nm) which can be focused to a diameter down to 10 µm. For fragmentation processes, the instrument is setup according to the LIFT method (see chapter 1.4.3). Instrument operation was carried out using flexControl Version 3.4 (Build 119) by Bruker Daltonics.

**Synapt G2 HDMS** by Waters (Manchester, UK):

A qTOF instrument used with the complimentary MALDI source operating with a 1 kHz solid state Nd:YAG laser (355 nm) with variable pulse energy up to 100 µJ. The ablation spot of the laser on the target is of elliptic shape with the largest diameter of approx. 180 µm and the smallest diameter of approx. 150 µm. In chapter 1.7.1, the instrument is described in more detail.

## 2.3 Sample Collection

Samples of the secreted salamander adhesive were provided by J. von Byern<sup>2)</sup>, the collection contained the following samples:

Secretion on Aclar® film was provided for two specimens of *P. shermani*. The Aclar film was cleaned with EtOH and placed in a petri dish with one animal on top, the petri dish was then closed and slightly shaken to provoke the salamander and induce bioglue secretion. Within seconds of exposure to air, the milky secretion thereby bonded strongly to the film. These samples will further be referred to as “Aclar-1” and “Aclar-2”.

A mixture of vacuum dried, powder-like bioglue from different specimens of *P. shermani* was provided as well. Hereby secretion was induced by gently twitching the animal with tweezers and the excreted glue was harvested in a sample vial. This sample will further be referred to as “glue-mixture”.

For dissolving the samples, different protocols were tested (see chapter 3.1)

---

<sup>2)</sup> Ludwig Boltzmann Institute for Experimental and Clinical Traumatology, Vienna, Austria

## 2.4 Protein Concentration – Bicinchonin Acid Assay (BCA)

### Working Solutions:

- Working compatibility reagent:
  - 500 µl UHQ + 500µl Reconstitution Buffer in 1 Compatibility Reagent tube
  - Vortex well and store up to 8 hours at 4°C protected from light
- BCA Working Reagent:
  - 50 parts BCA Reagent A + 1 part BCA Reagent B

### Protocol:

The Albumin Standard stock-solution was diluted to concentrations of 1.5 mg/ml, 1.0 mg/ml, 750 µg/ml, 500 µg/ml, 250 µg/ml and 125 µg/ml using the same buffer as for the corresponding sample dilution. A blank, containing just the sample buffer was prepared in parallel. Samples were diluted in various ratios using sample buffer, to fit the calibration function.

25 µl of sample standard or blank were mixed in a 500 µl sample vial with 25 µl Working compatibility reagent and incubated for 15 min at 37 °C. Further 100 µl of BCA Working Reagent were added, mixed and incubated for 30 min at 37 °C. After cooling to room temperature for 5 min, photometric absorption was measured at 562 nm with a disposable microliter cuvette. A calibration curve was constructed using albumin standards, to calculate protein concentration of the sample. All samples, standards and blanks were prepared and measured in duplicates.

## 2.5 Protein Concentration – Bradford Assay

### Protocol:

The Albumin Standard stock-solution was diluted to concentrations of 1.5 mg/ml, 1.0 mg/ml, 750 µg/ml, 500 µg/ml, 250 µg/ml and 125 µg/ml using the same buffer as for the corresponding sample dilution. A blank, containing just the sample buffer was prepared in parallel. Samples were diluted in various ratios using sample buffer, to fit the calibration function.

5 µl of Sample Standard or Blank were mixed in a 500 µl sample vial with 25 µl Coomassie Plus – The Better Bradford Assay™ Reagent and incubated for 10 min at room temperature.

Photometric absorption was measured at 595 nm with a disposable microliter cuvette and a calibration curve was constructed using albumin standards, to calculate protein concentration of the sample. All samples, standards and blanks were prepared and measured in triplicates.

## 2.6 1D-PAGE

### Working Solutions:

- Running Buffer:  
40 ml Novex™ MOPS SDS Running Buffer (20x) + 760 ml UHQ

### Protocol:

The secure strip of the NuPAGE 4-12% Bis-Tris 1D gel was removed and the gel was washed with UHQ prior to inserting in the XcellSureLock Mini Cell chamber. Running Buffer was filled in both, the cathode and anode chamber.

6.5 µl of Sample or Blank were mixed with 2.5 µl of NuPage LDS Sample Buffer (4x) and 1 µl NuPAGE Reducing Agent (10x) in a 500 µl sample vial. All samples were heated at 70 °C for 10 min followed by briefly spinning down, to gather all liquid at the bottom of the vial. 10 µl of each sample were then carefully pipetted in the wells of the gel.

Electrophoresis was carried out for approximately 50 min at a constant voltage of 200 V and an expected current of 100-125 mA/gel at the start and 60-80mA/gel at the end of the electrophoresis.

## 2.7 2D-PAGE

### Working Solutions:

- TRIS-HCl:  
50 mM tris(hydroxymethyl)aminomethane adjusted to pH 8.5 with HCl
- Rehydration buffer:  
7 M urea, 2M thiourea, 2% CHAPS, 0.002% bromophenol blue
- Equilibration solution:  
6 M urea, 75 mM Tris-HCl (adjusted to pH 8.8 with HCl), 29.3% Glycerol, 2% SDS, 0.002% bromophenol blue
- Equilibration I – reduction:  
70 mg of DTT were added to 7 ml of Equilibration Solution

- Equilibration II – alkylation:
  - 175 mg of IAA were added to 7 ml of Equilibration Solution
- Running buffer:
  - 40 ml Novex™ MOPS SDS Running Buffer (20x) + 760 ml UHQ

### **Protocol:**

10 µl of sample solution were mixed with 2.5 µl IPG buffer ampholyte and 115 µl of rehydration buffer. The solution was then distributed over approximately 4 cm in one chamber of the Reswelling Tray, followed by placing the IPG strip on the sample with the gel side facing down without trapping any air bubbles. To guarantee effective rehydration, paraffin was deposited at the ends of the strip to keep the sample solution at the gel, as well as on top of the strip to prevent the system from drying out. The IPG strip was equilibrated for 24 h.

After 24 h of rehydration, the IPG strip was placed on the Multiphor II device with the gel side facing up and both ends were slightly covered with a wetted filter strip (UHQ). The anode was then slightly pressed on the filter strip at the acidic end of the IPG strip (marked with a “+”) and the cathode installed in the same way at the other end. The strip was then again covered with paraffin to prevent drying out and ensure good thermal conduction, since the device is cooled to constant 20 °C. The lid of the Multiphore II instrument was closed and a respective high voltage program for good isoelectric focusing was applied (see chapter 3.1.3).

After completion of the IEF, the electrodes and filter strips were removed and the IPG strip was shortly rinsed with UHQ and placed in a new tray for equilibration where it was covered with the Equilibration I – Reduction solution. After 15 min of incubation, the solution was replaced with Equilibration II – Alkylation and again incubated for 15 min.

The IPG strip was again rinsed with UHQ followed by shortening to a length of 6 cm from one or both ends in order to fit the 2D-well of the 4-12% Bis-Tris gel, details are given in chapter 3.1.3.

The secure strip of the NuPAGE 4-12% Bis-Tris 2D gel was removed and the gel was washed with UHQ prior to inserting in the XcellSureLock Mini Cell chamber. Running buffer was filled in both, the cathode and anode chamber and the shortened IPG strip was carefully placed in the 2D well.

Electrophoresis was carried out for approximately 50 min at a constant voltage of 200 V and an expected current of 100-125 mA/gel at the start and 60-80 mA/gel at the end of the electrophoresis.

## 2.8 Silver Staining/Destaining

### Working Solutions:

- Sensitation solution:  
0.02 g sodiumthiosulfate-5-hydrate in 100 ml UHQ
- Incubation solution:  
0.4 g silver nitrate in 100 ml UHQ
- Developing solution:  
5 g sodium carbonate and 100 µl of 35% formaldehyde solution in 250 ml UHQ

### Protocol:

Mass spectrometry compatible silver staining of polyacrylamide gels was performed according to Shevchenko et al. (1996).

Table 2: MS compatible silver staining

Step	incubation duration	Volume	Solution
Fixing	20 min	100 ml	50 % MeOH, 5% acetic acid in UHQ
Washing	10 min	100 ml	50 % MeOH in UHQ
Washing	2 h	100 ml	UHQ
Optional Washing	Over night	100 ml	UHQ
Sensitation	1 min	100 ml	Sensitation solution
Washing	2x 1 min	2x 100 ml	UHQ
Incubation	20 min (4°C)	100 ml	Incubation solution
Washing	2x 1 min	2x 100 ml	UHQ
Developing	Change solution several times until protein bands are satisfying visible	~ 100 ml	Developing solution
Stopping	3x 5 min	3x 100 ml	5 % acetic acid in UHQ
Storage		100 ml	1 % acetic acid in UHQ

For destaining of PA gels, they were incubated in a solution of 50 mM sodium thiosulfate and 15 mM potassium hexacyanoferrate until all silver spots had disappeared.

## 2.9 Enzymatic Digestion, Desalting and Preparation for MS

### Working Solutions:

- Buffer solution:  
100 mM ammonium hydrogen carbonate in UHQ at pH 8.5
- Reducing solution:  
10 mM DTT in Buffer Solution
- Alkylation solution:  
54 mM IAA in Buffer Solution, stored in the dark
- Digestion buffer:  
50% Buffer Solution and 5% ACN in UHQ
- Trypsin solution:  
12.5 ng/ $\mu$ l trypsin in Digestion Buffer
- Matrix solution:  
2 mg/ml  $\alpha$ -CHCA in 0.1% TFA/ACN (1:2)

### Protocol:

To avoid contamination by keratin, a human epidermal protein, gloves were worn at all times.

The gel was placed on a clean glass slide and protein bands of interest were excised, transferred in a 500  $\mu$ l sample vial and cut into roughly 1 mm<sup>3</sup> cubes by the use of a clean scalpel. The positions of the excised bands were marked on a prior obtained image of the gel.

To destain the gel pieces, they were washed two times with 10  $\mu$ l of 100 mM sodium thiosulfate and 10  $\mu$ l of 30 mM potassium hexacyanoferrate each for 15 min per change. The brownish color of the silver stain was completely removed by then.

All liquid was removed and 10  $\mu$ l of ACN was added for dehydration. After the gel pieces shrunk and became of milky coloring, the ACN was replaced by 10  $\mu$ l of buffer solution for rehydration. After 5 min, 10  $\mu$ l of ACN were added and incubated for 15 min. During the incubation time the samples were briefly vortexed for several times. After the incubation all liquid was removed and the gel particles were dried in a vacuum centrifuge. The dried gel particles were again rehydrated and the proteins were reduced by incubating for 45 min at 56 °C with 15  $\mu$ l of reducing solution. After reduction, the sample vials were quickly cooled down in the refrigerator and the excess liquid was spun down, replaced with 15  $\mu$ l of freshly

prepared alkylation solution and again incubated for 30 min at room temperature in the dark. The alkylation solution was then removed and 10  $\mu$ l of buffer solution were added. The Gel pieces were incubated for 5 min before 10  $\mu$ l of ACN were added and further incubated for another 15 min. During the incubation time the samples were again briefly vortexed for several times, followed by removing all liquid and drying the gel particles using a vacuum centrifuge. The dried gel particles were subsequently rehydrated for 45 min with 7-10  $\mu$ l of trypsin solution, depending on the size of the excised gel part. After incubation, the enzyme supernatant was replaced with 10  $\mu$ l of digestion buffer. The proteins were digested for 10 min at approximately 170 W in a domestic microwave oven followed by overnight digestion at 37 °C in the Thermomixer. After the digestion, the samples were cooled to room temperature and all liquid briefly spun down, followed by addition of 10  $\mu$ l ACN and incubation for 15 min. During the incubation time the samples were again briefly vortexed for several times. All supernatant was recovered and transferred in a new 500  $\mu$ l sample vial. This extraction was repeated two times with 5  $\mu$ l of 1% formic acid for 15 min and the addition of 5  $\mu$ l ACN for another 15 min. All recovered supernatants were pooled, followed by drying in the vacuum centrifuge. The extracted and dried peptide samples were stored at -20 °C.

For subsequent MS analysis, the samples had to be desalted and purified. Therefore they were redissolved by vortexing and sonication in 10  $\mu$ l of 0.1% TFA. ZipTip C18 pipette tips were prepared by wetting three times with 5  $\mu$ l of 0.1% TFA/ACN (1:1) and three times equilibration with 5  $\mu$ l of 0.1% TFA. The redissolved peptides were bound on the C18 material by sucking and eluting the peptide solution three times followed by washing the ZipTips three times with 0.1% TFA. The bound peptides were then eluted in new 500  $\mu$ l sample vials using three times 5  $\mu$ l of 0.1% TFA/ACN (1:1) followed by three times 5  $\mu$ l of 0.1% TFA/ACN (1:2).

The purified peptide solution was again dried in the vacuum centrifuge and redissolved in 2  $\mu$ l matrix solution by vortexing and sonication followed by brief centrifugation to gather all liquid at the bottom of the vial. All liquid was then transferred and tried on a spot of the MSP BigAnchor 96 BC Target for subsequent MS analysis.

## 2.10 MALDI-TOF/TOF-MS for Protein Identification

For protein identification the UltrafleXtreme (see chapter 2.2) was used. The instrument was calibrated each time before use with an external 100 fmol peptide standard containing the in Table 3 listed peptides solubilized in 0.1% TFA/ACN (1:2). The standard was mixed 1:1 with 4 mg/ml  $\alpha$ -CHCA matrix in 0.1% TFA/ACN (1:2) and 2  $\mu$ l were applied on a BigAnchor target.

Table 3: Peptide standard for MS instrument calibration

Calibration Peptides	$m/z$ of [M+H] <sup>+</sup> monoisotopic	[MH] <sup>+</sup>	Sequence
<b>Bradykinin 1-5</b>	573.310	C27H41N8O6	RPPGF
<b>Bradykinin 1-7</b>	757.400	C35H53N10O9	RPPGFSP
<b>Angiotensin 2</b>	1046.54	C50H72N13O12	DRVYIHPF
<b>Angiotensin 1</b>	1296.69	C62H90N17O14	DRVYIHPFHL
<b>Glu - 1 - fibrinogen</b>	1570.68	C66H96N19O26	EGVNDNEEGFFSAR
<b>N - acetyl - renin</b>	1800.94	C87H126N21O21	AcDRVYIHPFHLLVYS
<b>ACTH fragment 1-17</b>	2093.09	C95H146N29O23S	SYSMEHFRWGKPVGKKR
<b>ACTH fragment 18-39</b>	2465.19	C112H166N27O36	RPVKVYPNGAEDESAEAFPLEF
<b>ACTH fragment 7-38</b>	3657.93	C167H258N47O46	FRWGKPVGKKRRPVKVPNGAEDESAEAFPLE

### 2.10.1 Peptide Mass Fingerprinting

Peptide Mass Fingerprinting was carried out in reflectron mode for a  $m/z$  range of 500-3 760. The laser operated with a power of 28% and a global attenuator offset of 62% at 2 kHz. Mass spectra of approximately 8 000 selected laser shots were acquired and accumulated.

### 2.10.2 Peptide Sequencing

For peptide sequencing, PSD was performed. The acquired mass range depended on the selected precursor mass and the size of the ion gate was set to  $\pm 0.45\%$  of the precursor mass. In certain cases the ion gate had to be manually adjusted by narrowing, or asymmetrically shifting the passing  $m/z$  range in order to isolate monoisotopic  $m/z$  values. For fragmentation the laser operated at 50% increased power at 1 kHz. In general, mass spectra of 2 000 selected laser shots for the precursor ion and 6 000 selected laser shots for the fragment ions were acquired and accumulated.

### 2.10.3 Data Analysis

Acquired mass spectra were analyzed using flexAnalysis Version 3.4 (Build 70) by Bruker Daltoniks and implemented database search by Matrix Science (London, UK).

PMF mass spectra were smoothed using the software inherent Savitzky Golay algorithm with a  $m/z$  width of 0.2 for one cycle and baseline subtracted using TopHat algorithm. Monoisotopic peaks which showed a signal-to-noise ratio (S/N) of three or greater, were manually selected. Those monoisotopic peaks also present in mass spectra of likewise treated gel- and trypsin-blanks were subtracted to reduce false positive identification. The thereby generated

monoisotopic peak list was sent to Mascot search. The search parameters are shown in Table 4. Hereby the search was performed within two different databases. Firstly, the search was performed in the online database SwissProt. At the time, the search was performed, the database contained 96 892 sequences in correlation to amphibian, whereas only 379 sequences were in correlation to *P. shermani*. And secondly the search was performed in a specific NCBI database on the in-house server, which only contained sequences in correlation to amphibian.

Peaks of PSD spectra were automatically assigned using the software inherent "Snap Averagine" peak detection algorithm for a threshold of  $S/N \geq 3$  and after automatic smoothing using Savitzky Golay algorithm with a  $m/z$  width of 0.15 for four cycles and baseline subtraction using TopHat algorithm. The thereby generated mass list was then sent to Mascot search. The search parameters for the search are shown in Table 5 and the search was again performed in two different databases.

Table 4: Database search parameter for PMF

Category	1 <sup>st</sup> Search Parameter	2 <sup>nd</sup> Search Parameter
Database	SwissProt	NCBI (in-house server version)
Taxonomy	Metazoa	Amphibia
Enzyme	Trypsin	Trypsin
Fixed Modifications	Carbamidomethyl (C)	Carbamidomethyl (C)
Variable Modifications	Acetyl (Protein N-term), Carbamyl (N-term), Oxidation (M)	Acetyl (Protein N-term), Carbamyl (N-term), Oxidation (M)
Mass Values	Monoisotopic $MH^+$	Monoisotopic $MH^+$
Peptide Mass Tolerance	$\pm 0.3$ Da	$\pm 0.3$ Da
Max. Missed Cleavages	1	1

Table 5: Database search for PSD

Category	1 <sup>st</sup> Search Parameter	2 <sup>nd</sup> Search Parameter
Database	SwissProt	NCBI (in-house server version)
Taxonomy	Metazoa; Error Tolerant	Amphibia
Enzyme	Trypsin	Trypsin
Fixed Modifications	Carbamidomethyl (C)	Carbamidomethyl (C)
Variable Modifications	Acetyl (Protein N-term), Carbamyl (N-term), Oxidation (M)	Acetyl (Protein N-term), Carbamyl (N-term), Oxidation (M)
Mass Values	Monoisotopic $MH^+$	Monoisotopic $MH^+$
Peptide Mass Tolerance	$\pm 0.3$ Da	$\pm 0.3$ Da
Fragment Mass Tolerance	$\pm 0.5$ Da	$\pm 0.5$ Da
Max. Missed Cleavages	1	1
Instrument Type	MALDI-TOF-TOF	MALDI-TOF-TOF

## 2.11 MALDI – IM–MS Imaging

For IM-MS imaging experiments, the Synapt G2 HDMS (see chapter 2.2) was used. It was calibrated with an external 100 fmol peptide standard containing the peptides listed in Table 3 solubilized in 0.1% TFA/ACN (1:2). The standard was mixed 1:1 with 4 mg/ml  $\alpha$ -CHCA matrix in 0.1% TFA/ACN (1:2) and 2  $\mu$ l were applied on a steel target. The laser power was always set to 300, the quadrupole profile was set automatically according to the chosen m/z range, which was adjusted according to the experiment but never exceeded 3 760 m/z and the qRTOF operated in V-mode.

### 2.11.1 Evaluation of Ion Mobility Parameter

#### **Stock Solutions:**

- TOF<sup>2</sup>:  
500 fmol of each peptide in 0.1% TFA/ACN (1:2) according to Table 3
- PC:  
1 nmol of L- $\alpha$ -phosphatidylcholine in MeOH/chloroform (1:1)
- CBO:  
Approximately 1 nmol castor bean oil in MeOH
- CLP:  
1 nmol Cardiolipin (sodium salt) in MeOH
- $\alpha$ -CHCA:  
2 mg/ml  $\alpha$ -CHCA in 0.1% TFA/ACN (1:2)  
4 mg/ml  $\alpha$ -CHCA in 0.1% TFA/ACN (1:2)  
10 mg/ml  $\alpha$ -CHCA in 0.1% TFA/ACN (1:2)

#### **Protocol:**

Stock-Solutions were further diluted to various concentrations using 0.1% TFA/CAN (1:2). For MALDI-MS, standards were prepared using either the mixed-solvent-, thin-layer- or sandwich-method (Kusmann et al. 1997). For the mixed solvent method, either one standard was mixed 1:1 with 4 mg/ml  $\alpha$ -CHCA and 2  $\mu$ l were deposited on a spot of the stainless steel target, or 10 mg/ml  $\alpha$ -CHCA were mixed 1:1:1:1 with different concentrations of all four standards (TOF<sup>2</sup>, PC, CBO, CLP) and 2  $\mu$ l were deposited on a spot of the steel target, thus always depositing 4  $\mu$ g of matrix. For the thin-layer method, 1  $\mu$ l of 4 mg/ml  $\alpha$ -CHCA was placed on a spot of the steel target and allowed to dry at ambient room temperature, before 1  $\mu$ l of

standard was placed on top of the matrix layer. This was not only done for one standard but also for multiple layers of different standards, whereas the order of the applied standards differed. The thin-layer-sandwich method was prepared similar to the thin-layer method, differing in the use of 2 mg/ml  $\alpha$ -CHCA and the addition of a final matrix layer, representing a sandwich of matrix layers with the respective standards in between. Again the total amount of matrix was 4  $\mu$ g.

To evaluate the ion mobility parameters of IMS Gas Flow, IMS Wave Velocity and IMS Wave Height for good ion separation and mass spectrometric results, an evaluation grid was established correlating each parameter with each other.

After evaluation of the IM settings, sensitivity measurements were performed for optimized settings. Therefore for the lipid standards (PC, CBO, CLP) concentrations of 100 pmol, 10 pmol, 1 pmol, 500 fmol and 100 fmol were prepared by dilution of the working solutions with 0.1% TFA/ACN (1:2). For the peptide standard TOF<sup>2</sup>, concentrations of 100 fmol, 10 fmol and 1 fmol were also prepared in the same way. After determining the LOD for single standards using the mixed-solvent method ( $S/N \geq 3$ ), various mixtures of standards containing different concentrations were measured. The total amount of matrix on the target was always approx. 4  $\mu$ g.

CID experiments were performed with optimized IM settings. The collision energy in the Trap- or Transfer-TWIG thereby depended on the  $m/z$  value and was adjusted manually to obtain representative fragmentation spectra.

### 2.11.2 Sample Preparation for MALDI-IM-MS-Imaging

To evaluate the optimized Ion Mobility settings of 2.8 in aspect of MS imaging, samples were either prepared according to 2.11.1 or were simply pipetted in a given geometry on Aclar film cleaned with EtOH before use. This film was fixed on an ITO (indium tin oxide) target with conductive-adhesive double-sided tape (Shimadzu) before matrix was applied with a chemical inkjet printer on top (for Detail on printing see 2.11.2.2). Some samples were prepared by directly printing a standard in a given geometry on a, with EtOH cleaned ITO target, before again matrix was applied by means of printing.

For further biogluce analysis, Aclar film with dried salamander secret was fixed on the target using conductive, double-sided adhesive tape and again matrix was printed on top (see 2.11.2.2). Biological tissue samples were prepared according to the following chapter.

### 2.11.2.1 Tissue Preparation

#### **Protocol:**

Tissue samples attached to ITO glass slides, which were stored at -20 °C had to be washed prior to matrix application. The glass slide is carefully placed in a 50 ml falcon tube filled with cold acetone and bathed for 30 sec. After drying the slide under vacuum in a vacuum desiccator, two more bathing steps for 30 sec with 70% EtOH and 95% EtOH were performed and afterwards the slides were again dried under vacuum in a vacuum desiccator. A last bathing step for 30 sec was performed in a glass container of chloroform to avoid tissue detachment from the glass slide.

Matrix application on the tissue section was carried out with an airbrush-sprayer according to chapter 2.11.2.2.

### 2.11.2.2 Matrix Application for Imaging

#### **Working Solution:**

- Matrix for ChIP printer:
  - 5 mg/ml  $\alpha$ -CHCA in 0.1% TFA/ACN (1:2)
  - 8 mg/ml  $\alpha$ -CHCA + 8 mg/ml DHB in 0.1% TFA/ACN (1:2)
- Matrix for Airbrush:
  - 10 mg/ml  $\alpha$ -CHCA in 0.1% TFA/ACN (60:40)
  - 10 mg/ml  $\alpha$ -CHCA + 7.2  $\mu$ l/ml aniline in 0.1% TFA/ACN (60:40)

#### **Protocol:**

- ChIP printing:

Depending on the used solution, the applied pressure on the printing solution reservoir and the voltages on the piezoelectric printing head were adjusted to generate defined droplets of 100 pl with an average diameter of 55  $\mu$ m. The chosen printing pitch size and the amount of continuously deposited droplets on the same spot also depended on the used solution. The applied matrix concentration was calculated by the overall deposited amount of droplets.

- Airbrush:

The matrix solution was filled in the reservoir chamber of the airbrush and was then repeatedly sprayed on the target of interest at a distance of approx. 25 cm and an angle of approx. 60°. The applied matrix was allowed to dry between each spraying step. This matrix application method does not allow to deposit defined concentrations of matrix, but generates a homogeneous crystallization and benefits from its speed which reduces denaturation of biological tissue by enzymatic degradation or oxidation. The spraying steps were repeated until a homogenous matrix surface could be visually observed.

### 2.11.3 MALDI-IM-MS-Imaging Parameter

The laser-step-size in x- and y-direction and consequently the lateral resolution or pixel size differed on the kind of experiment and will be mentioned in Results and Discussion. Optimized IM parameters were used for the chosen m/z range (according to the results from chapter 3.2.1) and the acquisition time for each position on the tissue was set to 2 sec.

MALDI-IM-MS/MS imaging experiments for pre-defined masses were performed. The collision energies in the Trap- or Transfer-TWIG depended on the selected m/z values and were adjusted according to the results from chapter 3.2.2.

### 2.11.4 Data Analysis

To visualize the correlation of a mass spectrum with its corresponding drift time spectrum, DriftScope v2.1 by Waters was used. The intensity threshold was set to 5% counts of the most intense m/z value and the color palette "Hot Metal" was used where black represents no intensity and white represents 100% intensity.

Ion Mobility Imaging experiments were analyzed using HDImaging v1.0 and MassLynx v4.1 SCN870 both Waters. Parameters for processing had to be adapted individually.

CID mass spectra were analyzed using preferably the latest version of mMass (by Martin Strohal; [www.mmass.org](http://www.mmass.org)), which was mainly Version 5.5.0. Specific CID spectra were extracted from the data by selecting regions of ions with similar drift times with the software DriftScope. Peaks with a  $S/N \geq 3$  were assigned manually and the thereby generated mass lists were submitted to Mascot search with parameters listed in Table 6.

Table 6: Database search for CID

Category	Search Parameter
Database	NCBIInr
Taxonomy	All entries; Error tolerant
Enzyme	No Cleavage
Mass Values	Monoisotopic MH <sup>+</sup>
Peptide Mass Tolerance	± 0.3 Da
Fragment Mass Tolerance	± 0.5 Da
Max. Missed Cleavages	1
Instrument Type	MALDI-QUAD-TOF

## 3 Results and Discussion

### 3.1 Protein Analysis of Bioglue Samples Derived from *P. shermani*

Protein content of the secreted bioglue was analyzed by means of electrophoretic separation methods 1D-PAGE and 2D-PAGE. Identification of selected proteins was performed using PMF and peptide sequencing with MALDI-RTOF-MS, as previously described in chapter 1.5.

Further were preliminary results provided by Janek von Byern<sup>2)</sup>, regarding the overall amino acid composition of the bioglue sampled from several *P. shermani* individuals living in captivity. This sample should be identical to the glue-mixture sample used for protein identification in this chapter. A first overview of low MW molecules was also gained by Sophie Fröhlich<sup>1)</sup> using the Axima TOF<sup>2</sup> instrument. Those preliminary results are shown in chapter 1.1.1.

#### 3.1.1 Sample Preparation and Protein Concentration

In order to perform electrophoretic protein separation and subsequent protein analysis, a technique to completely dissolve the provided samples of secreted salamander glue had to be developed.

#### Secreted Salamander Bioglue on Aclar-film

As described in chapter 2.3 dried bioglue samples of the salamander secret from two different specimens were provided on Aclar-film (samples Aclar-1 and Aclar-2). The thickness and therefore amount of the deposited secret varied strongly over the surface of the Aclar-film. For the analysis, always an area of high bioglue density was chosen and excised using a sterile scalpel. The size of the excised area was determined with the help of a graph paper.

##### - Method A:

The first approach to dissolve the dried bioglue on the Aclar-film was performed according to Standard 1D SDS-PAGE procedures according to Laemmli (1970). Parts of the Aclar-film samples (approx. 1.50 cm<sup>2</sup> of Aclar-1 and approx. 1.25 cm<sup>2</sup> of Aclar-2) were cut into small pieces (1-4 mm<sup>2</sup>) with sterile scissors and transferred into 1.5 ml sample vials. 5 µl of NuPAGE LDS Sample Buffer (4x) and 5 µl of UHQ were added to each vial, followed by 5 min of sonication and subsequent heating at 70 °C for 5 min. 2 µl of NuPAGE Reducing Agent (10x) and 8µl UHQ were added and the samples were again sonicated for 5 min followed by heating at 70 °C for 5 min. Afterwards all liquid

was spun down. A non-used Aclar-film cleaned with EtOH (approx. 0.25 cm<sup>2</sup>) was used as blank and treated the same way (referred to as "Aclar-film blank 1").

The supernatant was withdrawn for subsequent 1D gel electrophoresis (see next chapter) but only 10 µl could be gathered due to loss by capillary effects between the small pieces of Aclar-film (from 20 µl in total). Since the amount of retrieved solution was too small, no protein concentration was determined. Furthermore, a sticky recess of probably not dissolved, rehydrated bioglue was observed (see Figure 23). Samples from this analysis will subsequently be annotated with "Aclar-1.1" & "Aclar-2.1".

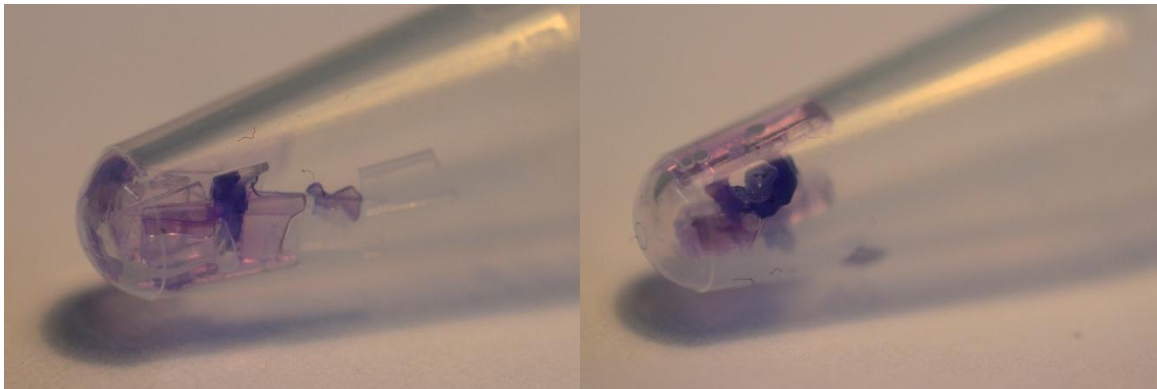


Figure 23: Sticky recess from Aclar-film after first dissolving approach

- Method B:

To prevent sample loss due to inseparable Aclar-film and sample solution, the Aclar-film pieces holding dried bioglue (approx. 1.5 cm<sup>2</sup> of Aclar-1 and approx. 1.5 cm<sup>2</sup> of Aclar-2) were carefully scratched off using a sterile spatula and transferred into 1.5 ml sample vials. Remaining bioglue recess on the Aclar-films was then washed in the vials with 10 µl of NuPAGE LDS Sample Buffer (4x)/UHQ (1/1), subsequently sonicated for 5 min and heated at 70 °C for 5 min. 2 µl of NuPAGE Reducing Agent (10x) and 8 µl UHQ were added and the samples were again sonicated for 5 min and heated (70 °C, 5 min). Afterwards the sample solution was spun down. Supernatant was withdrawn for subsequent 1D-gel electrophoresis and samples from this analysis will subsequently be annotated with "Aclar-1.2" & "Aclar-2.2".

It was observed that not all bioglue could be transferred from the Aclar-film into the vials and again a sticky recess of probably not dissolved, rehydrated glue could be observed after LDS buffer treatment. The amount of retrieved solution was again too low to

determine its protein concentration. A non-used Aclar-film cleaned with EtOH (approx. 0.25 cm<sup>2</sup>) was used as blank and treated the same way (referred to as "Aclar-film blank 2").

- Method C:

To avoid sample loss, further pieces of Aclar-film (approx. 0.75 cm<sup>2</sup> of Aclar-1 and approx. 0.75 cm<sup>2</sup> of Aclar-2) were cut in half and placed in 1.5 ml sample vials. 100 µl of NuPAGE LDS Sample Buffer (4x)/UHQ (1/1) were added to each vial, followed by 5 min of sonication and subsequent heating at 70 °C for 5 min. Then 100 µl of 100 mM DTT were added and again sonicated for 5 min followed by heating at 70 °C for 10 min. Afterwards the sample solution was spun down. Supernatant was withdrawn for subsequent 1D-gel electrophoresis and samples from this analysis will subsequently be annotated with "Aclar-1.3" & "Aclar-2.3".

Again a sticky recess could be observed. The protein concentration could not be determined at this point since the LDS Buffer interfered with both, the photometric BCA- and the Bradford-assay. A non-used Aclar-film cleaned with EtOH (approx. 0.75 cm<sup>2</sup>) was used as blank and treated the same way (referred to as "Aclar-film blank 3").

### **Mixed powder of secreted salamander glue**

Since dissolving of the bioglue directly from the Aclar-film samples resulted in not further analyzed debris, a method for the provided dried bioglue was established. This sample can be described as a white powder and consisted of a mixture of secreted bioglues from different specimen. The sample will further be annotated as "glue-mixture".

- Method D:

First the sample was stepwise dissolved in various solvents and buffers, representing a pre-fractionation of proteins according to their solubility.

To 14 mg of glue-mixture, 1 ml of 50 mM TRIS-HCl (pH 8.5) were added in a 1.5 ml sample vial followed by three cycles of sonication for 5 min each and subsequent vortexing. After that, a clear solution, a white, stiff, crystalline foam at the top and a white hydrogel-like recess at the bottom of the sample were observed. The clear solution may represent hydrophilic analytes. It was collected and a protein

concentration of 0.39 mg/ml was determined by photometric BCA assay. This sample is further referred to as "glue-mixture-1.1". For results of the BCA assay see Table 7 and Figure 24. Outliers of the calibration function were determined by residual-plot and are marked in red.

Table 7: BCA assay of glue-mixture-1.1

	absorption [A]		concentration [ $\mu\text{g/ml}$ ]
<b>blank</b>	0.311	0.313	<b>0</b>
<b>Std 125</b>	0.356	0.357	<b>125</b>
<b>Std 250</b>	0.421	0.413	<b>250</b>
<b>Std 500</b>	0.531	0.426	<b>500</b>
<b>Std 750</b>	0.64	0.642	<b>750</b>
<b>Std 1 000</b>	0.777	0.753	<b>1 000</b>
<b>Std 1 500</b>	0.954	0.97	<b>1 500</b>
<b>Std 2 000</b>	1.169	1.167	<b>2 000</b>
<b>glue-mixture-1.1 undiluted</b>	0.485	0.478	<b>0.39</b>
<b>glue-mixture-1.1 diluted 1:10</b>	0.282	0.328	--
<b>glue-mixture-1.1 diluted 1:20</b>	0.320	0.316	--

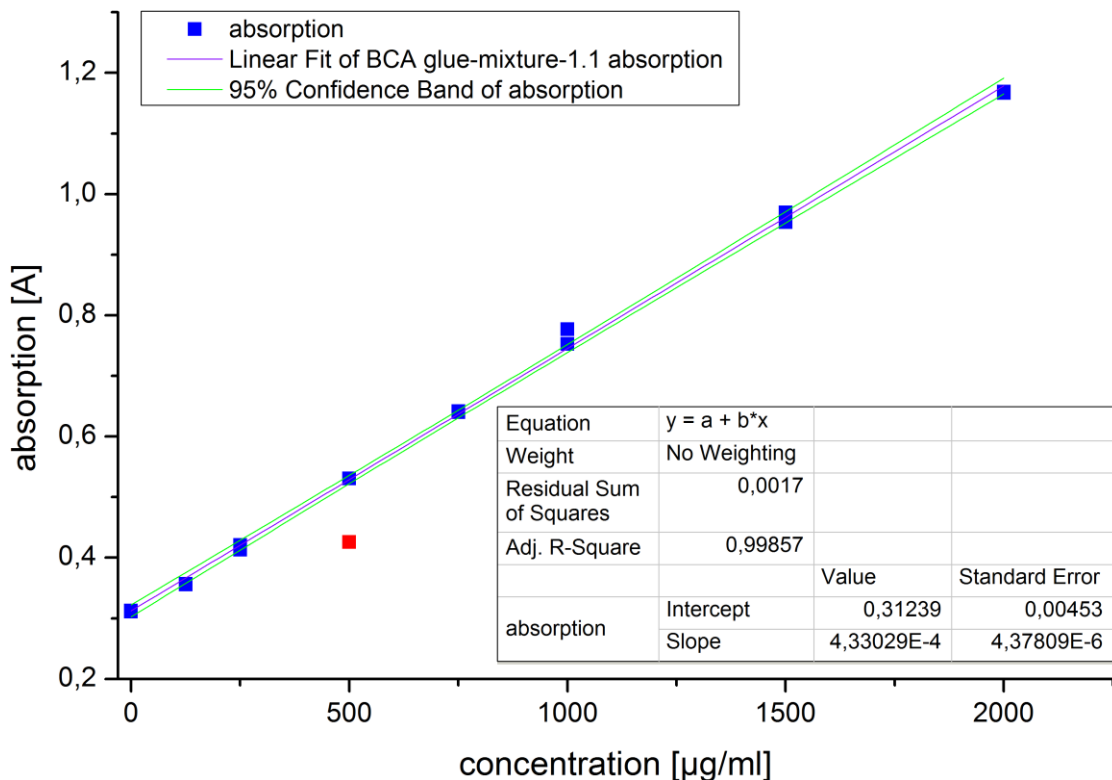


Figure 24: Standard calibration curve of BCA assay for glue-mixture-1.1

The recess of white crystalline foam and white hydrogel were further used to extract more hydrophobic analytes by the addition of denaturing reagents, detergents and chaotropic agents. These undissolved were accessed by the addition of 500  $\mu\text{l}$  of 5 mM DTT, 2 M thiourea, 7 M urea, 2% CHAPS and 50 mM TRIS-HCl (pH 8.5). After vortexing (2 times), the sample was sonicated for 5 min and heated at 70°C for 5 min and again sonicated for 30 min. This second dissolving step resulted in a clear solution and a now clear hydrogel-like recess with few black contaminations visible inside. The clear solution was recovered and yielded a protein concentration of approximately 1.35 mg/ml and is further referred to as “glue-mixture-1.2”. The protein concentration cannot directly be compared to sample “glue-mixture-1.1” as it was determined by the photometric Bradford assay since some of the chemicals were not BCA assay compatible. For results of the Bradford assay see Table 8 and Figure 25. Above a protein concentration of 750  $\mu\text{g/ml}$ , there was no more linear correlation between the concentration and the absorption. Those standards were therefore not included in the calibration function. Outliers of the calibration function were also determined by residual-plot and are marked in red. The absorption of the undiluted sample was too high and protein content is therefore based on sample dilution.

Table 8: Bradford assay of glue-mixture-1.2

	absorption [A]			concentration [ $\mu\text{g/ml}$ ]
<b>blank</b>	0.49	0.492	0.513	<b>0</b>
<b>Std 125</b>	0.594	0.606	0.582	<b>125</b>
<b>Std 250</b>	0.672	0.696	0.676	<b>250</b>
<b>Std 500</b>	0.882	0.906	<b>0.911</b>	<b>500</b>
<b>Std 750</b>	1.044	1.037	1.058	<b>750</b>
<b>Std 1 000</b>	<b>1.137</b>	<b>1.132</b>	<b>1.091</b>	<b>1 000</b>
<b>Std 1 500</b>	<b>1.19</b>	<b>1.177</b>	<b>1.196</b>	<b>1 500</b>
<b>Std 2 000</b>	<b>1.171</b>	<b>1.169</b>	<b>1.133</b>	<b>2 000</b>
<b>glue-mixture-1.2 undiluted</b>	<b>1.235</b>	<b>1.231</b>	<b>1.236</b>	<b>--</b>
<b>glue-mixture-1.2 diluted 1:2.5</b>	0.917	0.889	0.833	<b>1 295.19</b>
<b>glue-mixture-1.2 diluted 1:5</b>	0.697	0.71	0.708	<b>1 397.38</b>

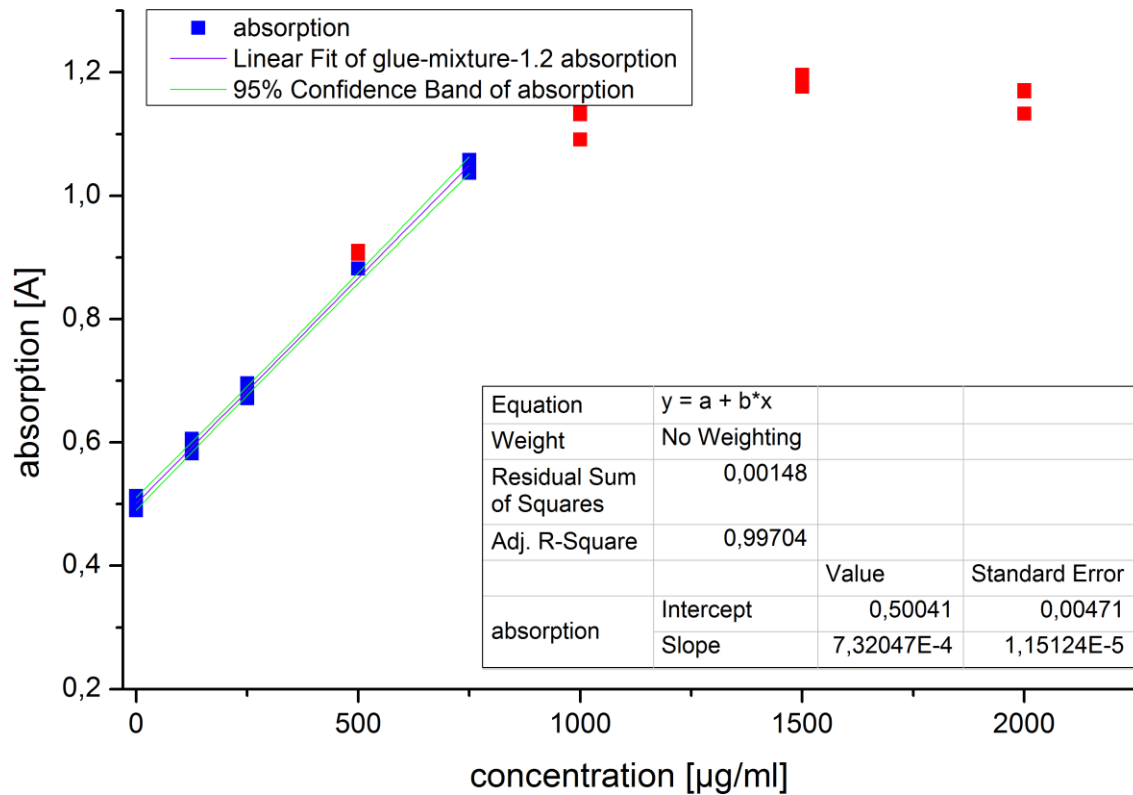


Figure 25: Standard calibration curve of Bradford assay for glue-mixture-1.2

To dissolve the last recess, the hydrogel-like debris, an adapted version of the filter aided sample preparation method described by Wisniewski et al. (2009) was performed. This method was chosen since it uses the help of the proteolytic enzyme trypsin as well as urea and IAA to destroy and dissolve strong hydrophobic structures like membranes. Since the recess showed a gel like behavior, the filter aided washing steps could not be performed in the published way due to complete blocking of the filter membrane. The recess was therefore incubated three times with 200 µl of 8 M urea and 50 mM TRIS-HCl (pH 8.5) in a 1.5 ml sample vial for 15 min each and the supernatant was transferred onto the same 10K microcentrifuge filter. After centrifugation at 15 000xg for 15 min, the flow-through was discarded. After this, the remaining recess of the hydrogel-like debris was treated three times with 200 µl of a solution containing 10 mg/ml IAA, 8 M urea and 50mM TRIS-HCl (pH 8.5) and as well as three times with 200 µl of a solution containing 50mM NH<sub>4</sub>CO<sub>3</sub>. The supernatant was thereby always transferred on the same 10K microcentrifuge filter as before, where it was centrifuged at 15 000xg for 15 min to retain proteins and remove buffer constituents. After these washing steps, the still remaining hydrogel-like debris was also transferred on the 10K microcentrifuge filter

and 100 µl of 10 ng/µl trypsin in 50 mM NH<sub>4</sub>CO<sub>3</sub>/ACN (19/1) were added followed by overnight incubation at 37°C. This last step dissolved all hydrogel-like debris and the remaining solution was then centrifuged through the membrane into a new collection vial at 15 000xg for 30 min. To gather all peptides, the filter was further washed two times for 15 min with 40 µl of 1% formic acid followed by the addition of 40µl of ACN for 15 min. The solution was then always centrifuged through the membrane into the same new collection vial as before at 15 000xg for 30 min.

Except for some small black particles remaining on the filter membrane, which were previously also visible in the hydrogel, no further debris could be observed. These black particles probably represent contamination introduced during sample collection but do not consist of proteins or alike and therefore were to be discarded. All other components of the hydrogel were supposed to be proteins as the residue was proteolytically degradable. Due to the cleavage into small peptides, the proteins can no longer be analyzed using gel electrophoresis. For this a LC-MS based method has to be developed, but this experiment was not carried out within the frame of the presented thesis.

Photometric absorption at 280 nm characteristic for aromatic amino acid residues yielded a rough estimation of 13.8 mg/ml for the protein concentration of the filtrate. This peptide solution is annotated as "glue-mixture-1.3"

- Method E:

Personal communication and only recently published data on the Australian frog *Notaden bennetti* and velvet worms regarding protein characterization (Graham et al. 2005; Graham et al. 2013), was basis for a different approach aiming at the complete dissolving of all present proteins. The data indicated that solubility could be improved using acetic acid and/or 2-mercaptoethanol.

To 7 mg of glue-mixture, 700 µl of 5% acetic acid were added, vortexed and sonicated which resulted in the formation of a hydrogel-like recess. 23 µl of 2-mercaptoethanol were added, representing a total of 3 Vol%, and heated at 99 °C for 4 min. The residue partially dissolved under these acidic conditions. To change the acidic- to an alkaline-milieu, 500 µl of rehydration buffer (see chapter 2.7) were added, which additionally introduced chaotropic agents and detergents for better solubility of hydrophobic

analytes. In order to maintain the level of reducing agent, another 23  $\mu\text{l}$  of 2-mercaptoethanol were added and then heated at 99 °C for 4 min three times, resulting in complete dissolving of the sample.

This approach showed that some sample components are more soluble at acidic conditions. The use of 2-mercaptoethanol as reducing agent also improves dissolving-behavior after reduction of the sample. 2-mercaptoethanol is also beneficial for gel electrophoresis since it is quite volatile and excess can therefor easily be removed. Completely dissolving the sample without enzymatic cleavage of the proteins also maintains the sample's compatibility for gel electrophoresis.

The protein concentration of the sample solution was determined again according to Bradford because some of the used chemicals were not BCA compatible. A concentration of approx. 4.38 mg/ml was determined and this sample solution is further referred to as "glue-mixture-2". For results of the Bradford assay see Table 9 and Figure 26. Above a protein concentration of 750  $\mu\text{g/ml}$ , there was no more linear correlation between the concentration and the absorption. Those standards were therefore not included in the calibration function. Outliers of the calibration function were also determined by residual-plot and are marked in red.

Table 9: Bradford assay of glue-mixture-2

	absorption [A]			concentration [ $\mu\text{g/ml}$ ]
<b>blank</b>	0.579	0.578	0.578	<b>0</b>
<b>Std 125</b>	0.694	0.691	0.703	<b>125</b>
<b>Std 250</b>	0.784	0.794	0.788	<b>250</b>
<b>Std 500</b>	0.951	0.955	0.927	<b>500</b>
<b>Std 750</b>	1.072	1.102	1.021	<b>750</b>
<b>Std 1 000</b>	1.122	1.111	1.096	<b>1 000</b>
<b>Std 1 500</b>	1.167	1.16	1.149	<b>1 500</b>
<b>Std 2 000</b>	1.182	1.182	1.177	<b>2 000</b>
<b>glue-mixture-2 diluted 1:10</b>	0.917	0.92	0.887	<b>4 557.98</b>
<b>glue-mixture-2 diluted 1:20</b>	0.777	0.74	0.739	<b>4 472.56</b>
<b>glue-mixture-2 diluted 1:40</b>	0.673	0.67	0.6698	<b>4 119.14</b>

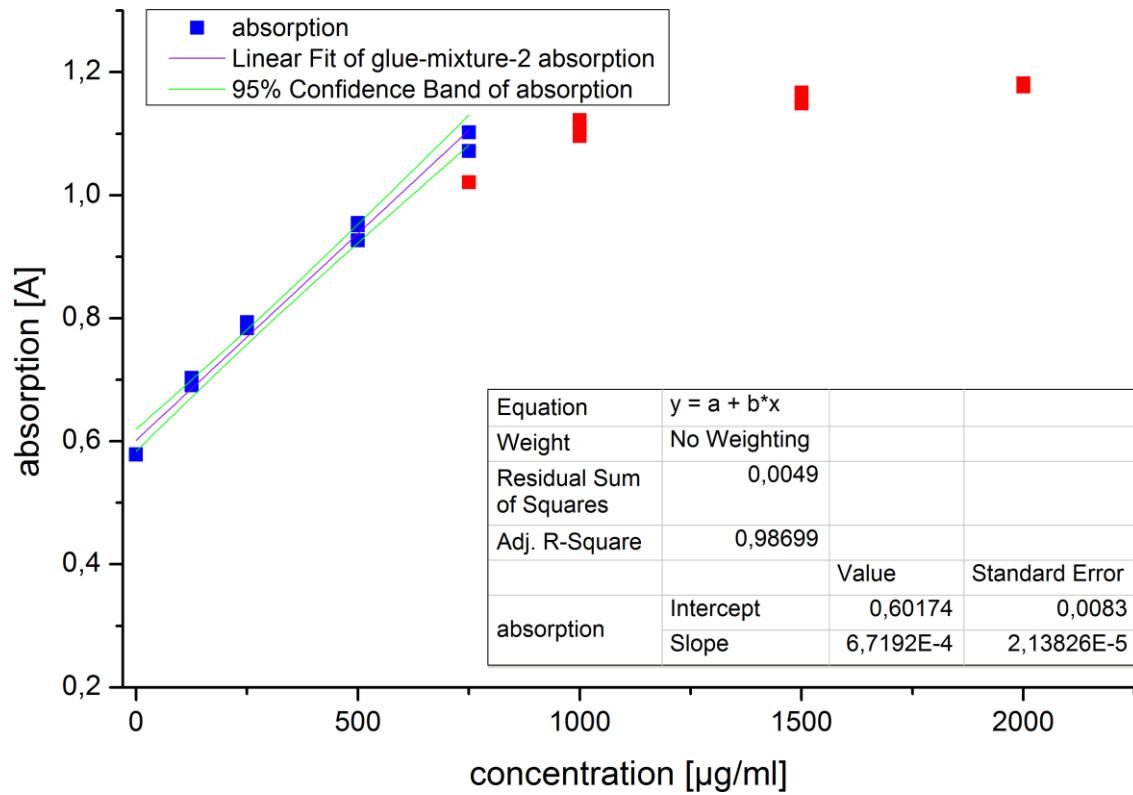


Figure 26: Standard calibration curve of Bradford assay for glue-mixture-2

An overview of all determined protein concentrations and the used photometric method is shown in Table 10.

Table 10: Overview of determined protein concentrations of biogluce samples and used photometric methods

	photometric method	protein concentration [mg/ml]
glue-mixture-1.1	BCA	0.39
glue-mixture-1.2	Bradford	1.35
glue-mixture-1.3	Absorption at 280nm	13.8
glue-mixture-2	Bradford	4.38

### 3.1.2 1D-PAGE

To separate the proteins of the salamander bioglue samples according to their MW, denaturing SDS PAGE was performed for all samples prepared as described in chapter 2.6.

Figure 27 shows images of the SDS-PAGE gels after silver staining (for protocol see 2.8) derived after protein separation of bioglue of two different specimen derived from Aclar-film. All samples were either prepared according to methods A or B (see previous chapter) whereas 1  $\mu$ l and 9  $\mu$ l of each sample were applied on the gel, since no protein concentration could be determined. Figure 27/a shows the image of the SDS-PAGE gel after the first staining cycle. It can be observed that the staining procedure was not sensitive enough to visualize all protein bands sufficiently, because of an overall short staining time since some of the gel lanes (for example 9  $\mu$ l of sample Aclar-1.1) were already intensively stained. Hereby the Sigma Marker was also not visualized, therefore the gel was destained (for protocol see chapter 2.8), followed by a second staining cycle. Removal of interfering substances and enhanced sensitization led to improved staining results as shown in Figure 27/c.

Even though the first staining was not sensitive enough it can already be observed that applying 9  $\mu$ l sample (for all applied samples) represents a concentration too high for good separation. This is especially observed for sample Aclar-2.1 and Aclar-2.2 showing both extensive smearing. Nevertheless, this effect can also slightly be observed for 1  $\mu$ l of Aclar-2.1. Another obvious observation is the variation of visualized protein bands for both specimens (Aclar-1 & Aclar-2). The prominent protein bands at approx. 30, 50, 75 and 100 kDa are present in samples from both specimens. But bands at approx. 60 kDa are differing: Aclar-1 shows two close protein bands, but three even better separated protein bands can be observed for Aclar-2. Aclar-2 also shows bands at MWs above 160 kDa, especially observed in the gel lane where only 1  $\mu$ l of sample Aclar-2.2 was applied. However, none of the applied samples could be dissolved completely, nor could their protein concentration be determined. Therefore it cannot be said if the differences in the visible protein bands result from sample preparation or due to the fact that samples Aclar-1 and Aclar-2 were gathered from two different specimens.

Figure 27/b shows an image of the Novex Pre-Stained Marker prior to silver staining. This image was used to correctly assign MWs, since the marker lane was contaminated with sample proteins, which are also visible after the second cycle of silver staining.

Low abundant proteins are more clearly visible after the second staining cycle and the MW marker is also visible. However, the second staining was too sensitive and protein bands cannot be distinguished clearly.

Nevertheless, after the second staining cycle, bands for the Aclar-film blanks are visible. Those bands can be protein contaminations originating from the clean Aclar-film, but since both blanks show different bands, which are moreover similar to their adjacent sample lanes, these protein bands were considered as cross contaminations from the actual samples.

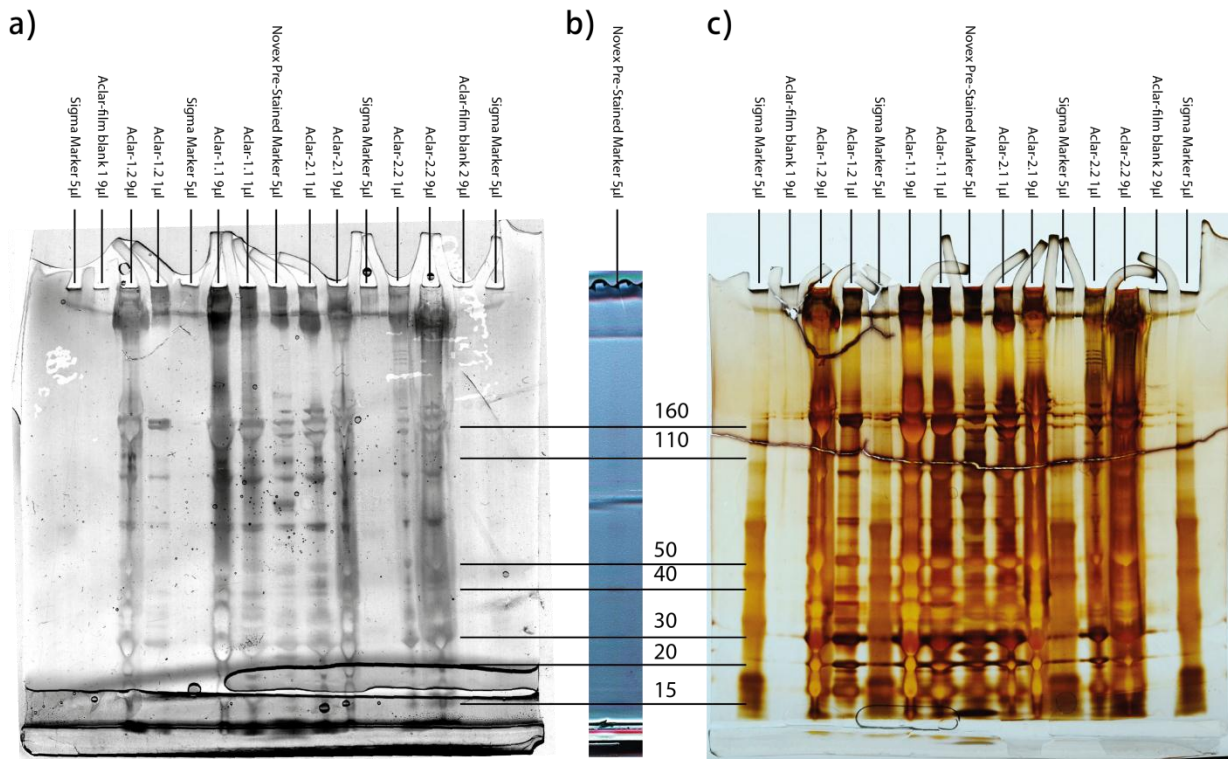


Figure 27: 1D-PAGE of samples from Aclar-1 and Aclar-2 as well as respective Aclar-film blanks prepared according to methods A and B; a) first silver staining cycle; b) pre stained marker before silver staining; c) second silver staining cycle with improved sensitivity

After these promising first results, samples were prepared according to method C resulting in less concentrated samples Aclar-1.3 and Aclar-2.3, whereas the same volume of sample solution (10 µl per sample) was applied on the PA gel. To prevent cross-contamination as described for the previous experiment and can be observed in Figure 27, sample was only applied in every second pocket of the gel. An image of the silver stained gel is shown in Figure 28.

In Figure 28 the most abundant proteins which were present in the previous results (see Figure 27), bands at approx. 35, 50 and 75 kDa, can again be observed for Aclar-1.3 and Aclar-2.3. Additionally the protein variability between the different specimens (Aclar-1 & Aclar-2) is again visible and is most prominent at 100 kDa. However it has to be mentioned that both patterns vary slightly from the protein patterns displayed in Figure 27. This can be explained by possible variations of sample distribution on the provided Aclar-films, as well as the facts that the samples were not completely dissolved and that different reducing agents and amounts of buffer solutions were used. This further demonstrates the importance of sample preparation. This figure further shows separated proteins of the first and second dissolving step from the glue-mixture sample prepared according to method D, which represents a biological average of *P. shermani* since it was collected from different specimens (see chapter 2.3). Since the sample solutions of the glue-mixture were not yet ready for electrophoretic separation, they were treated according to chapter 2.6 1D-PAGE. The importance of sample preparation can again be observed for glue-mixture-1.1 and glue-mixture-1.2 which were dissolved stepwise on purpose. Here the prominent protein band at approx. 140 kDa was almost completely dissolved using TRIS-HCl as buffer and is therefore mainly visible in glue-mixture-1.1 and not in the sample of the subsequent dissolving step (glue-mixture-2). This band is further interesting since it does not occur in the samples of individuals (Aclar-1 and Aclar-2), but is only present in the biological average.

Compared to Figure 27, the Aclar-film blank does not show any protein bands and therefore encourages the previous assumption of cross-contamination during the last analysis. Another observation from Figure 28 is that the load of MW marker had to be reduced as the respective protein bands were not clearly visible.

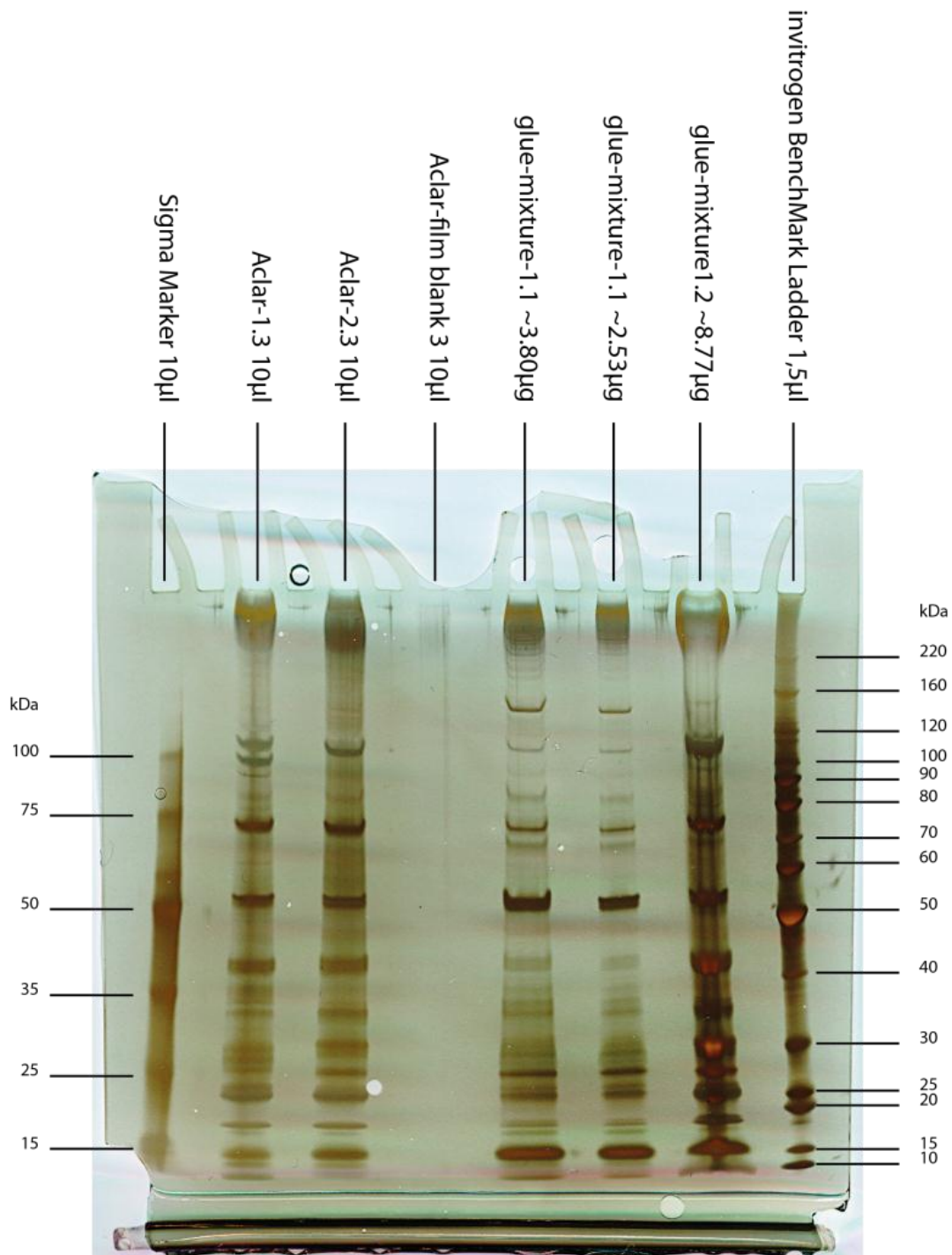


Figure 28: 1D-PAGE of samples from Aclar-1 and Aclar-2 prepared according to method C as well as samples from glue-mixture prepared according to method D (first and second dissolving step)

The importance of sample choice and sample preparation for the significance of gained 1D-PAGE results was already mentioned above. Based on latest published data and personal communication, a method (method E) was developed for completely dissolving a biogluce mixture, representing the biological average of two specimens (see chapter 3.1.1).

The electrophoretic protein separation of various concentrations of this sample is shown in Figure 29/b. Compared to method D that only partially dissolved the very same sample (Figure 29/a), it is obvious that a lot more protein bands were visualized. The high intensity of certain protein bands at 35, 50 and 75 kDa is no longer observed when compared to the additionally extracted proteins. Only the protein band at 100 kDa shows significantly higher staining efficiency. In addition to this, two more distinctive bands at approx. 20-25 kDa can be observed. For every other protein the intensity of the staining is very similar, preventing the differentiation of individual protein bands.

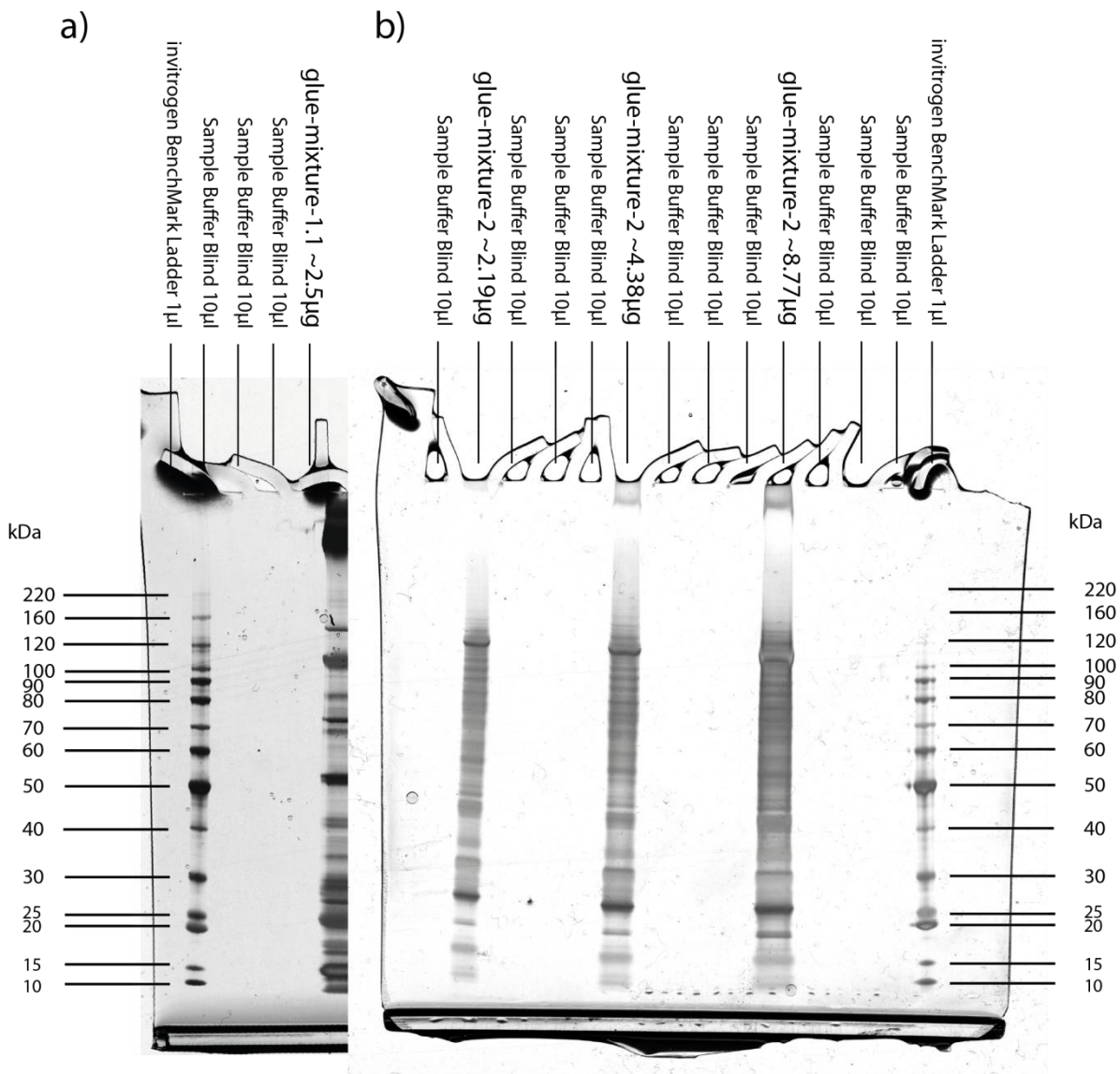


Figure 29: 1D-PAGE of glue-mixture samples; a): first step of the partial dissolved glue-mixture according to method D; b) different concentrations of glue-mixture sample prepared according to method E

### 3.1.3 2D-PAGE

For better protein separation of the glue-mixture samples, which represent a biological average of the secret by *P. shermani*, 2D-PAGE was performed.

Figure 30/a shows the silver stained gel after two-dimensional separation of glue-mixture-1.2 which was acquired after separating the sample according to chapter 2.7. The corresponding pH-gradient of the used IPG-strip is displayed above the 2D-gel image and the set voltage program for isoelectric focusing as well as the actual progress of voltage and current is shown in Figure 31. Figure 30/b further shows the 1D-PAGE of the same sample for better comparison with previous results. Prominent bands at 15, 25 and 30 kDa can be observed in both gels, while protein bands at higher MW are only present in the 1D-PAGE. There are various possible explanations for this observation. One possibility is the fact that these proteins are either very acidic or very alkaline and were therefore removed when the IPG-strip was shortened to fit in the pocket of the 2D-PAGE (0.8 cm from the acidic and 0.4 cm from the alkaline end corresponding to pI 3.0-3.5 and 8.8-11 respectively). However, it cannot be neglected that the IPG-strip was already past its expiring date before deployment. Therefore mobility for larger proteins could be limited, leading to precipitation. Those proteins were therefore not entering the second dimension. This assumption of precipitation is encouraged by the observation of white colored areas in the IPG-strip after electrophoretic focusing. Additionally the maximum current of 50  $\mu$ A was quickly reached which restricted voltage increase (see Figure 31), therefore hampering protein separation. The result of protein precipitation and limited voltage during the first dimension led to insufficient protein separation and most of the proteins are only partially resolved (horizontal streaking) as visualized in Figure 30/a.

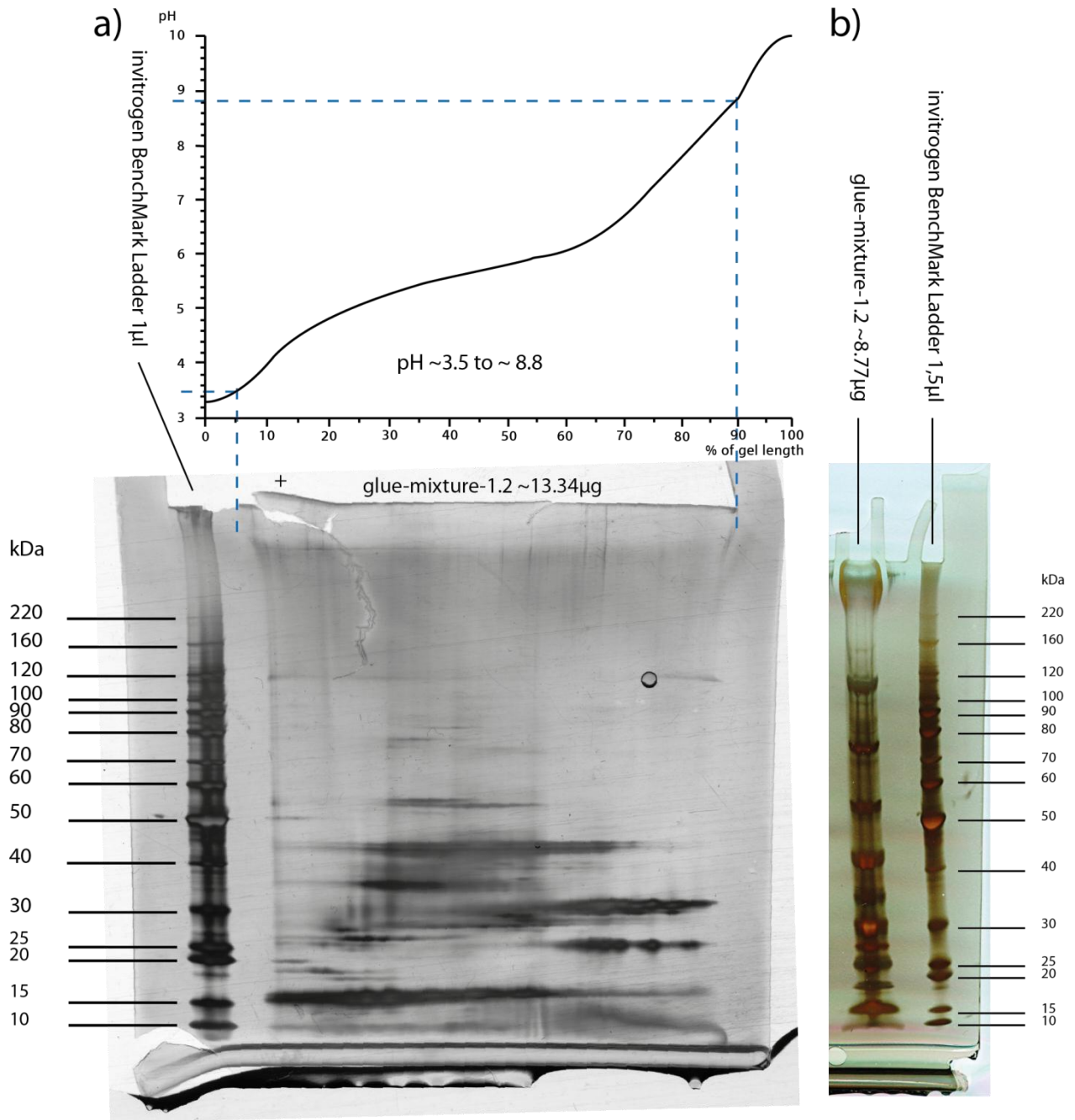


Figure 30: a) 2D-PAGE of glue-mixture-1.2; b): corresponding 1D-PAGE of glue-mixture-1.2

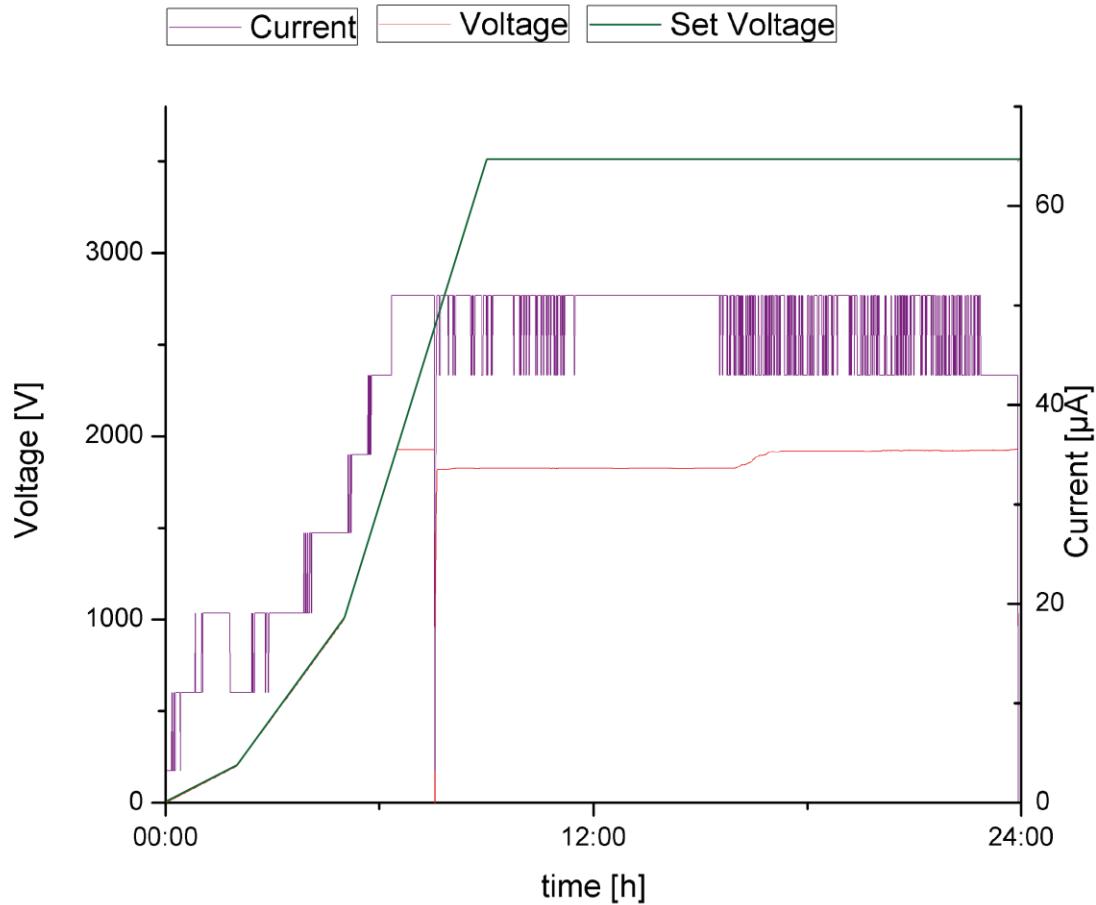


Figure 31: Voltage and current progress during IEF corresponding to Figure 31

In a second experiment a freshly bought IPG strip was used and the very same sample was applied (glue-mixture-1.2). The silver stained gel is shown in Figure 32, which also shows the pH-gradient of the used IPG-strip and the 1D-PAGE of the same sample for comparison. This 2D-PAGE shows now defined protein-spots at alkaline pIs with MWs from 20 kDa to 30 kDa. However, the more acidic protein fraction shows again horizontal streaking for the low MW proteins. The distorted protein pattern in combination with the horizontal streaking can be explained by non-protein impurities in the sample. Nevertheless for this sample again no protein-spots exceeding a MW of 50 kDa were observed. Again the maximum current of 50 µA was quickly reached which restricted voltage increase, therefore hampering protein separation (see Figure 33).

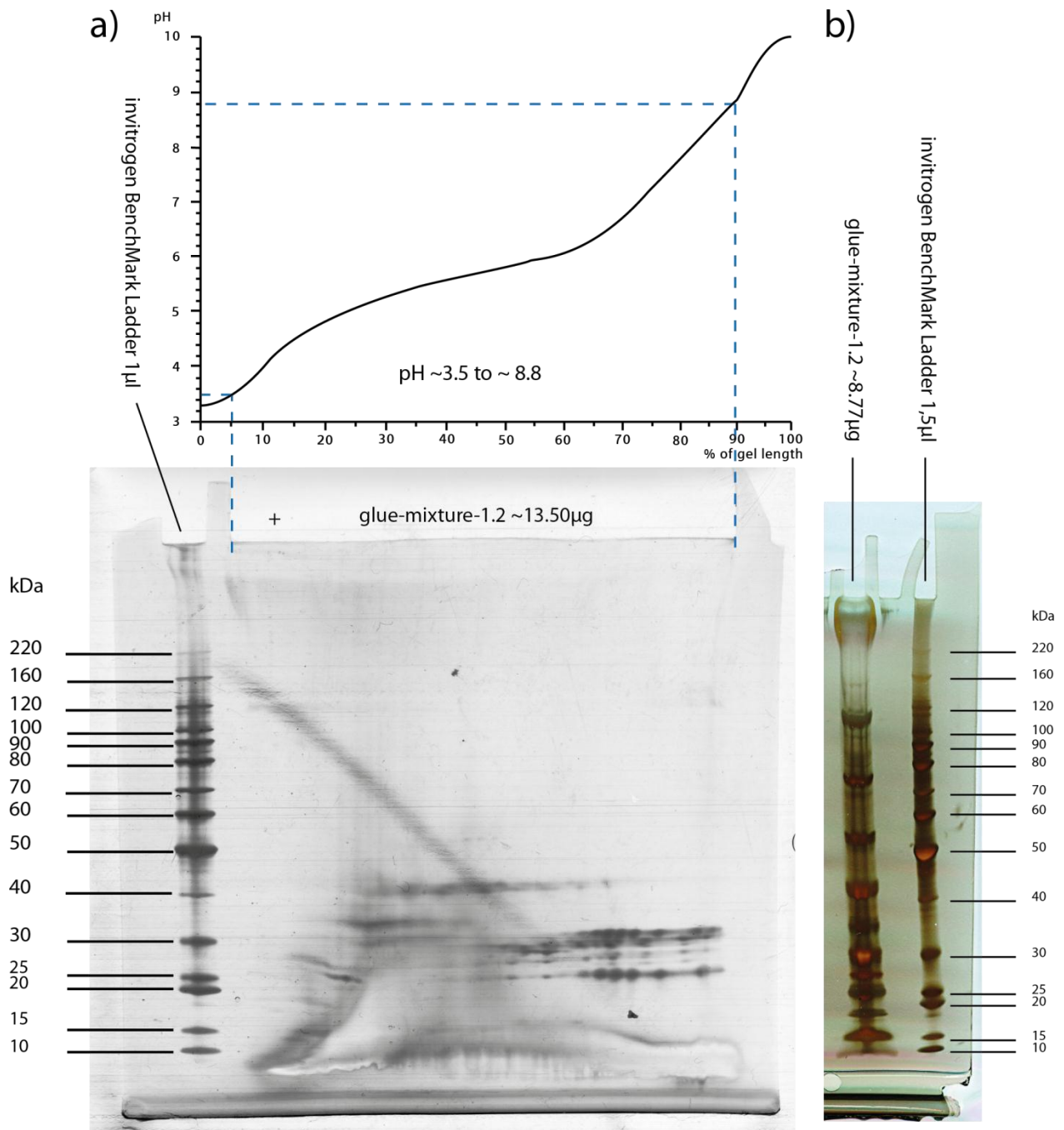


Figure 32: a) 2D-PAGE of glue-mixture-1.2; b): corresponding 1D-PAGE of glue-mixture-1.2

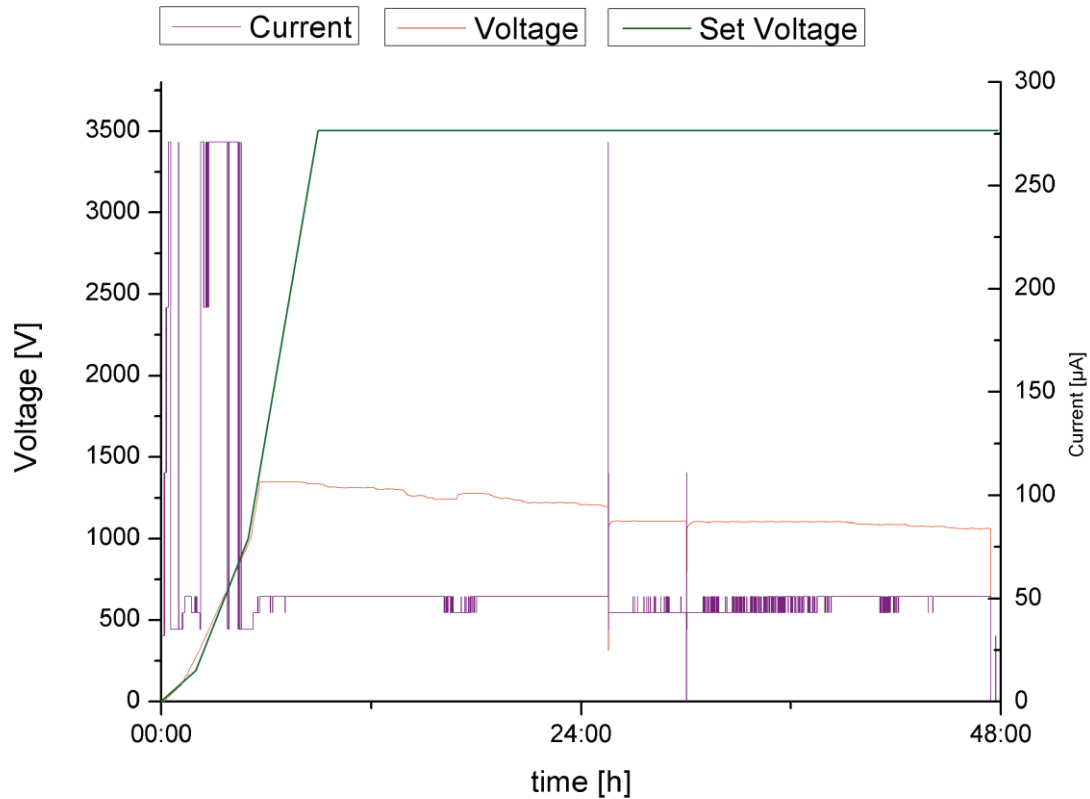


Figure 33: Voltage and current progress during IEF corresponding to Figure 32

Since no sufficient 2D-PAGE separation could be accomplished for glue-mixture-1.2 using a TRIS-HCl buffer containing DTT, urea, thiourea and CHAPS for dissolving, glue-mixture-2 was also separated on a 2D PAGE for comparison. This sample was prepared using method E where the complete sample was dissolved in one single step. Figure 35 shows the applied set voltage program for isoelectric focusing as well as the actual progress of voltage and current. It can be observed that the isoelectric focusing was performed for 45.5 h in order to reach the necessary electric potential energy. The necessity of such a long focusing time led again to the assumption of protein precipitation, confirmed by the white colored areas in the middle of the IPG-strip (see Figure 34). Beside this, a high number of protein-spots with apparent molecular masses beyond 50 kDa can be observed even though protein precipitation occurred. Nevertheless, electrophoretic focusing was hampered in the area of protein precipitation. Figure 32 shows that the majority of present proteins have rather basic isoelectric points, therefore it has to be mentioned that this time the IPG-strip was only shortened at the acidic end. Furthermore it was observed that protein spots successfully separated in the first dimension at approx. 10 to 35 kDa correspond nicely with the prominent protein bands of the 1D-PAGE.

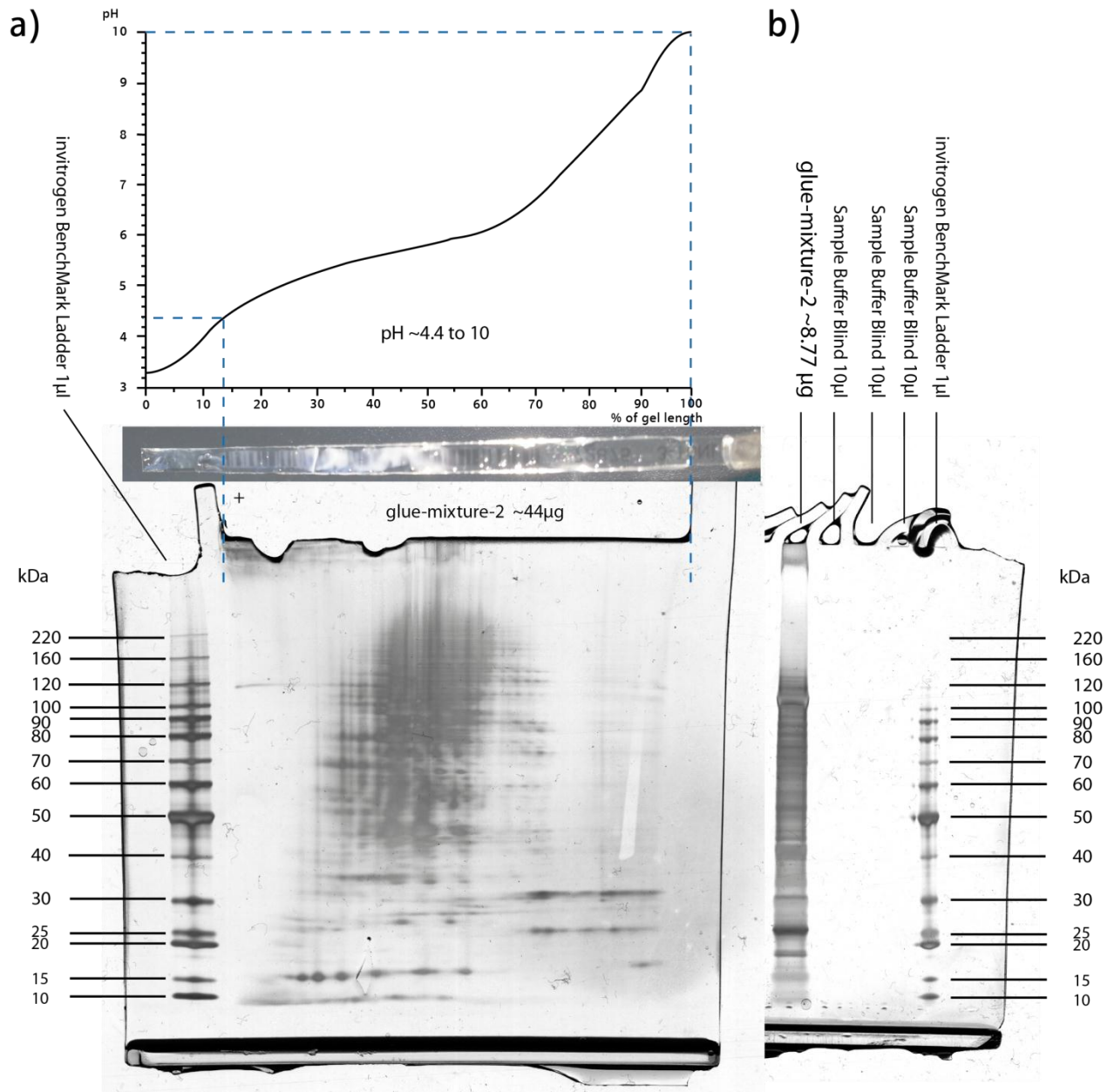


Figure 34: a) 2D-PAGE of glue-mixture-2; b): corresponding 1D-PAGE of glue-mixture-2

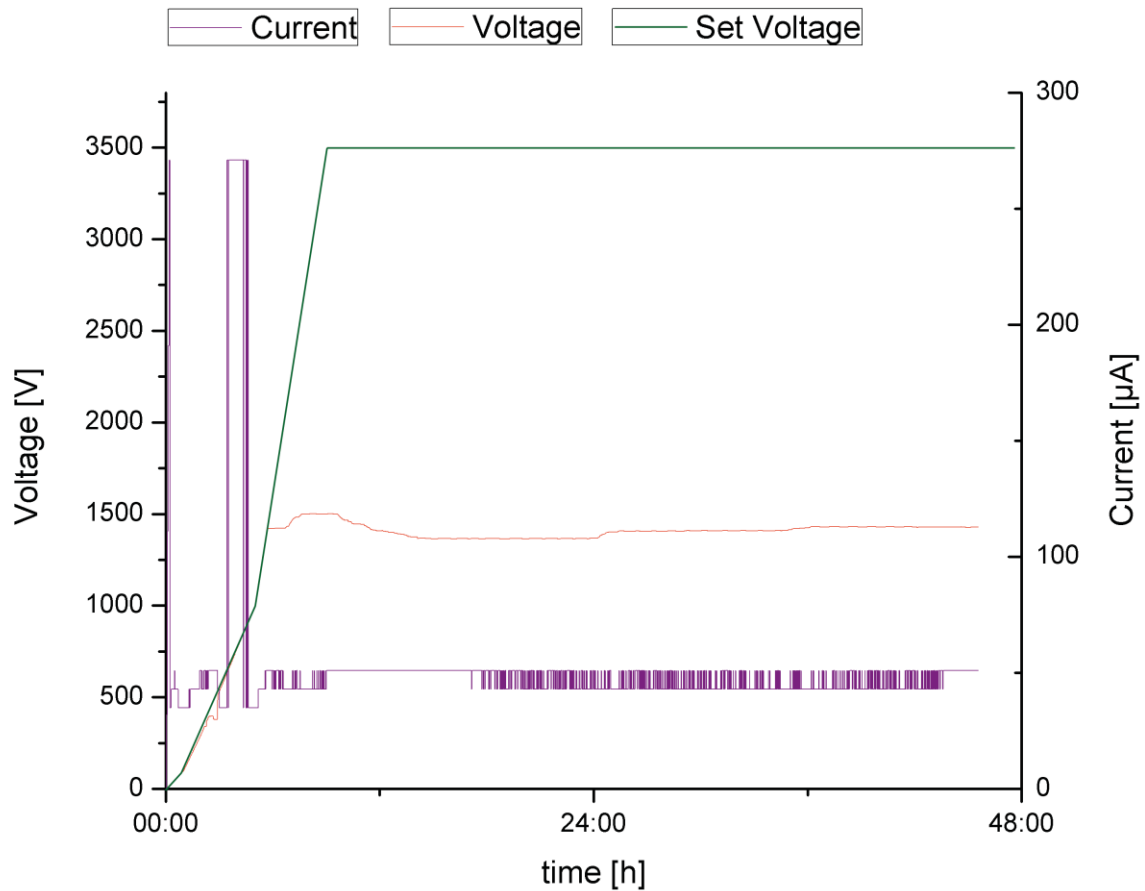


Figure 35: Voltage and current progress during IEF corresponding to Figure 35

This 2D-PAGE was subsequently used for protein identification. Defined protein spots, which are marked in Figure 36, were excised and enzymatically digested according to the protocol given in chapter 2.9. Furthermore Figure 36 shows the estimated MW and pIs of the excised protein spots based on their position on the 2D-PAGE.

Unfortunately some of the excised spots were disadvantageously chosen. A consecutive series of spots exhibiting the same MW but different pIs are very likely protein isoforms differing only in a few amino acids or post-translational modifications. Since PMF based protein identification relies on existing database entries, spots with a rather large pI difference like "5a" and "5b" should be chosen to increase the number of identified proteins. However, choosing spots with small pI differences increases the chance to identify the protein (if all spots belong to the same protein) as one of the isoforms may be closely related to respective database entries.

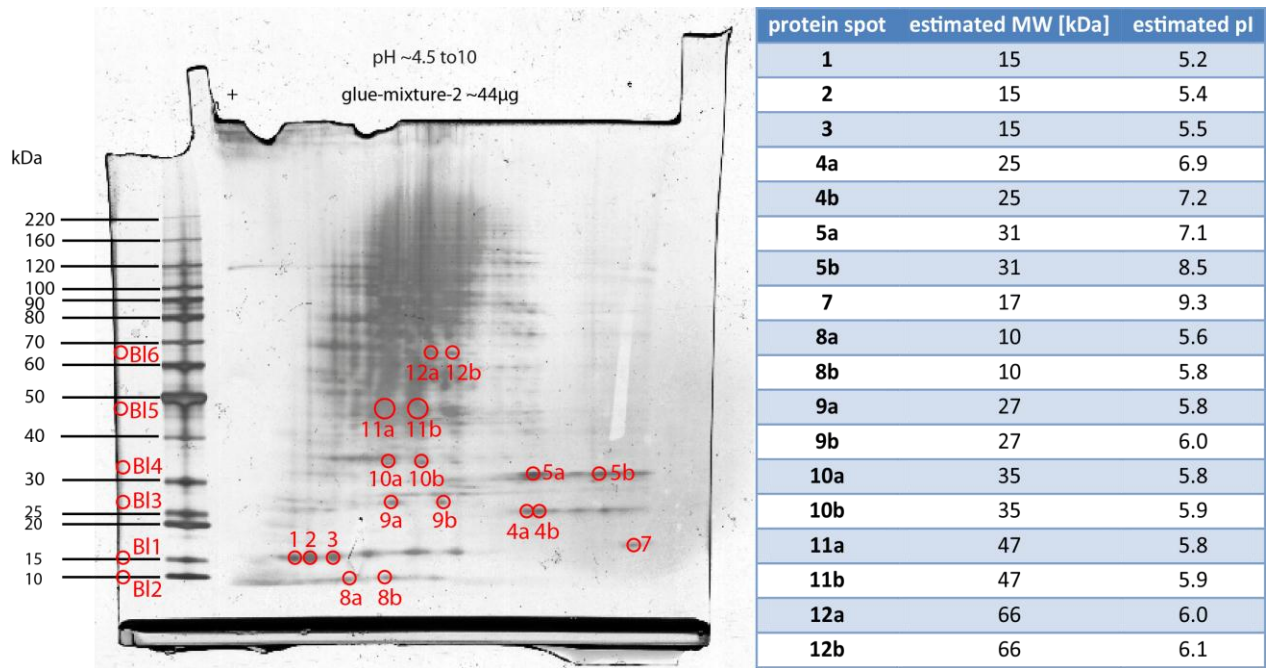


Figure 36: Marked protein spots which were excised for protein identification and their corresponding MW and pI

For all excised spots, mass spectra were acquired for PMF, and MS/MS spectra of the most intensive peptide signals (not belonging to the gel blank, trypsin or keratin contaminations) were used for peptide sequencing.

The genome of *P. shermani* is not completely sequenced and yet so far not many proteins are present in the database, therefore only three spots could be significantly assigned with a threshold exceeding a statistical p-value of 0.05 which are shown in Table 11.

Table 11: Protein spots with positive identification

Protein Spot	DB	Score/TH <sup>3)</sup>	theoretical MW [kDa]	MW on gel [kDa]	Protein Name	DB ID		
<b>4b</b>	Swiss Prot	<b>70/63</b>	<b>32.134</b>	~25	<b>Oxidative stress-responsive serine-rich protein 1</b>	<a href="#">OSER1_PONAB</a>		
						NCBI BLAST for amphibia	57% identity to <i>Xenopus tropicalis</i>	<a href="#">gi 45360461 ref NP_988917.1 </a>
						NCBI BLAST for plethodontinae	32% identity to <i>Plethodon kisatchie</i>	<a href="#">gi 392055855 AFM52279.1</a>
<b>10b</b>	Swiss Prot	<b>69/63</b>	<b>19.507</b>	~35	<b>Centrin-3 OS=<i>Mus musculus</i></b>	<a href="#">CETN3_MOUSE</a>		
						NCBI BLAST for amphibia	90% identity to <i>Xenopus tropicalis</i>	<a href="#">gi 62858487 ref NP_001016387.1 </a>
						NCBI BLAST for salamander	29% identity to <i>Plethodon chlorobryonis</i>	<a href="#">gi 124246580 ABM92692.1</a>
<b>12b</b>	Swiss Prot	<b>65/63</b>	<b>18.382</b>	~66	Peptidyl-prolyl cis-trans isomerase A-like 4G	<a href="#">PAL4G_HUMAN</a>		
						NCBI-BLAST for amphibian	63% identity to <i>Xenopus laevis</i>	<a href="#">gi 157423022 AAI53776.1</a>
						NCBI-BLAST for salamander	82% identity to <i>Ambystoma tigrinum</i>	<a href="#">gi 67528120 AAY68418.1</a>

For the PMF of protein spot “4b” the “oxidative stress-responsive serine-rich protein1” of *Pongo abelii* could be assigned with a significant Mascot score of 70 (see Figure 37). *Pongo abelii* itself is an orangutan species, but using a Basic Local Alignment Search Tool (BLAST) by NCBI, a sequence similarity of 57% with the well-studied western claw frog *Xenopus tropicalis* could be found for this protein. Furthermore *X. tropicalis* belongs also to the class of amphibia indicating a relation to *P. shermani*. Performing BLAST search in comparison to *plethodontinae* 32% identity was revealed for the same protein in *P. kisatchie*. This means the sequence for this protein is highly conserved and almost identical for many species. For this it can be considered a correct identification for *P. shermani*. As the name of the protein already indicates, it is correlated to stress. The biogluce secretion of the salamander as a defense mechanism is kind of a stress-trigger, therefore it is likely to be the protein variant in *P. shermani*. Additionally the MW of 32 kDa for this database entry is similar to the MW of protein spot “4b” which further strengthens this assumption. Unfortunately, peptide fragmentation of protein spot “4b” did not result in confirmation of the “oxidative stress-responsive serine-rich protein1”, but since amino acid exchanges and PTMs influence the fragmentation pattern, possible identification by database comparison is decreased.

<sup>3)</sup> TH... threshold for results with a significance exceeding a p-value of 0.05

BLAST results, MS and MS/MS data of protein spot "4b" used for PMF and peptide sequencing as well as their corresponding Mascot search results, can be found in the attached data files.

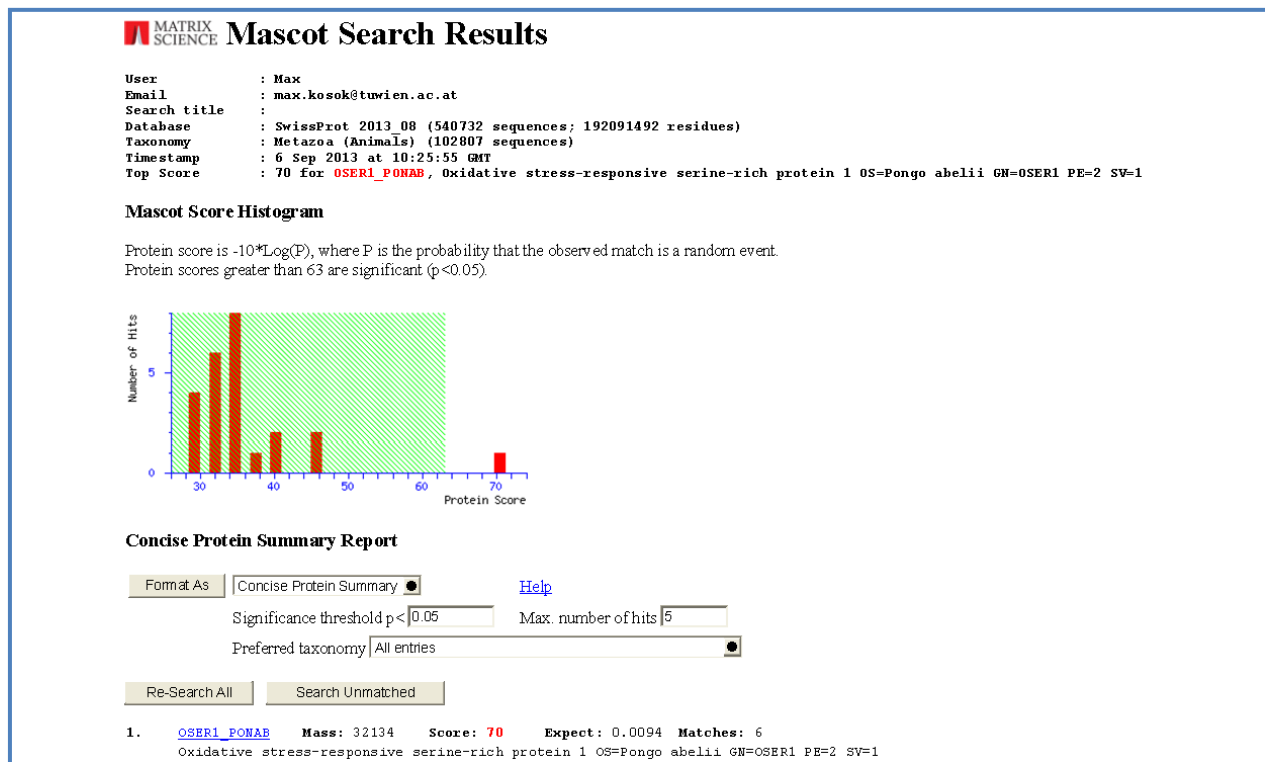


Figure 37: Mascot search result for protein spot "4b"

For the PMF of protein spot "10B", "Centrin-3" of *Mus musculus* could be assigned with a significant Mascot score of 69 (see Figure 38). *Mus musculus* itself belongs to the class of mammalia, but using BLAST again, a similarity of 90% with the same western claw frog *Xenopus tropicalis* could be found. A similarity of 29% to the protein variant in *Plethodon chlorobryonis* strengthens the assumption of similarity. Centrins are evolutionary highly conserved proteins and occur in the cytoplasm and cytoskeleton of eukaryotic cells. Since the glue collection occurred by applying slight mechanical force with tweezers on the animal, it is possible that such proteins were additionally secreted. Unfortunately, peptide fragmentation of protein spot "10b" did not result in confirmation of the "Centrin-3" because of the reasons mentioned before. The MW of 20 kDa for Centrin-3 is also smaller than the observed MW on the gel.

BLAST results, MS and MS/MS data of protein spot "10b" used for PMF and peptide sequencing as well as their corresponding Mascot search results, can be found in the attached data files.

## MASCOT SCIENCE Mascot Search Results

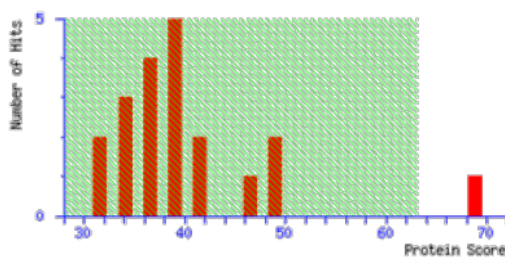
User : Max  
Email : max.kosok@tuwien.ac.at  
Search title :  
Database : SwissProt 2013\_09 (540958 sequences; 192206270 residues)  
Taxonomy : Metazoa (Animals) (102854 sequences)  
Timestamp : 15 Oct 2013 at 15:09:17 GMT  
Top Score : 69 for **CETN3\_MOUSE**, Centrin-3 OS=Mus musculus GN=Cetn3 PE=2 SV=1

### SwissProt [Decoy](#)

Protein hits above identity threshold	1	0
Highest scoring protein hit	69	52

### Mascot Score Histogram

Protein score is  $-10 \cdot \log(P)$ , where  $P$  is the probability that the observed match is a random event.  
Protein scores greater than 63 are significant ( $p < 0.05$ ).



### Concise Protein Summary Report

Format As  [Help](#)

Significance threshold  $p <$   Max. number of hits

Preferred taxonomy

1. [CETN3\\_MOUSE](#) Mass: 19507 Score: **69** Expect: 0.013 Matches: 7  
Centrin-3 OS=Mus musculus GN=Cetn3 PE=2 SV=1

Figure 38: Mascot search result for protein spot "10b"

For the PMF of protein spot "12b", the human "peptidyl-prolyl cis-trans isomerase A-like 4G" protein could be assigned with a significant Mascot score of 65 (see Figure 39). Using BLAST again, a similarity of 63% with yet another western claw frog *Xenopus laevis* could be found. A similarity of 29% to the protein variant in *Ambystoma tigrinum* strengthens the assumption of similarity. The identified protein belongs to the family of cyclophilin-type PPIase occurring in various isoforms throughout the cells of vertebrates. Again it is possible that such proteins were additionally secreted, but peptide fragmentation of protein spot "12b" did not result in confirmation because of the reasons mentioned before. The MW of 18 kDa is also smaller than the observed MW on the gel.

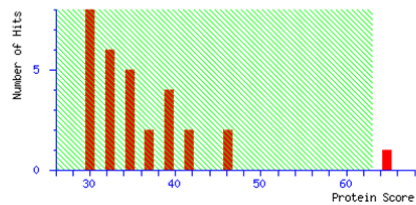
BLAST results, MS and MS/MS data of protein spot "12b" used for PMF and peptide sequencing as well as their corresponding Mascot search results, can be found in the attached data files.

## MATRIX SCIENCE Mascot Search Results

User : MaxK  
Email : max.kosok@tuwien.ac.at  
Search title :  
Database : SwissProt 2014\_01 (542258 sequences; 192776118 residues)  
Taxonomy : Metazoa (Animals) (103088 sequences)  
Timestamp : 17 Feb 2014 at 14:17:21 GMT  
Top Score : 65 for **PAL4G\_HUMAN**, Peptidyl-prolyl cis-trans isomerase A-like 4G OS=Homo sapiens GN=PPIAL4G PE=2 SV=1

### Mascot Score Histogram

Protein score is  $-10 \cdot \log(P)$ , where P is the probability that the observed match is a random event. Protein scores greater than 63 are significant ( $p < 0.05$ ).



### Concise Protein Summary Report

Format As  [Help](#)  
Significance threshold  $p <$  Max. number of hits   
Preferred taxonomy

1. [PAL4G\\_HUMAN](#) Mass: 18382 Score: **65** Expect: 0.035 Matches: 5  
Peptidyl-prolyl cis-trans isomerase A-like 4G OS=Homo sapiens GN=PPIAL4G PE=2 SV=1

Figure 39: Mascot search result for protein spot "12b"

An extensive table with a summary of all analyzed protein spots and their mass spectra which were used for PMF and peptide sequencing as well as their corresponding Mascot search results can be found in the attached files. Further were all mass lists of MS and MS/MS experiments saved, Mascot search can be repeated in the future, after for example the genome of *P. shermani* has been sequenced.

### 3.1.4 Summary & Conclusion

Summarizing the protein analysis of biogluce samples derived from *P. shermani*, it could be observed that the protein content of the expressed biogluce varied between individual salamanders. It is assumed that only certain proteins are responsible for the gluing effect. The main task for future analysis is therefore to identify those proteins occurring in all *P. shermani* specimens, which is why samples representing a biological average were chosen for protein analysis in this thesis.

It also could be shown that the sample preparation protocol has a major influence on the solubility of proteins. It was found, that completely dissolving the biological glue samples in one step, using 2-mecaptoethanol as reducing agent in an acidic and alkaline milieu is the easiest way to gain reproducible results. Since the protein content in the biogluce appeared to be very high according to photometric assays and 1D-PAGE, 2D-PAGE was chosen for better protein separation. Separation by 2D-PAGE still has to be improved, but already resulted in an acceptable separation to perform protein analysis by MS.

This resulted in the significant identification of three proteins. Firstly the “oxidative stress-responsive serine-rich protein1” (*Pongo abeli*) which shows 57% identity with the protein variant from *Xenopus tropicalis* and 32% identity with the protein variant in *Plethodon kisatchie*, was identified exhibiting an apparent MW similar to database entries. We hypothesize to have identified the *P. shermani* variant of this protein. Secondly “Centrin-3”, an evolutionary highly conserved protein from *Mus musculus* was identified, showing 90% identity to the protein variant in *Xenopus tropicalis* and 29% identity to the variant in *Plethodon chlorobryonis*, hypothesizing homology to the respective protein variant in *P. shermani*. And thirdly, human “peptidyl-prolyl cis-trans isomerase A-like 4G” was identified, showing 98% identity to the protein variant in *Xenopus laevis* and 29% identity to the variant in *Ambystoma tigrinum*, also hypothesizing homology to the respective protein variant in *P. shermani*.

## 3.2 MALDI – IM-MS Imaging

### 3.2.1 Evaluation of Ion Mobility Parameter

As described in chapter 1.7.1.1, the parameters of the Triwave device have to be adapted for a selected  $m/z$  range, in order to separate ions according to their mobility while maintaining the transfer efficiency into the TOF mass analyzer. Additionally, those parameters have to guarantee that all ions leave the Triwave device within the drift time window of 200 bins. If this is not fulfilled, ion-carry-over occurs and the ions leave the Triwave too late, presenting shorter drift times for the respective ions, since they are detected with the next ion package. There are three main parameters to influence transfer efficiency and ion mobility separation. The first parameter is the nitrogen gas flow and therefore the pressure in the IMS TWIG ("IMS Gas Flow" [ml/min]). The second parameter is the velocity with which the electric potential, the so called "wave" is moving through the IMS TWIG ("IMS Wave Velocity" [m/s]). And the third parameter is the height of the electric potential ("IMS Wave Height" [V]). To evaluate the influence of these parameters, an experimental grid was established representing stepwise changes of parameters. The borders of the evaluation grid were defined by a first, manual scouting-approach for somehow good results. The definition of a good result will be explained later on. The used values of the three parameters are illustrated in a 3-dimensional way in Figure 40, whereas each spot represents the used settings for an IM-MS experiment. The selected  $m/z$  range was always set to 500–3 760 and mass spectra were recorded for approx. 60 sec. All experiments were carried out for 500 fmol TOF<sup>2</sup> peptide standard and for 1 nmol lipid standard prepared according to the sandwich-method applying the layers in the following order: matrix – CBO – CLP – PC – matrix. For more information on sample preparation methods see chapter 2.11.1.

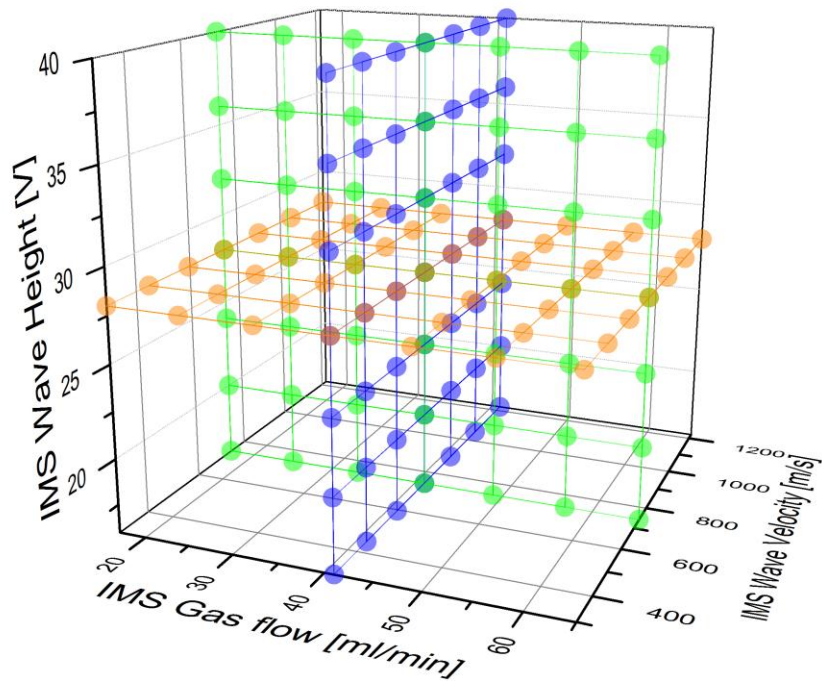


Figure 40: 3D visualization of the used parameters

The correlation between the drift times of detected ions in an IM-MS experiment and their corresponding  $m/z$  values is visualized in a two-dimensionally way using the software DriftScope by Waters. One axis represents the  $m/z$  values, the other axis represents the drift time values in bins. The intensity of detected ions is expressed in a hot-metal color scale whereas the intensity increases from black (0% intensity) to white (100% intensity). To evaluate the quality of the graphs in a standardized way, a scheme with a classification of four colors was established. The quality of a DriftScope-graph can be seen as good if all ions are detected within the drift time of 200 bins, respectively the green area. Graphs with ions detected in areas marked in red represent unacceptable results, whereas ions detected in orange or yellow areas represent graphs with improving quality. The created scheme (a) as well as an exemplary DriftScope-graph with good quality (b) are shown in Figure 41. In Figure 41/b it is observed that ions at approx.  $m/z$  1 800 and a drift time of below 50 bins are present in the orange marked area. However, since they represent doubly charged ions, they were not considered for parameter evaluation.

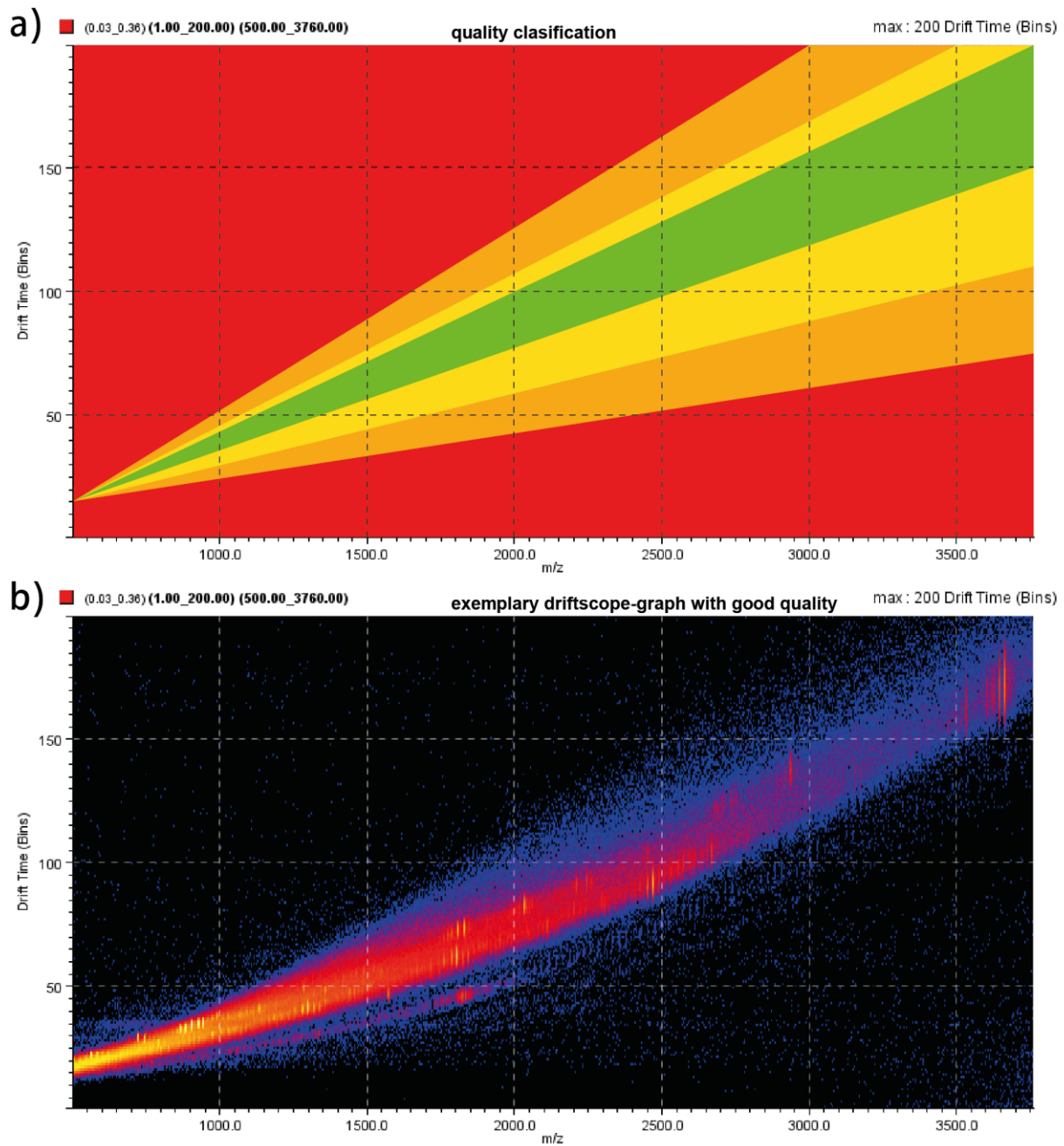


Figure 41: a) Quality classification of DriftScope-graphs; b) exemplary DriftScope-graph with good quality where ions are detected in the green area

A visualized summary of the results from the evaluation grid is shown in Figure 42. Each box thereby represents the quality of an individual DriftScope-graph according to the previously described color coding (Figure 41/a). Furthermore it shows the extracted drift time for a chosen analyte. For experiments with the peptide standard the drift time of N-acetyl-renin with  $[M+H]^+_{\text{mono}} 1\ 800.94$  and for experiments with the lipid standard the drift time of PC-dimer with  $[2M+H]^+_{\text{mono}} 1\ 804.51$  was extracted and therefore studied in detail.

Regarding a good quality for the DriftScope-graphs, it can be said that there is a correlation between the three parameters. If the IMS Wave Velocity is increased the height of the wave has to increase as well, but the IMS Gas Flow has to decrease. This is in accordance to the characteristics of the TriWave device as described in chapter 1.7.1.1: for a faster travelling wave, the wave height has to increase in order to maintain efficient ion transfer and to avoid ion carry-over and in parallel the resistance for the analyte ions has to be reduced by decreasing the IMS Gas Flow (lesser nitrogen molecules are present in the device). The evaluation of the parameters also reveals that above a certain IMS Wave Velocity no good result can be obtained due to the fact that the IMS Gas Flow cannot be reduced much further and the IMS Wave Height cannot be increased further due to instrumental limitations.

If the IMS Wave Height is considered with respect to a constant IMS Wave Velocity, it can be stated that an increase in the wave height leads to a necessary increase of the IMS Gas Flow to maintain adequate separation. But it also has to be said, that an increase of the gas flow results in a loss of transmission efficiency and the possibility of ion fragmentation due to collision events. Hereby instrumental limitations are again the maximal possible IMS Wave Height and *vice versa* there are also limitations according to a minimal gas flow and minimal wave height.

For the quality of DriftScope-graphs, comparable trends were observed for peptide (500 fmol TOF<sup>2</sup>) and lipid standards (1 nmol CBO-CLP-PC). However it was more difficult to distinguish the quality of graphs from lipid standards, since the highest m/z value was detected for the PC-dimer at  $[2M+H]^+_{\text{mono}} 1\ 804.51$  (compared to  $[M+H]^+_{\text{mono}} 3\ 657.97$  of ACTH fragment 7-38 for the peptide standard).

Regarding the extracted drift times of selected ions it further can be said, that a slow travelling wave and therefore a low wave height but high gas flow results in longer ion drift times for all analytes. Further do lipids usually have a more linear and outstretched structure in contrast to the mostly globular structures of peptides, resulting in lower ion mobility and therefore longer

drift times for lipids. This observation allows us to separate ions according to their species and to draw conclusions for future experiments with unknown analyte ions.

a) 500fmol TOF <sup>2</sup>										b) 1nmol CBO-CLP-PC									
extracted drift times for N-acetyl-renin [M+H] <sup>+</sup> mono 1800.97										extracted drift times for PC-dimer [2M+H] <sup>+</sup> mono 1804.51									
IMS Gas flow [ml/min]	IMS Wave Velocity [m/s]									IMS Gas flow [ml/min]	IMS Wave Velocity [m/s]								
41										41									
IMS Wave Height [V]		16	20	24	28	32	36	40		16	20	24	28	32	36	40			
299	82.4695	54.8724	39.1678	29.1528	23.1993	18.6673	15.3121		299	99.4964	65.9414	47.7751	36.1574	28.1585	23.3508	19.1234			
455	124.594	82.8949	58.1436	44.1621	35.1836	29.3	25.2681		455	151.284	99.6996	71.7725	54.9131	43.9845	35.332	30.2194			
595	172.218	113.678	80.8879	61.1469	48.1429	39.1978	33.282		595	12.1378	133.126	97.5629	73.5548	58.1163	48.121	40.8525			
741	21.1665	146.509	104.687	78.1057	62.1462	50.1112	42.2684		741	76.282	175.416	124.798	93.2464	74.776	60.261	51.1154			
896	97.1147	188.29	133.316	99.5602	77.1125	63.1145	52.1802		896	151.312	23.332	158.706	118.134	92.1661	75.928	63.1007			
1053	166.754	42.176	169.44	124.685	97.7562	78.1298	65.186		1053	44.5	83.181	197.77	148.244	113.261	92.1235	76.202			
1225	92.512	105.853	12.244	158.345	122.492	97.1422	81.1131		1225	29.131	197.49	45.649	186.434	143.832	115.301	94.2116			

IMS Wave Height [V]	IMS Wave Velocity [m/s]									IMS Wave Height [V]	IMS Wave Velocity [m/s]								
28										28									
IMS Gas flow [ml/min]		17	25	33	41	49	57	65		17	25	33	41	49	57	65			
299	13.9767	15.1221	21.1621	29.1528	37.6247	46.3272	56.99		299	15.1599	18.3738	27.1648	36.1574	46.9081	57.3378	70.249			
445	15.9041	24.9606	33.3249	44.1621	56.4094	70.2765	85.902		445	20.7502	30.1624	41.2029	54.9131	69.3388	85.2441	105.32			
595	22.1583	34.1387	46.1576	61.1469	77.435	95.4113	115.163		595	27.6366	41.1571	56.1746	73.5548	93.4878	114.837	141.188			
741	30.7332	45.3028	60.1736	78.1057	98.3796	121.236	150.794		741	37.2082	53.1694	72.1003	93.2464	119.324	147.302	183.264			
896	42.1027	58.2609	77.1164	99.5602	125.153	152.124	188.696		896	49.1181	69.7523	92.828	118.134	150.261	185.571	231.51			
1053	57.8348	77.8186	100.687	124.685	153.252	188.615	232.316		1053	65.7348	88.1346	115.324	148.244	182.224	228.489	285.73			
1225	80.6434	103.488	126.185	158.345	199.128	249.907	311.776		1225	89.2561	115.602	146.144	186.434	231.382	285.915	351.42			

IMS Wave Velocity [m/s]	IMS Gas flow [ml/min]									IMS Wave Velocity [m/s]	IMS Gas flow [ml/min]								
741										741									
IMS Wave Height [V]		16	20	24	28	32	36	40		16	20	24	28	32	36	40			
17	85.1803	56.6872	40.2378	30.7332	23.7357	19.1862	17.1964		17	102.108	66.4029	48.1142	37.2082	31.488	25.3081	22.3618			
25	124.349	82.1044	58.1503	45.3028	35.1982	29.2271	25.1603		25	146.104	96.3678	69.1895	53.1694	43.5226	35.1849	30.9132			
33	170.266	112.425	80.5843	60.1736	47.12	39.2387	33.2303		33	195.293	133.293	95.234	72.1003	57.5226	47.1139	40.1167			
41	21.1665	146.509	104.687	78.1057	62.1462	50.1112	42.2684		41	76.282	175.416	124.798	93.2464	74.776	60.261	51.1154			
49	97.708	184.143	132.263	98.3796	77.5227	63.5248	52.6008		49	24.119	29.517	157.128	119.324	93.1017	75.2757	63.461			
57	200.151	31.648	163.907	121.236	93.2671	77.2004	63.3294		57	0	99.101	198.512	147.302	111.14	91.632	77.1652			
65	0	192.59	199.237	130.794	115.867	92.1174	75.1994		65	0	0	47.49	183.264	136.14	111.84	92.193			

Figure 42: Summarized results for all experiments presented in a grid-like structure, color code according to Figure 41; a) peptide standards with extracted drift times; b) lipid standards with extracted drift times

Here it also has to be stated that the drift time was extracted by integrating the monoisotopic peak, resulting in a precise drift time. But like it is the case for mass spectra, where the resolution is defined by the full peak width at half maximum (see chapter 1.4), we also have a spread of detected drift time for one ion species as it is shown in Figure 43. This also illustrates, that even if a longer drift time is gained by a slow wave and a low wave height, a better drift time resolution is gained by a faster wave with a corresponding faster wave height.

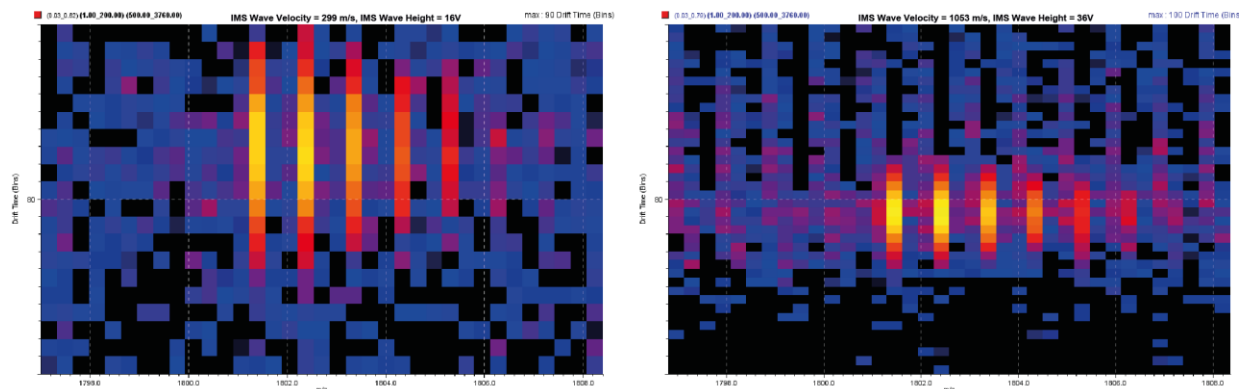


Figure 43: Drift time resolution for N-acetyl-renin; a) low wave velocity and low wave height resulting in a longer drift time; b) high wave velocity and high wave height resulting in a shorter drift time but better resolution

Triwave parameters for efficient ion transmission and ion mobility separation are also depending on the selected m/z range. To estimate which parameters could result in a good DriftScope-graph for a m/z range of 500-2 000, a new quality classification scheme (see Figure 44) was proposed to reevaluate the data from the previous experiments (peptide standard, m/z range of 500-3 760).

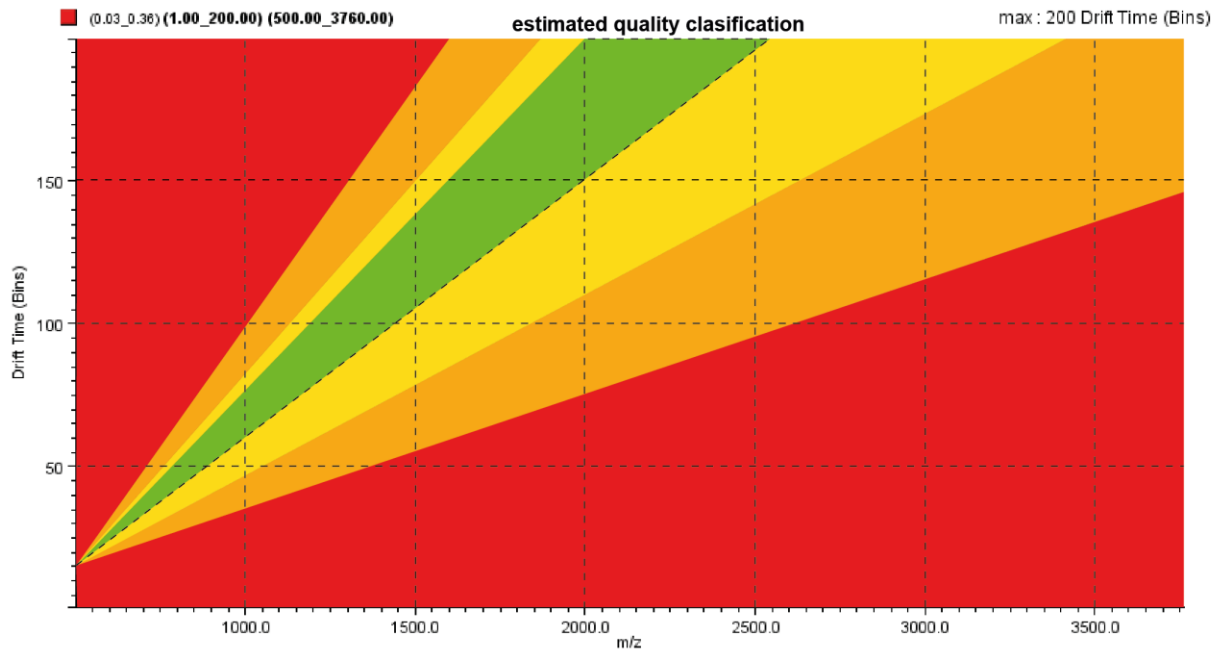


Figure 44: Classification scheme to estimate parameters for a good quality of DriftScope-graphs for a m/z range of 500-2 000

A visualized summary of the estimated quality of DriftScope-graphs with a m/z range of 500-2 000 for peptide standards is shown in Figure 45/a, whereas Figure 45/b shows again the quality classifications for the corresponding m/z range 500-3 760. For m/z 500-2 000, experiments were performed with selected parameters (in total 7 experiments) which should result in DriftScope-graphs of good quality. In this way the following observations were proven to be correct.

The same trends regarding the three parameters were observed for the smaller m/z range: higher IMS Wave Velocity needs higher IMS Wave Height and lower IMS Gas Flow for good ion transmission efficiency. Furthermore a higher wave requires a higher gas flow in respect to a constant wave velocity to maintain good ion mobility separation. However a smaller m/z range requires higher IMS Wave Velocities or IMS Gas Flows in respect to the same IMS Wave Height for the larger m/z range. Therefore the evaluation grid does not cover the parameters believed to result in DriftScope-graphs with good quality. However this is only

correct if the cut-off is applied at the upper end of the  $m/z$  range. Also similar to the previous described observations, instrumental limitations are given according to minimal possible wave heights and gas flows. *Vice versa*, IMS Wave Velocities can only be increased to a certain point. Since the  $m/z$  range was limited to smaller  $m/z$  values and therefore towards ions with higher mobility it can be said, that their separation is improved by a faster wave and higher gas flow in contrast to ions with lower mobility. Again this is in accordance to the characteristics of ion mobility separation by the TriWave device as described in chapter 1.7.1.1.

The values in Figure 45 further represent drift time differences of ions with similar  $m/z$  values. Figure 45/b represents the drift time differences between the PC-dimer  $[M+H]^+_{\text{mono}} 1\ 804.51$  (lipid) and N-acetyl-renin  $[M+H]^+_{\text{mono}} 1\ 800.97$  (peptide) and Figure 45/a represents drift time differences calculated for castor bean oil  $[M+H]^+_{\text{mono}} 955.8$  (lipid) and the mean drift time of the peptides bradykinin 1-7  $[M+H]^+_{\text{mono}} 757.4$  and angiotensin 2  $[M+H]^+_{\text{mono}} 1046.5$  since no peptide with similar  $m/z$  value was present. The observations for the drift time differences between lipids and peptides are the same for smaller and larger  $m/z$  values. The drift time differences increase for slower waves with decreased wave heights and higher gas flows. But as mentioned earlier and observed in Figure 43, drift time resolution also decreased with these parameters. Depending on the sample type and on the analytical problem, a priority towards larger separation or better resolution has to be chosen. For standard applications it has proven to be a good choice to set moderate parameters trending towards slightly faster and higher waves since the advantage of increased resolution predominates larger drift time differences. But it always has to be kept in mind that transmission efficiency has to be maintained and therefore IMS Wave Velocities should be kept below the possible maximum.

a) estimated quality for a m/z range of 500-2000 drift time differences between (bradykinin 1-7 + angiotensin 2)/2 and CBO									b) quality for a m/z range of 500-3760 drift time differences between N-acetyl-renin and PC-dimer									
IMS Gas Flow [ml/min]	IMS Wave Velocity [m/s]								IMS Gas Flow [ml/min]	IMS Wave Velocity [m/s]								
41									41									
IMS Wave Height [V]		16	20	24	28	32	36	40	IMS Wave Height [V]		16	20	24	28	32	36	40	
	299	5.775	5.581	3.176	0.097	0.271	-0.385	0.801		299	17.027	11.069	8.607	7.005	4.959	4.684	3.811	
	455	9.844	7.445	5.507	5.099	4.393	2.826	2.323		455	26.691	16.805	13.629	10.751	8.801	6.032	4.951	
	595	14.265	9.625	7.318	5.447	4.533	2.897	2.457		595	-160.080	19.447	16.675	12.408	9.973	8.923	7.571	
	741	18.103	12.025	8.079	5.984	4.982	4.752	3.942		741	55.116	28.907	20.111	15.141	12.630	10.150	8.847	
	896	22.449	14.558	9.891	8.027	6.947	5.556	5.176		896	54.197	-164.958	25.390	18.574	15.054	12.814	10.921	
	1053	32.905	19.596	12.984	9.041	7.965	5.840	5.382		1053	-122.254	41.005	28.330	23.559	15.505	13.994	11.016	
	1225	-63.957	21.537	14.548	12.526	10.052	7.429	7.185		1225	-63.381	91.637	33.405	28.089	21.340	18.158	13.099	
IMS Wave Height [V]	IMS Wave Velocity [m/s]								IMS Wave Height [V]	IMS Wave Velocity [m/s]								
28									28									
IMS Gas Flow [ml/min]		17	25	33	41	49	57	65	IMS Gas Flow [ml/min]		17	25	33	41	49	57	65	
	299	1.367	-0.197	-0.023	0.097	4.099	5.337	5.716		299	1.183	3.252	6.003	7.005	9.283	11.011	13.259	
	445	1.842	0.953	6.913	5.099	5.677	6.552	7.117		445	4.846	5.202	7.878	10.751	12.929	14.968	19.418	
	595	2.830	4.147	3.478	5.447	7.001	8.772	8.976		595	5.478	7.018	10.017	12.408	16.053	19.426	26.025	
	741	1.522	3.780	5.096	5.984	8.763	10.160	12.473		741	6.475	7.867	11.927	15.141	20.945	26.066	32.470	
	896	3.096	3.809	6.439	8.027	9.555	11.966	1.605		896	7.015	11.491	15.712	18.574	25.109	33.447	-149.186	
	1053	3.011	5.465	7.662	9.041	12.399	16.000	19.209		1053	7.900	10.316	14.638	23.559	28.972	-160.126	83.414	
	1225	4.147	5.155	7.862	12.526	13.700	2.297	22.670		1225	8.613	12.114	19.959	28.089	-167.746	52.043	18.244	
IMS Wave Velocity [m/s]	IMS Gas Flow [ml/min]								IMS Wave Velocity [m/s]	IMS Gas Flow [ml/min]								
741									741									
IMS Wave Height [V]		16	20	24	28	32	36	40	IMS Wave Height [V]		16	20	24	28	32	36	40	
	17	6.315	3.849	2.913	1.522	3.049	3.778	6.616		17	16.928	9.716	7.876	6.475	7.752	6.122	5.165	
	25	9.508	6.061	8.687	3.780	3.184	2.730	2.890		25	21.755	14.263	11.039	7.867	8.324	5.958	5.753	
	33	15.184	8.790	6.509	5.096	4.300	3.461	2.901		33	25.027	20.868	14.650	11.927	10.403	7.875	6.886	
	41	18.103	12.025	8.079	5.984	4.982	4.752	3.942		41	55.116	28.907	20.111	15.141	12.630	10.150	8.847	
	49	24.119	14.942	11.257	8.763	6.530	5.005	4.651		49	-73.589	-154.626	24.865	20.945	15.579	11.751	10.860	
	57	33.155	21.301	17.901	10.160	8.704	6.612	5.137		57	-200.151	67.453	34.605	26.066	17.873	14.432	13.836	
	65	-66.248	22.931	16.979	12.473	9.620	8.230	6.608		65	0.000	-102.590	-151.747	32.470	20.273	19.723	16.994	

Figure 45: Comparison of DriftScope-graph qualities for the m/z range of 500-3 760 (b) and an estimated quality of the m/z range 500-2 000 (a); a) differences between the drift time of the lipid CBO  $[M+Na]^+_{mono}$  955.8 and the mean drift time of the peptides bradykinin 1-7  $[M+H]^+_{mono}$  757.4 and angiotensin 2  $[M+H]^+_{mono}$  1 046.5; b) drift time differences between the peptide N-acetyl-renin  $[M+H]^+_{mono}$  1 800.97 and the lipid PC-dimer  $[2M+H]^+_{mono}$  1 804.51

To test for a constant drift time for a specific ion, ten consecutive experiments for the same sample of 1 nmol PC prepared with the mixed-solvent method, were performed with an IMS Gas Flow of 48.5 ml/min, an IMS Wave Velocity of 1225 m/s and an IMS Wave Height of 40 V. The resulting drift times were extracted for the FWHM of the monoisotopic peak  $[M+H]^+_{mono}$  902.75 and the complete isotopic pattern of m/z 902-904 as well as for the FWHM of the monoisotopic peak of the PC-dimer  $[2M+H]^+_{mono}$  1 804.51 and the complete isotopic pattern of m/z 1 804-1 807. The results are displayed in Table 12. A variation in the extracted drift times can be observed, whereas the variation for the PC-dimer is higher than for the monomer. It also can be observed that the variation is reduced by extracting the drift time over the complete isotopic pattern, probably due to an already kind of averaged drift time.

Table 12: Extracted drift times of PC and PC-dimer for 10 consecutive experiments with a m/z range of 500-3 760, an IMS Gas Flow of 48.5ml/min, an IMS Wave Velocity of 1 225 m/s an IMS Wave Height of 40V and an helium gas flow of 180ml/min

PC	m/z 902-904	m/z 902.8	PC-dimer	m/z 1804-1807	m/z 1804.5
	51.565091	51.241165		113.8166	113.2438
	51.626791	51.320465		112.8125	113.2567
	52.787198	52.333945		113.1046	113.3015
	52.429362	52.225242		114.6028	113.2052
	52.363737	52.132937		113.5657	113.1745
	52.330169	52.145319		112.4063	112.1335
	52.443103	52.182788		112.5659	112.1961
	52.235295	52.747280		113.3238	112.8920
	52.163826	52.121647		114.2814	114.9750
	52.229913	52.128263		113.3594	115.1349
<b>Mean</b>	<b>52.217448</b>	<b>52.057905</b>		<b>113.383896</b>	<b>113.351320</b>
<b>STD</b>	<b>0.351</b>	<b>0.428</b>		<b>0.674</b>	<b>0.945</b>

Due to abnormal high helium consumption during the conducted experiment period compared to previous experiences, a leakage of the helium gas line supplying the instrument was suspected. This was expected to explain the rather high drift time variations due to fluctuations of the resulting helium pressure as well as possible oxygen/air contaminations of the gas flow. After installing a direct gas supply to the instrument and a new pressure regulation valve for fine regulation of the aspired pressure range directly at the gas bottle, the experiments were repeated.

Before and after the installation, an experiment for 100 fmol of TOF<sup>2</sup> standard was conducted for a m/z range of 500-2 000 with an IMS Wave Velocity of 1 225 m/s, an IMS Wave Height of 36 V and an IMS Gas Flow of 38 ml/min. Both resulting DriftScope-graphs are shown in Figure 46 and the resulting effect from a new gas line and pressure valve is quite obvious. In consideration of the structure of the Triwave device (see Figure 20) helium gas also enters the IMS TWIG and after the installation of the new gas line and pressure valve, there seemed to be a higher pressure inside the IMS TWIG resulting in a higher retention of the analyte ions and therefore unfavorable ion-carry-over (Figure 46/b).

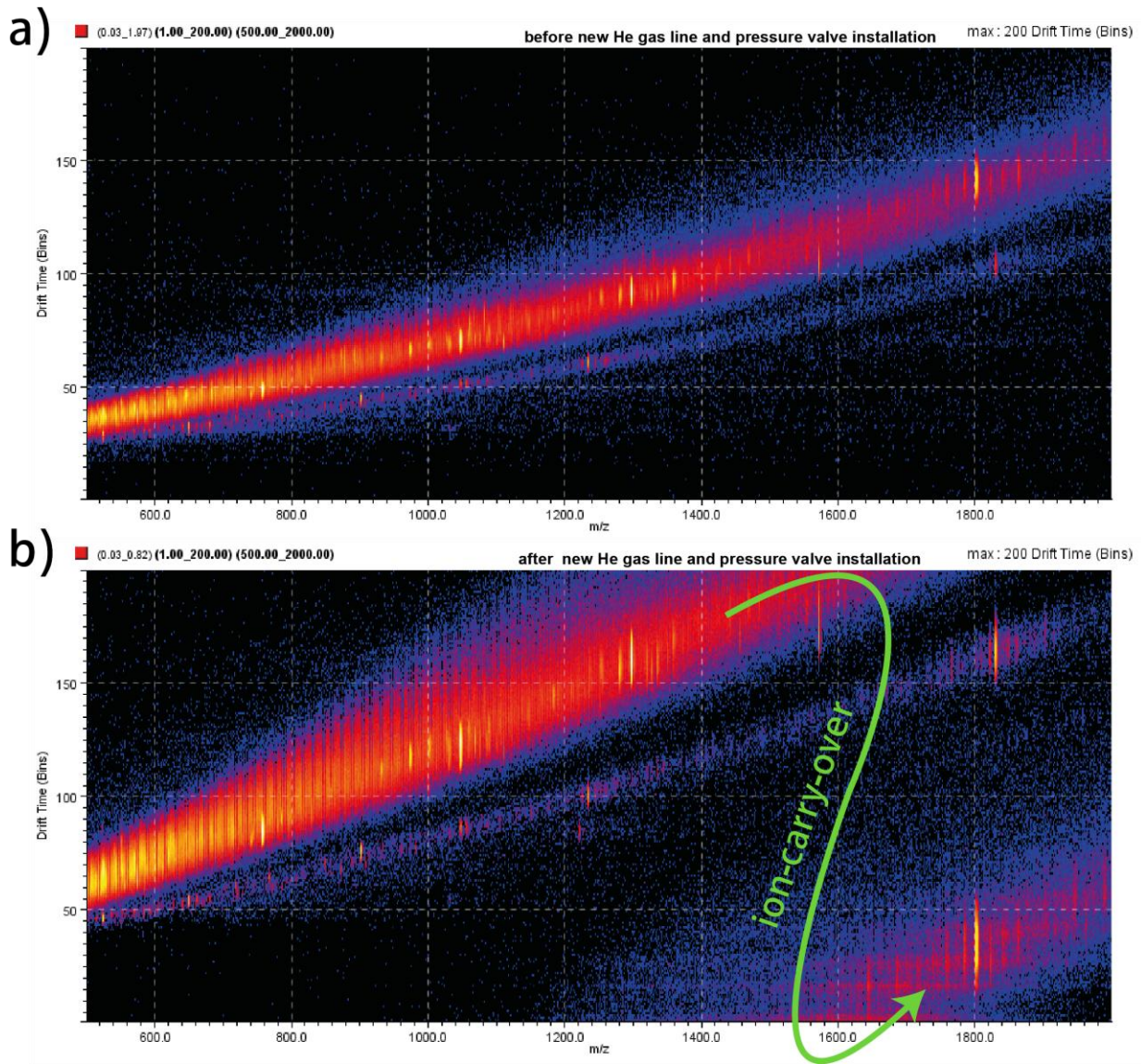


Figure 46: DriftScope-graphs of 100 fmol TOF<sup>2</sup> conducted with the same settings before (a) and after (b) installation of a new helium gas line and pressure valve

Since the helium inlet pressure into the instrument could now be adjusted more correctly to 0.5 mbar, the helium gas flow in the helium cell had to be reduced from 180 ml/min to 20 ml/min in order to achieve similar results using the same ion mobility settings as applied before the installation. The helium gas flow was then tested for selected parameters from the evaluation grid, resulting in the additional adaption of the IMS Gas Flow (reduction) but overall improved ion mobility separation (see Figure 47).

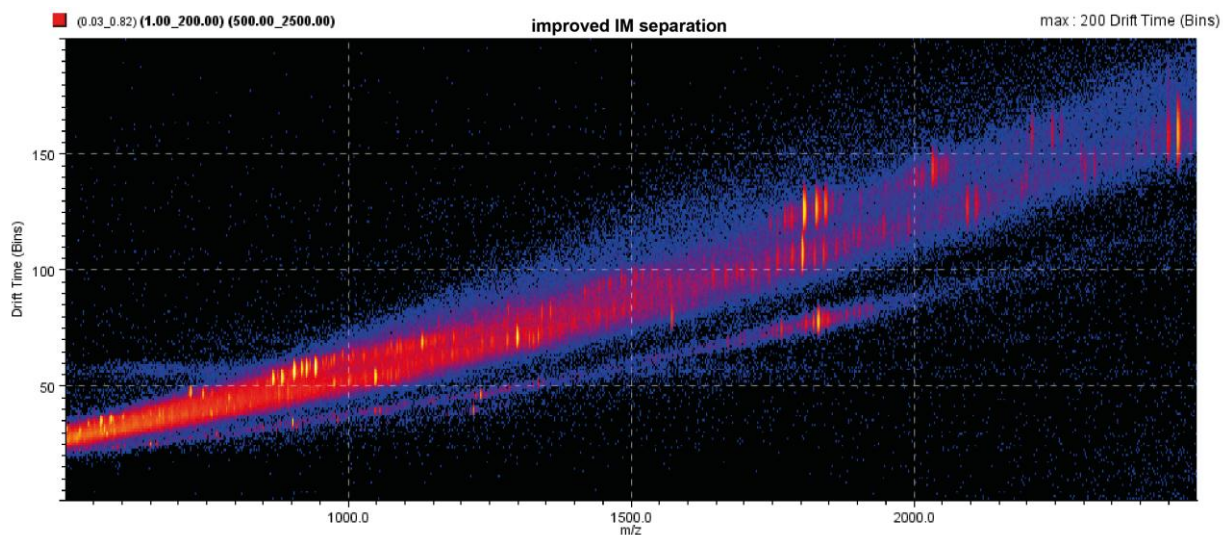


Figure 47: Improved IM separation after new He-gas line and pressure valve instalation; IMS Wave Velocity 1 225 m/s, IMS Wave Height 35 V, IMS Gas Flow 36 ml/min, He-gas flow 20 ml/min

The test for constant drift times was then repeated for ten consecutive experiments for the same sample of 1 nmol of PC, performed with an IMS Wave Velocity of 1 225 m/s and an IMS Wave Height of 40 V but now an IMS Gas Flow of 37 ml/min and a helium gas flow of 20 ml/min instead of 180 ml/min. The resulting drift times again were extracted for the FWHM of the monoisotopic peak  $[M+H]^+_{\text{mono}}$  902.75 and the complete isotopic pattern of  $m/z$  902-904 as well as for the FWHM of the monoisotopic peak of the PC-dimer  $[2M+H]^+_{\text{mono}}$  1 804.51 and the complete isotopic pattern of  $m/z$  1 804-1 807, the results are shown in Table 13. A variability of the extracted drift times was still observed but the variability was obviously reduced (compare Table 12). The drift time variability for the monoisotopic peak and the isotopic pattern, as well as for smaller and larger  $m/z$  values is now also in a comparable range. Based on personal communication to instrument engineers it was pointed out that the instrument inherent Pirani gauges have an accuracy of  $\pm 15\%$ . This further explains slight variations of drift times due to possible fluctuations in the gas flows.

This observation leads to the consequence, that if ion mobility separation is used to determine drift times in order to identify isobaric species like isomers or to distinguish folding states of proteins, always analyte mixtures have to be analyzed to maintain the possibility of internal calibration of drift time, especially if analytes are investigated exhibiting only small drift time differences.

Table 13: Extracted drift times of PC and PC-dimer for 10 consecutive experiments with a m/z range of 500-3 760, an IMS Gas Flow of 37ml/min, an IMS Wave Velocity of 1 225 m/s an IMS Wave Height of 40V and an helium gas flow of 20ml/min

PC	m/z 902-904	m/z 902.8	PC-dimer	m/z 1804-1807	m/z 1804.5
	47.610997	47.287318		102.14583	102.3361
	47.646790	47.262688		102.29773	102.7496
	47.596197	47.305054		102.21894	102.5823
	47.182415	47.775153		102.87007	102.2201
	47.219788	47.869920		102.15745	102.4302
	47.980593	47.434378		102.39076	102.9271
	47.139688	47.605305		102.93860	102.2319
	47.193058	47.800735		102.11586	102.3004
	47.252014	47.102659		102.17326	102.4776
	47.879261	47.397342		102.42346	102.1063
<b>Mean</b>	<b>47.470080</b>	<b>47.484055</b>		<b>102.37320</b>	<b>102.4361</b>
<b>STD</b>	<b>0.296</b>	<b>0.250</b>		<b>0.283</b>	<b>0.242</b>

### 3.2.2 Ion Fragmentation coupled with IM Separation

As it was described in chapter 1.7.1.2, the instrumental setup allows performing different types of CID experiments in combination with ion mobility separation. After the Triwave parameters were evaluated and the settings optimized, three different fragmentation types were tested, CID prior to IMS, CID after IMS and CID after IMS without precursor ion selection. The fourth type, ion fragmentation before and after ion mobility separation ( $MS^3$ -type) was not investigated.

#### CID prior to IMS

CID fragmentation of selected precursor ions prior to IM separation helps to get information of the 3-dimensional structure of resulting fragment ions and therefore information about the chemical structure of the precursor ion can be deduced. For a standard of 1 nmol CLP, 1 nmol CBO and 666 pmol PC prepared by sandwich-method, a precursor ion window of  $m/z$  1 516  $\pm$  4 and a collision energy in the Trap TWIG of 75 V was chosen. The IMS Gas Flow was set to 48.5 ml/min, the IMS Wave Velocity to 1 225 m/s and the IMS Wave Height to 40 V. The resulting DriftScope-graph is shown in Figure 48. It can be observed that some of the fragment ions have longer drift times than others, allowing for example to get hints about the head group of lipids which usually has a more globular structure and therefore shorter drift time.

Further at approx.  $m/z$  600 and  $m/z$  620, ions with similar  $m/z$  but different drift times can be observed, proving that isobaric fragment ions or fragment ions with similar  $m/z$  values can clearly be distinguished.

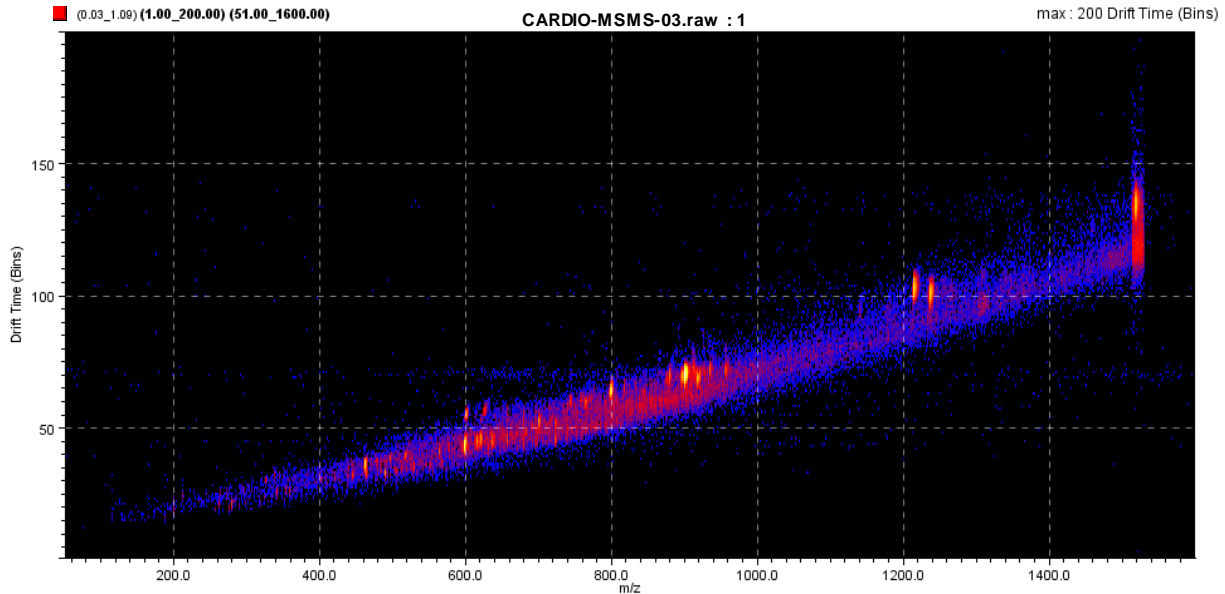


Figure 48: DriftScope-graph for CID prior to IMS and a  $m/z$  precursor ion window of  $1\ 516 \pm 4$

The mass spectrum of the precursor- and fragment-ions is shown in Figure 49 which identifies the precursor  $m/z$  1 515.9 as cardiolipin ion  $[M+3Na-2H]^+_{mono}$ . Hereby the second signal of ions at approx.  $m/z$  600 and  $m/z$  620 could not be assigned since they do not belong to other theoretical fragment pattern of cardiolipin. One explanation can be different 3D structures for the specific fragments or yet unknown fragments.

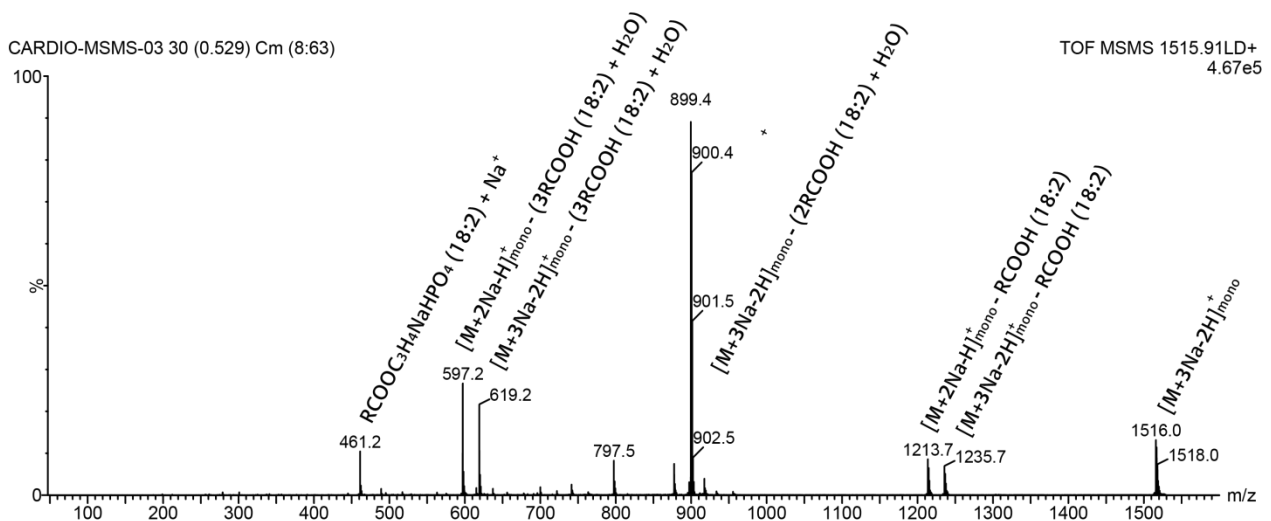


Figure 49: Mass spectrum for CID prior to IMS and a  $m/z$  precursor ion window of  $1516 \pm 4$

## CID after IMS

CID fragmentation of selected precursor ions after IM separation allows to distinguish fragment ions belonging to isobaric species since those fragment ions are detected with the same drift times as their corresponding precursor ions. For a standard of 1 nmol PC and 500 fmol TOF<sup>2</sup> prepared by sandwich-method, a precursor ion window of  $m/z$   $1801 \pm 5$  and a collision energy in the Transfer TWIG of 100 V was chosen. The IMS Gas Flow was set to 48.5 ml/min, the IMS Wave Velocity to 1 225 m/s and the IMS Wave Height to 40 V. The resulting DriftScope-graph is shown in Figure 50. It can be observed that fragment ions in fact have the same drift time as their corresponding precursor ion whereas ions for three different drift times are detected, approx. 110 bins, approx. 95 bins and approx. 60 bins.

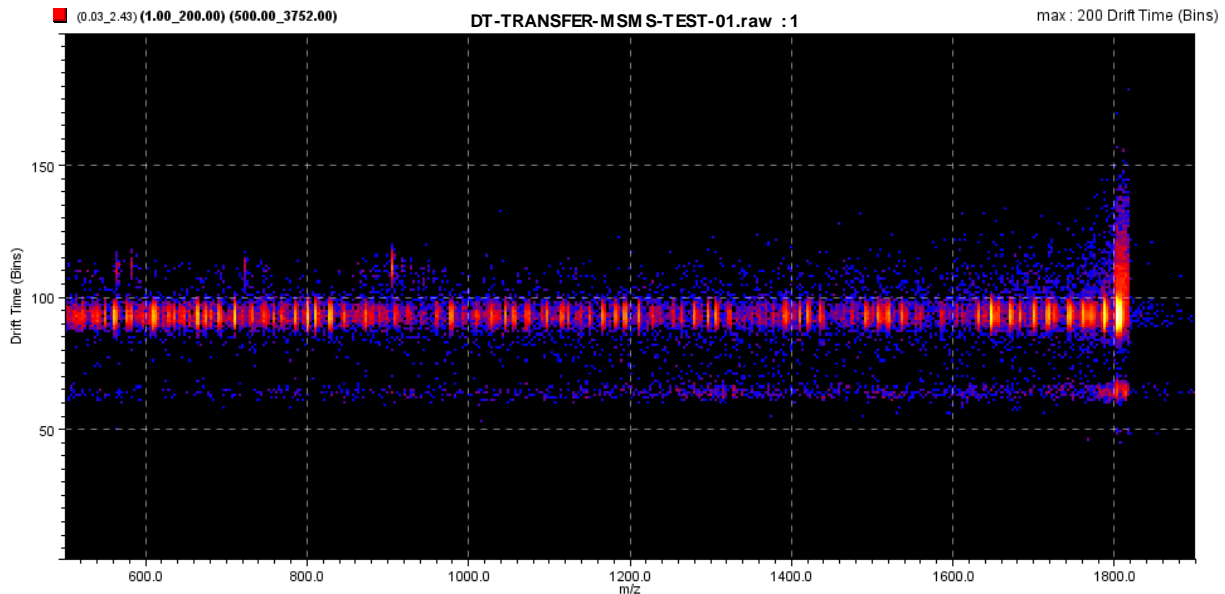


Figure 50: DriftScope-graph for CID after IMS and a  $m/z$  precursor ion window of  $1801 \pm 5$

Within the DriftScope-graph, regions can be selected and mass spectra with the corresponding ions are generated. By generating mass spectra for ions with only specific drift times this not only allows identifying isobaric analytes, but compared to the overall mass spectrum, this also increases positive protein identification by Mascot search. The ions with a drift time of approx. 60 bins belong to a doubly charged precursor ion and were not further investigated, whereas the extracted mass spectrum for selected ions with a drift time of approx. 95 bins is shown in Figure 51. It shows fragment ions belonging to the precursor ion  $m/z$  1 800.9 and by generating a mass list for peaks with a  $S/N \geq 3$ , this precursor ion can be identified as angiotensinogen fragment 1-14 by Mascot search with a significant Mascot score of 49 to 13 ( $p < 0.05$ , see Figure 52), which is the same as N-acetyl-renin.

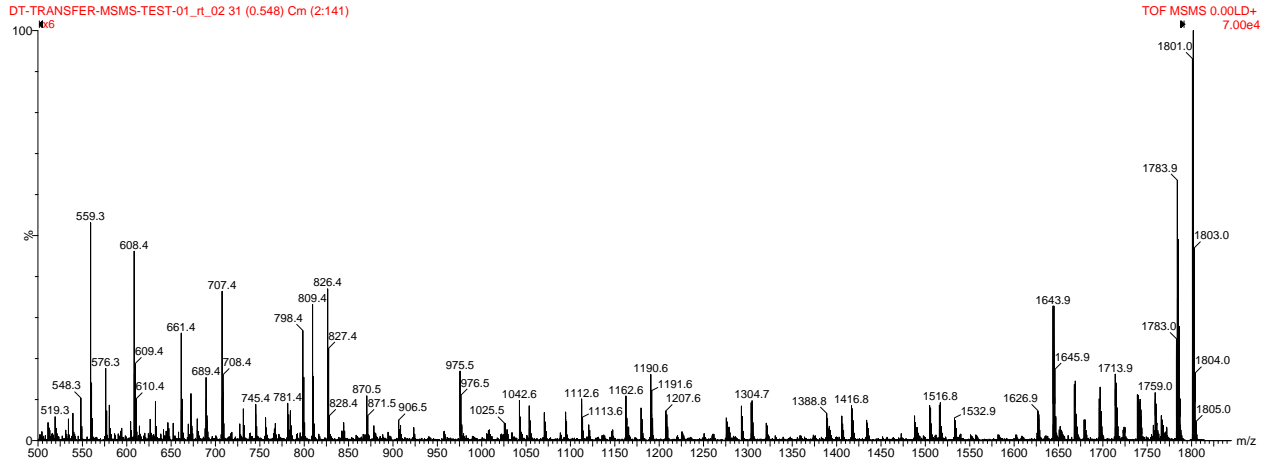


Figure 51: Mass spectrum for selected ions with a drift time of approx. 95bins

### MATRIX SCIENCE Mas cot Search Results

User : Max  
 Email : max.hosok@twien.acat  
 Search title : PT-TET-01-RMS-03rt\_01  
 Database : NCBI 2013830 (3252081 sequences; 111643558 residues)  
 Taxonomy : Mammalia (mammals) (181872 sequences)  
 Timestamp : 2 Sep2013 13:45:17 GMT  
 Protein hits : [gi|113879](#) RecName: Full=Angiotensinogen; AltName: Full=Serpina8; Contain: RecName: Full=Angiotensin; AltName: Full=Angiotensin-10  
 AltName FullAngiotensin I; ShortAng I; Contain: RecName: Full=Angiotensin2; AltName: Full=Angiotensin 1-8; AltName F

#### Mascot Score Histogram

Ions score is  $-10 \log(P)$ , where P is the probability that the observed match is a random event.  
 Individual ions scores > 13 indicate identity or extensive homology ( $p < 0.05$ ).  
 Protein scores are derived from ions scores as a non-probabilistic basis for ranking protein hits.

#### Peptide Summary Report

1. [gi|11389](#) Mass: 1800 Score: 49 Matches: 1(1) Sequences: 1(1)  
 RecName: Full=Angiotensinogen; AltName: Full=Serpina8; Contain: RecName: Full=Angiotensin-1; AltName: Full=Angiotensin 1-10  
 AltName: Full=Angiotensin I; Short=Ang I Contain: RecName: Full=Angiotensin-2; AltName: Full=Angiotensin 1-8; AltName: F

Check  include this hit in error tolerant search

Query	Observed	Mr (exp)	Mr (calc)	Delta	Miss	Score	Expect	Rank	Unique	Peptide
<a href="#">1</a>	900.9000	1799.784	179.9359	-0.154	0	49	1.6e-05	1	U	-DRVYIHFLLWS-

Figure 52: Mascot search result for selected fragment ions with a drift time of approx. 95bins

The mass spectrum for selected ions with a drift time of approx. 110 bins is shown in Figure 53 showing one main fragment ion with an m/z value of 902.8 which is the  $[M+H]^+_{\text{mono}}$  from PC resulting from the PC-dimer ion  $[2M+H]^+_{\text{mono}}$  1 804.5.

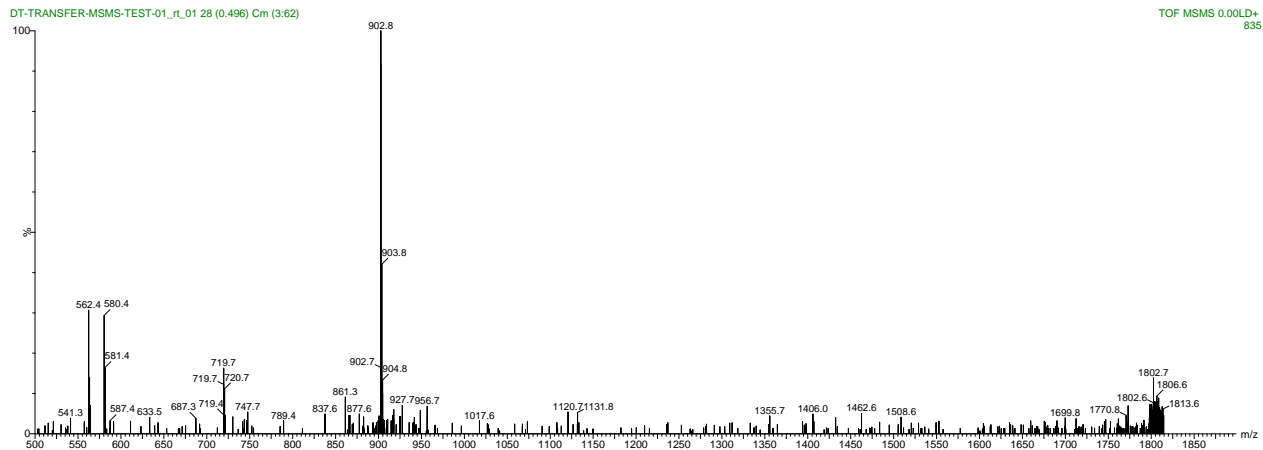


Figure 53: Mass spectrum for selected ions with a drift time of approx. 110bins

This experiment proved that CID ion fragmentation after ion mobility separation allows to identify isobaric ions or ions with similar MW which cannot be selected individually by the first mass analyzer.

### CID after IMS without precursor ion selection

For this type of experiment, fragmentation is again performed after IM separation as it was previously described, but now no precursor ion selection occurs. This type of experiment is only possible since IMS represents a second dimension of separation allowing assigning fragment ions to their corresponding precursor ions by means of the same drift time. Therefore ion fragmentation for identification does not only work for selected precursor ion windows, but for larger  $m/z$  ranges as well. For a standard of 1 nmol PC and 500 fmol TOF<sup>2</sup> prepared by sandwich-method, a collision energy in the Transfer TWIG of 100 V was chosen, but no precursor ion window was selected. Further was the IMS Gas Flow set to 48.5 ml/min, the IMS Wave Velocity to 1 225 m/s and the IMS Wave Height to 40 V. The result is a complicated DriftScope-graph (Figure 54), making interpretation even more difficult. Nevertheless for specific drift times, e.g. 62 bins and 94 bins, specific fragment ions can be observed. These regions can be selected and mass spectra with the corresponding ions are generated (see Figure 55 and Figure 57).

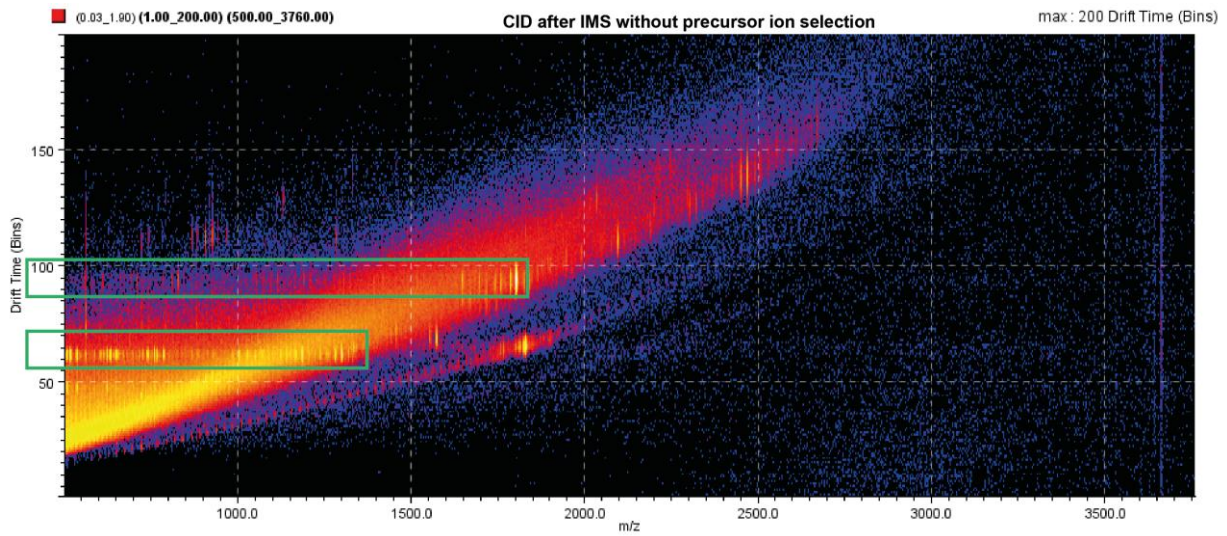


Figure 54: DriftScope-graph for CID after IMS and no m/z precursor ion window

The ions with a drift time of approx. 62 bins are shown in Figure 55. It shows fragment ions belonging to the precursor ion m/z 1296.7 and by generating a mass list for peaks with a  $S/N \geq 3$ , this precursor ion can be identified as angiotensin 1 by Mascot search with a significant Mascot score of 29 to 17 ( $p < 0.05$ , see Figure 56).

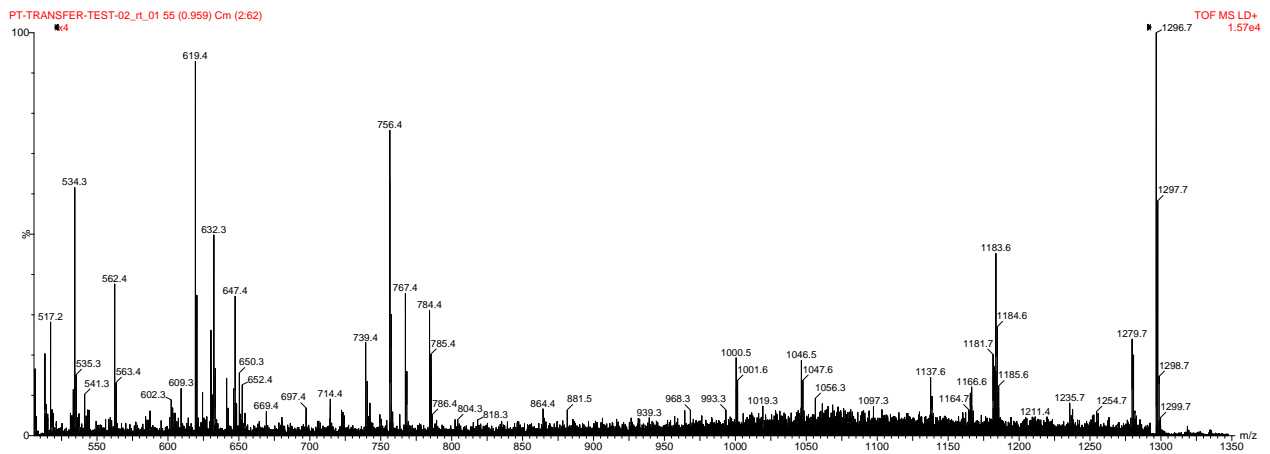


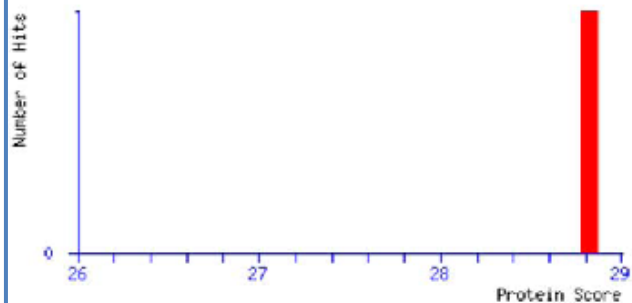
Figure 55: Mass spectrum for selected ions with a drift time of approx. 62bins

# MATRIX SCIENCE Mascot Search Results

User : Max  
 Email : max.kosok@tuwien.ac.at  
 Search title : PT-TRANSFER-TEST-02\_rt\_01  
 Database : NCBI nr 20130830 (32052081 sequences; 11116435548 residues)  
 Timestamp : 2 Sep 2013 at 11:59:07 GMT  
 Protein hits : [gi|2133747](#) angiotensin I - horn fly (fragment)

## Mascot Score Histogram

Ions score is  $-10 \cdot \log(P)$ , where P is the probability that the observed match is a random event.  
 Individual ions scores  $> 17$  indicate identity or extensive homology ( $p < 0.05$ ).  
 Protein scores are derived from ions scores as a non-probabilistic basis for ranking protein hits.



## Peptide Summary Report

1. [gi|2133747](#) Mass: 1296 Score: 29 Matches: 1(1) Sequences: 1(1)  
 angiotensin I - horn fly (fragment)  
 Check to include this hit in error tolerant search

Query	Observed	Mr (expt)	Mr (calc)	Delta	Miss	Score	Expect	Rank	Unique	Peptide
<input checked="" type="checkbox"/> <u>1</u>	1296.7000	1295.6927	1295.6775	0.0152	0	29	0.0037	1	U	-.DRVYIHPFHL.-

Figure 56: Mascot search result for selected fragment ions with a drift time of approx. 62bins

The ions with a drift time of approx. 94 bins are shown in Figure 57. It shows fragment ions belonging to the precursor ion  $m/z$  1800.9 and by generating a mass list for peaks with a  $S/N \geq 3$ , this precursor ion can be identified as angiotensinogen fragment 1-40 by Mascot search showed a significant score of 17 to 8 ( $p < 0.05$ , see Figure 58), which is the same as N-acetyl-renin.

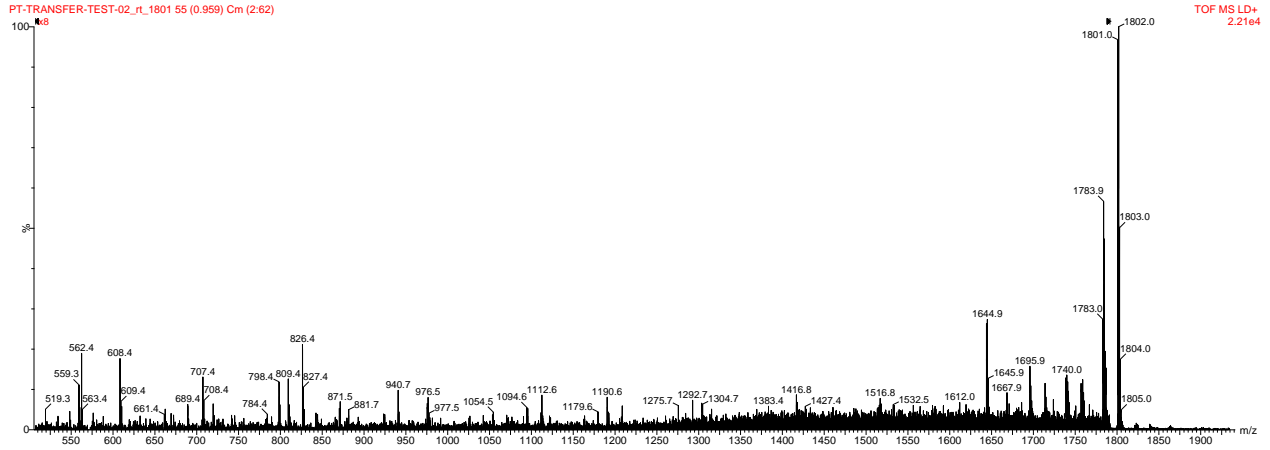


Figure 57: Mass spectrum for selected ions with a drift time of approx. 94bins

## Mascot Search Results

**User** : Max  
**Email** : max.kosok@tuwien.ac.at  
**Search title** : PT-TRANSFER-TEST-02\_rt\_1801  
**Database** : SwissProt 2013\_08 (540732 sequences; 192091492 residues)  
**Timestamp** : 2 Sep 2013 at 11:52:19 GMT  
**Protein hits** : [ANGT\\_HORSE](#) Angiotensinogen (Fragment) OS=Equus caballus GN=AGT PE=1 SV=1

### Mascot Score Histogram

Ions score is  $-10 \cdot \log(P)$ , where P is the probability that the observed match is a random event.  
 Individual ions scores  $> 8$  indicate identity or extensive homology ( $p < 0.05$ ).  
 Protein scores are derived from ions scores as a non-probabilistic basis for ranking protein hits.

### Peptide Summary Report

1. [ANGT\\_HORSE](#) Mass: 1800 Score: 17 Matches: 1(1) Sequences: 1(1)  
 Angiotensinogen (Fragment) OS=Equus caballus GN=AGT PE=1 SV=1  
 Check to include this hit in error tolerant search

Query	Observed	Mr(expt)	Mr(calc)	Delta	Miss	Score	Expect	Rank	Unique	Peptide
<input checked="" type="checkbox"/> <a href="#">1</a>	1800.9000	1799.8927	1799.9359	-0.0432	0	17	0.021	1	U	-.DRVYIHPFLLLVYS.-

Figure 58: Mascot search result for selected fragment ions with a drift time of approx. 94bins

This experiment proved that CID ion fragmentation after IM separation without ion precursor window selection allows to separate and identify ions in just one experiment as it is a valuable approach for MS imaging experiments.

### 3.2.3 Mass Sensitivity for Ion Mobility

After evaluation of IM parameters and finding optimized settings for good ion mobility separation and transmission efficiency, experiments with peptide and lipid standards of various concentrations were performed to find the lowest possible concentration still detectable with a  $S/N \geq 3$ . For these sensitivity tests, standards were prepared with the mixed-solvent method according to chapter 2.11.1 and measured within a range of  $m/z$  500–2 000 at an IMS Gas Flow of 36 ml/min, an IMS Wave Velocity of 1 225 m/s and an IMS Wave Height of 37 V.

For the single standard of the peptide mixture TOF<sup>2</sup> angiotensin 2  $[M+H]^+_{\text{mono}}$  1 046.5 was chosen as reference compound and a concentration of 1 fmol could still be detected (see Figure 59/a). For the single lipid standards, various LODs were found. Lipids form different kinds of salt adducts, which reduces the sensitivity since different  $m/z$  values are detected. For the CLP ion  $[M+3Na-2H]^+_{\text{mono}}$  1 515.9 the LOD was 50 pmol (see Figure 59/b), for the CBO ion  $[M+Na]^+_{\text{mono}}$  955.8 the LOD was 10 pmol and for PC ion  $[M+H]^+_{\text{mono}}$  902.8 the LOD was 1 pmol. Here it has to be stated, that the samples were applied on an area of about 19.6 mm<sup>2</sup> but data was only acquired for 60 sec and therefore only for a small area of the sample. It therefore has to be considered that the actual LOD could be lower since the formation of analyte “hot spots” could occur (Luxembourg et al. 2003). Further could the sensitivity for lipids have been improved using different matrix systems or adhesives (Zhou et al. 2010), however this was not performed since it was aimed to establish a standardized method for IM-MS imaging experiments.

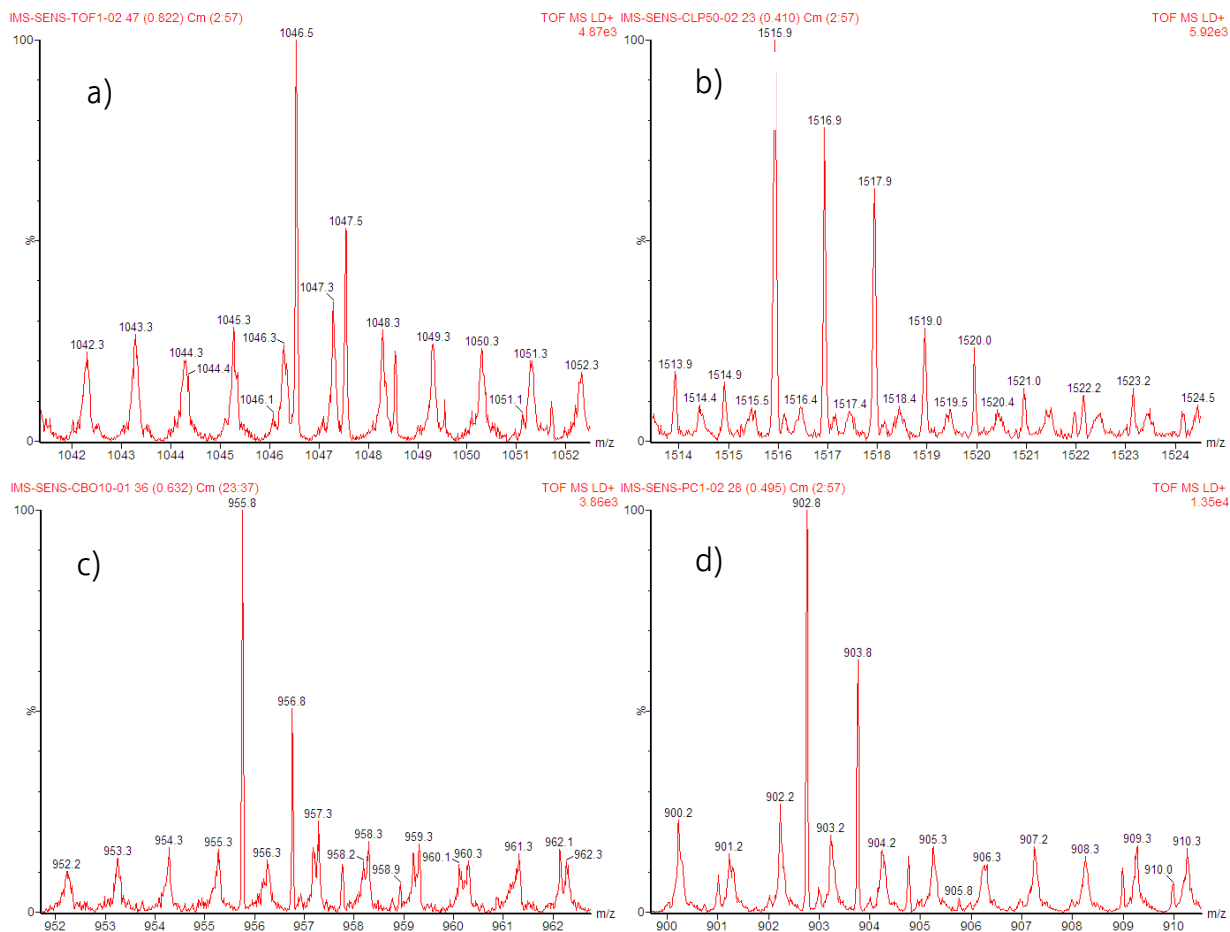


Figure 59: LOD for IM MS; a) 1 fmol TOF<sup>2</sup>, b) 50 pmol CLP, c) 10 pmol CBO, d) 1 pmol PC; m/z 500-2 000, IMS Gas Flow 36 ml/min, IMS Wave Velocity 1 225 m/s, IMS Wave Height 37 V

Since various effects like suppression or adduct formation between different ions can occur, sensitivity also had to be tested for combined standards of peptides and lipids. The sensitivity for peptides was slightly reduced to 10 fmol by the presence of the lipid species, again represented by angiotensin 2  $[M+H]^+_{\text{mono}}$  1 046.5 and the sensitivity for the PC ion  $[M+H]^+_{\text{mono}}$  902.9 was reduced to 4 pmol. The other two lipid species CBO and CLP seemed to influence each other differently from preparation to preparation. CBO could always be detected down to concentrations of 28 pmol, while in some cases CLP could even be detected with an increased LOD of 20 pmol while in other cases higher concentrations of CLP could not be detected at all. For those samples, where higher concentrations of CLP could not be detected, CBO always showed increased signal intensity. This effect probably results from varying formation of different salt adducts for the CLP and the CBO during crystallization on the target. The consequences of this effect were not further investigated within the extent of this thesis since it should not have an influence on IM-MS imaging experiments of biological tissue.

### 3.2.4 IM-MS Imaging of Peptide/Lipid Standard

After the ion mobility setting optimization and sensitivity evaluation, tests to check the maintenance of ion mobility separation over the length of an MS imaging experiment were performed.

For this, five different standards were applied on the MALDI steel target in a given pattern as shown in Figure 60. The applied standards of 1 nmol CBO, 1 nmol PC, 1  $\mu$ l of PEG (10 mg/ml), 1 nmol CLP and 500 fmol TOF<sup>2</sup> were prepared each according to the mixed-solvent method in chapter 2.11 and the experiment was conducted with an x- and y- laser-step-size of 150  $\mu$ m for a m/z range of 500-2 000, an IMS Gas Flow of 38 ml/min, an IMS Wave Velocity of 1 225 m/s and an IMS Wave Height of 36 V. The lateral distribution of selected analyte specific ions is also shown in Figure 60 representing a successful imaging experiment. This experiment also shows how (in-) homogeneous the analyte co-crystalizes with the matrix, confirming that the tested sensitivities described in chapter 3.2.3 could be lower.

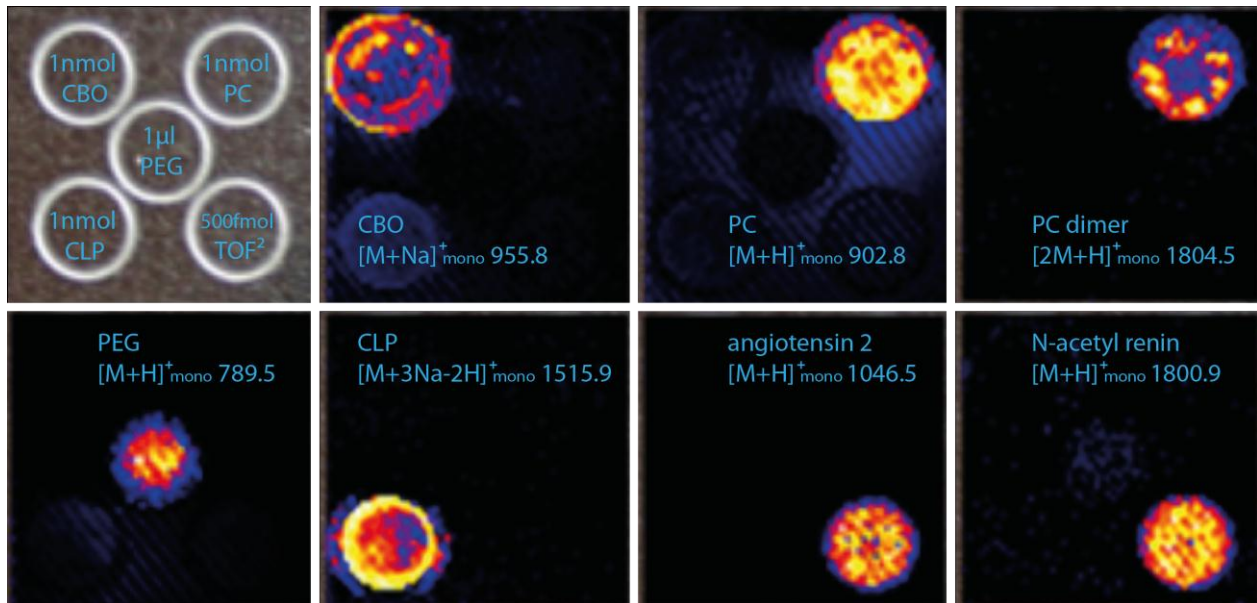


Figure 60: First IM-MS imaging experiment; pattern of applied standards and selected m/z values; 150  $\mu$ m x 150  $\mu$ m lateral resolution

This experiment was performed to prove that ion mobility separation can be maintained for the whole sample (respective tissue) area. Figure 61 therefore shows the DriftScope-graph for all ions that were detected over the whole IM-MS imaging experiment. It can be observed that there are two main classes of detected ions which can be separated by their drift time. One ion class exhibiting shorter drift times and therefore higher ion mobilities can be distinguished from

the other ion class exhibiting longer drift times and therefore lower ion mobilities. To further define those two main classes, the specific areas were selected and mass spectra were generated by accumulating the selected ions. The mass spectrum corresponding to the ion class with longer drift times is shown in Figure 62 and represents mainly lipidic analytes. This confirms the previous observations from chapter 3.2.1 that lipids possess lower ion mobilities compared to peptides and polyethyleneglycol which are mainly shown in Figure 63 representing the mass spectrum for ions with a shorter drift time. Since lipid and peptide species, present on the whole imaging area, can be distinguished in the DriftScope-graph by their drift time, it can be said that ion mobility separation could be maintained for the IM-MS imaging experiment.

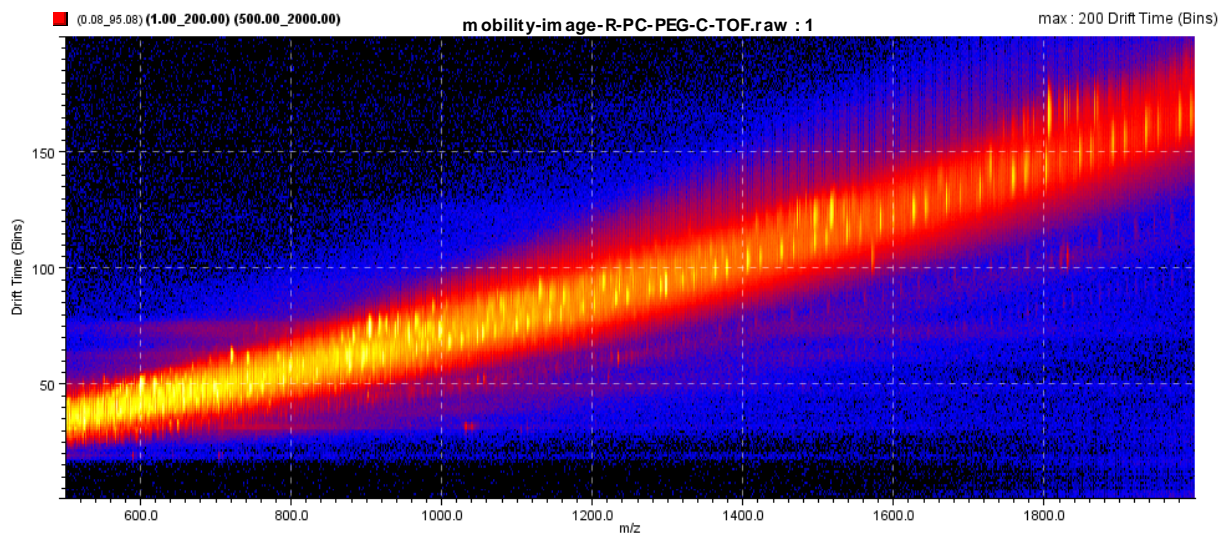


Figure 61: DriftScope-graph for detected ions distributed over the whole area used for imaging

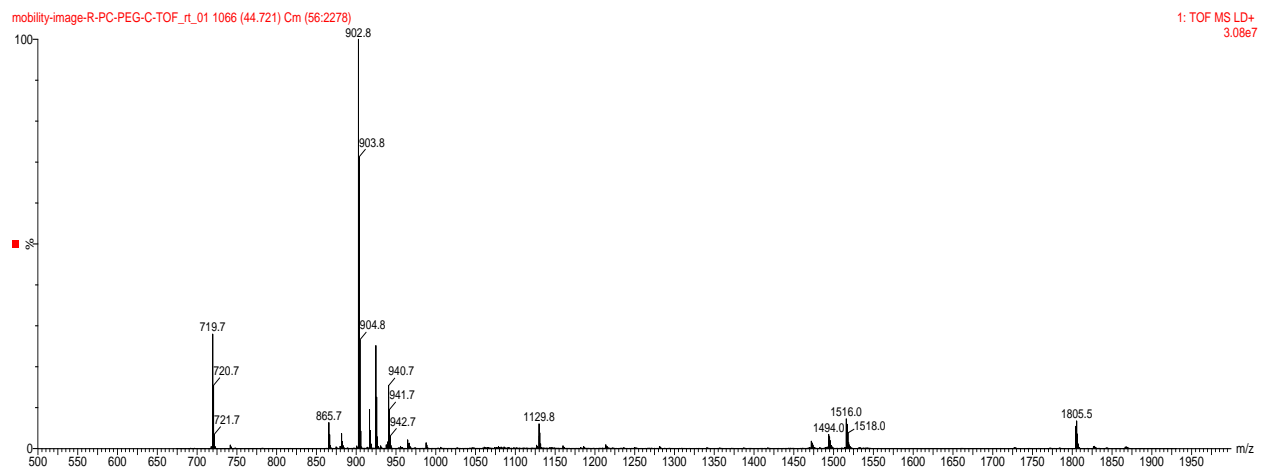


Figure 62: Generated mass spectrum for selected ions from the DriftScope-graph in Figure 61 with longer drift times and therefore lower ion mobilities

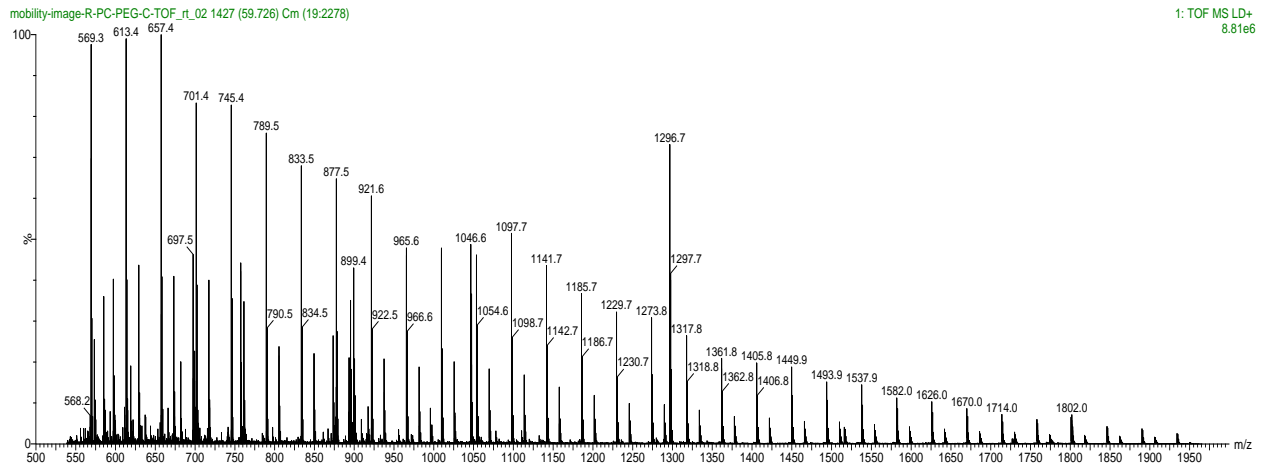


Figure 63: Generated mass spectrum for selected ions from the DriftScope-graph in Figure 61 with shorter drift times and therefore higher ion mobilities

Further, an IM-MS imaging experiment was conducted for a TOF<sup>2</sup> and PC standard on Aclar-film to simulate the bioglue on the film. The PC standard was applied by means of ChIP-printing method in a "+" shape, whereas 100 pmol were printed on each spot using the chemical inkjet printer with a pitch size of 180  $\mu\text{m}$ . The peptide standard (500 fmol of TOF<sup>2</sup>) was applied as a drop on the upper left and the lower right corner of the printed lipid area. Finally the MALDI matrix (see chapter 2.11.2.2) was printed on top of the standards with a pitch size of 180  $\mu\text{m}$ . The printing process had to be aborted due to inconsistent printing behavior, leading to an unknown final matrix concentration. The imaging experiment was conducted with a laser step size of 100  $\mu\text{m}$  x 100  $\mu\text{m}$  for a m/z range of 500-2000, with an IMS Gas Flow of 38 ml/min, an IMS Wave Velocity of 1 225 m/s and an IMS Wave Height of 36 V. In Figure 64, the pattern of the applied standards as well as the lateral distribution of selected analyte specific ions is shown, which illustrates a successful imaging experiment.

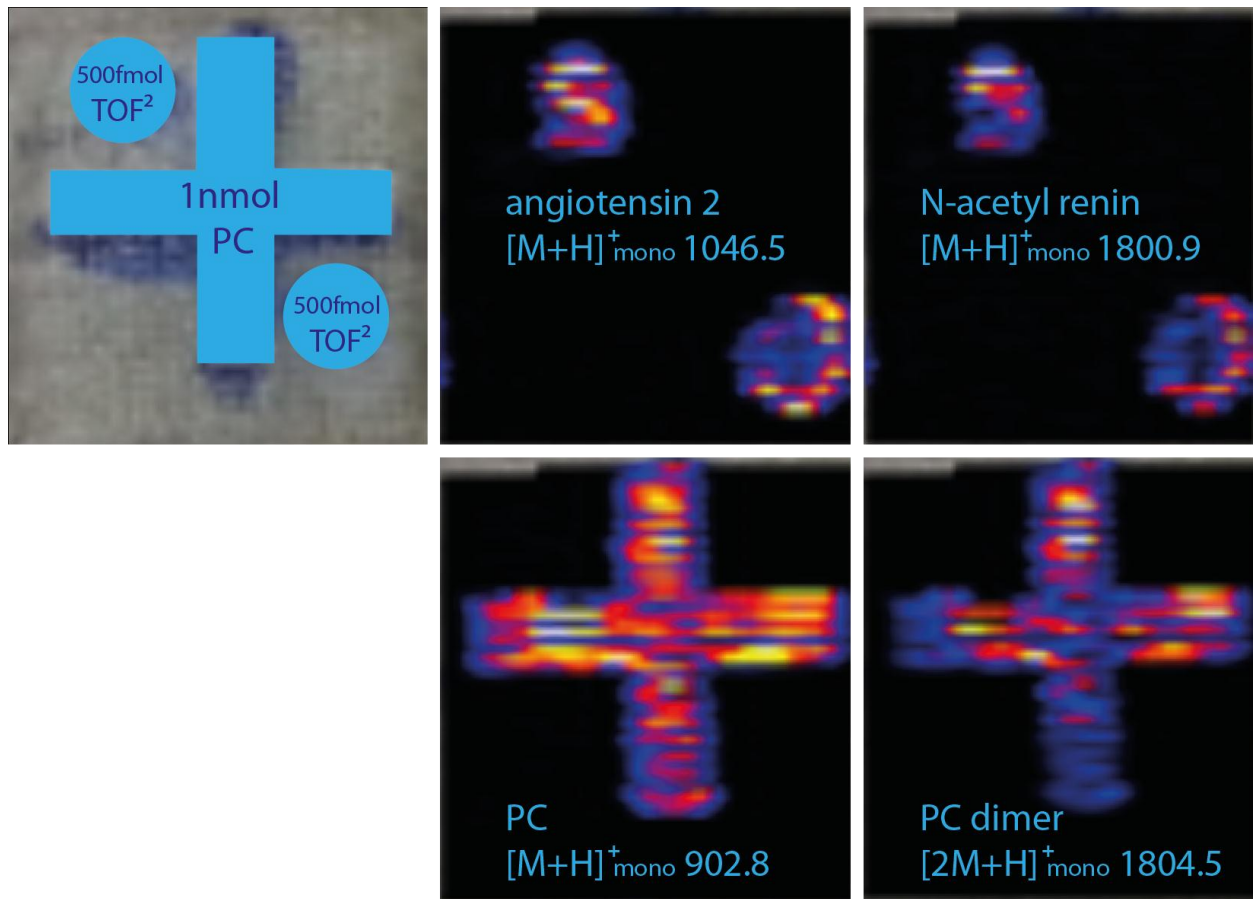


Figure 64: pattern of applied TOF<sup>2</sup> and PC standard on Aclar-film; lateral distribution of selected analyte specific m/z values

Figure 65 shows the DriftScope-graph for all detected ions of the selected area. Different classes of ions with varying drift times can again be distinguished, but not as good as it was observed for previous experiments (Figure 61). Especially for lower drift times, repeated signal cluster of lower intensity were observed, most likely resulting from matrix artifacts. By selecting specific areas of the DriftScope-graph mass spectra of the selected ions were generated. Figure 66 shows the mass spectrum of ions with longer drift times and therefore lower ion mobilities and Figure 67 shows the mass spectrum of ions with shorter drift times and therefore higher ion mobilities. Again lipids and peptides can be distinguished as it was possible for the first IM-MS imaging experiment, but also a lot of different peaks with high intensity can be observed.

These additional detected ions can result from contaminations originating from the printing procedure but this is rather unlikely since the printing method is well established and commonly used. Further could the additional ions represent contaminations and background peaks from

Aclar-film, which is more likely even though the film was cleaned with EtOH prior to standard and matrix application. Since the lipid and the peptide standard can still be distinguished by their drift time, it was shown that ion detection and mobility separation is still possible for samples with intensive, unknown background signals.

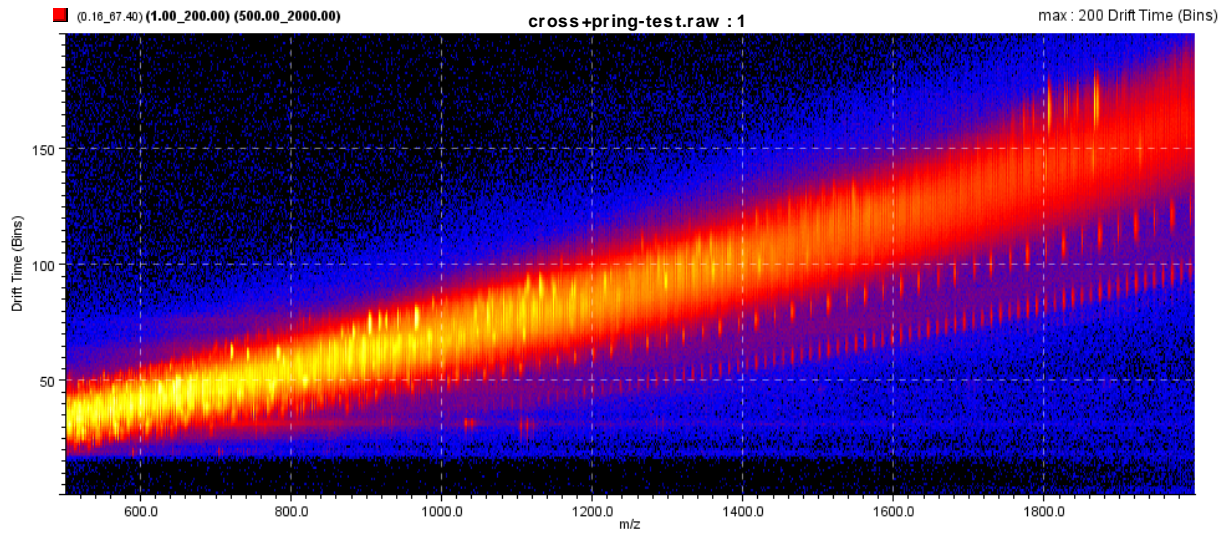


Figure 65: DriftScope-graph for detected ions distributed over the whole area used for imaging

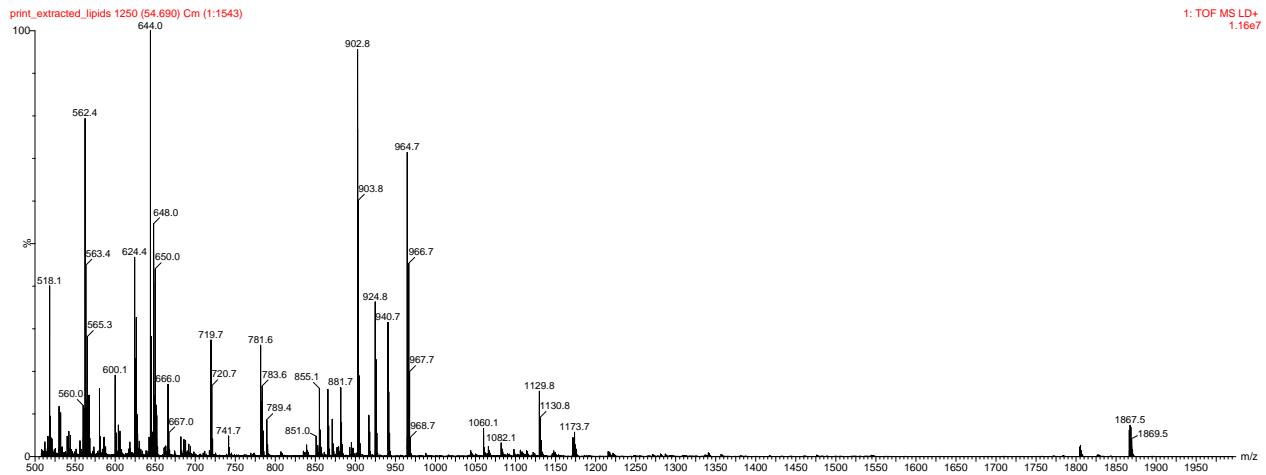


Figure 66: Generated mass spectrum for ions from the DriftScope-graph in Figure 65 with longer drift times and therefore lower ion mobilities; PC ions are present

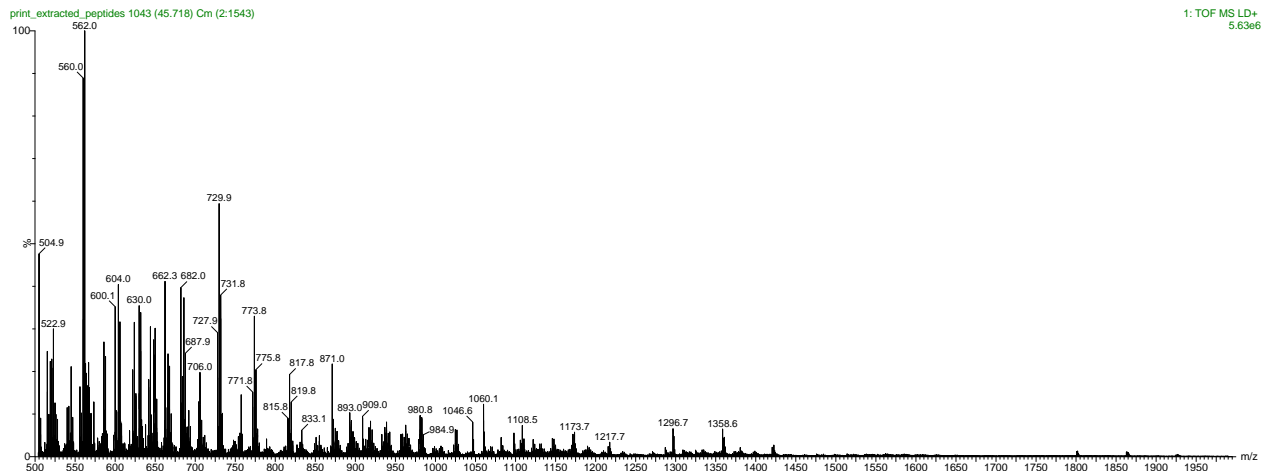


Figure 67: Generated mass spectrum for ions from the DriftScope-graph in Figure 65 with shorter drift times and therefore higher ion mobilities; peptide ions from TOF<sup>2</sup> standard are present

### 3.2.5 IM-MS Imaging of Bioglue

IM-MS imaging experiments were performed on Aclar-film samples which were provided with bioglue from individual *P. shermani* specimen. An area of approximately 1 cm<sup>2</sup> from the Aclar-1 sample with a high density of bioglue was excised with sterile scissors and fixed on an ITO glass slide with double sided conductive tape. Matrix was applied on the glue by means of CHIP printing in steps of 180 μm with a final concentration of 40 ng α-CHCA and 40 ng DHB per spot. The experiment was conducted with an x- and y- laser-step-size of 180 μm for a m/z range of 500-2 500, an IMS Gas Flow of 36 ml/min, an IMS Wave Velocity of 1 225 m/s and an IMS Wave Height of 35 V. Light microscopic images of the printed matrix spots are shown in Figure 68. Figure 68/a represents the sample before the imaging experiment. It can be observed that matrix did not form uniformly crystallized spots on the bioglue surface. In contact with liquids, the bioglue forms a kind of hydrogel that was observed in chapter 3.1.1, it therefore appears as if the matrix solution is absorbed and crystallization on the glue surface prevented (Figure 68/b). The sample surface after the imaging experiment is displayed in Figure 68/c. It seems that matrix crystals disappeared from positions where no glue was present, but the glue surface itself, showing initially almost no matrix crystallization, seemed to be burned by the laser. This could represent caramelization, indicating the presence of carbohydrates or exopolysaccharides. For such analytes, α-CHCA is the wrong matrix system for sufficient ionization. Further did the experiment only result in one ion with a S/N ≥ 3 (m/z 666.0). The lateral distribution of this ion is shown in Figure 68/d where it can be observed that this ion is only detected where no bioglue was present. From the large number of proteins present in the bioglue which was observed in chapter 3.1 (Figure 29), the bioglue's

composition is assumed to be very complex resulting in ion suppression or effects during the desorption process in the ion source, leading to non-detectable neutral molecules.

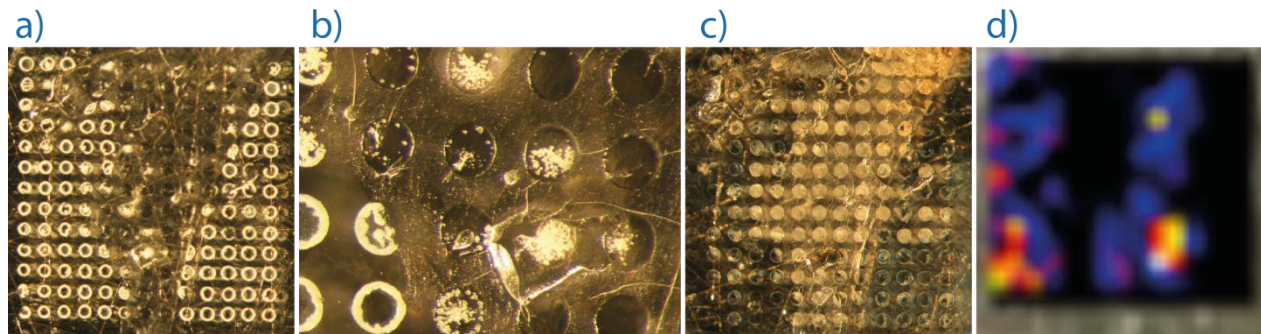


Figure 68: IM-MS Image of Aclar-1 sample; a) light microscopic image before IM-MS imaging, b) light microscopic image after IM-MS imaging

Since matrix application by ChIP printing did not result in good crystallization on the bioglue material, a new IM-MS imaging experiment was conducted where  $\alpha$ -CHCA matrix was applied by means of Airbrush technique (see chapter 2.11.2.2). Again an area with a high density of bioglue was excised with sterile scissors followed by matrix application (see Figure 69/a). During the spraying process the glue seemed to soak up the matrix solution but a light microscopic image showed that matrix crystals were formed on the glue's surface (see Figure 69/b). The IM-MS imaging experiment was conducted with an x- and y- laser-step-size of  $180 \times 180 \mu\text{m}$  for a m/z range of 500-3760, an IMS Gas Flow of 26 ml/min, an IMS Wave Velocity of 1133 m/s and an IMS Wave Height of 37 V. The sample surface after the imaging experiment is shown in Figure 69/c, where it can be observed that the matrix crystals vanished but the bioglue surface also seemed to have been burned by the laser like it was the case for the previous experiment.

Again ions could only be detected where no bioglue is present, they are assumed to be matrix cluster, since they are of low m/z values. An exemplary ion distribution is shown in Figure 69/d for m/z 664.6.

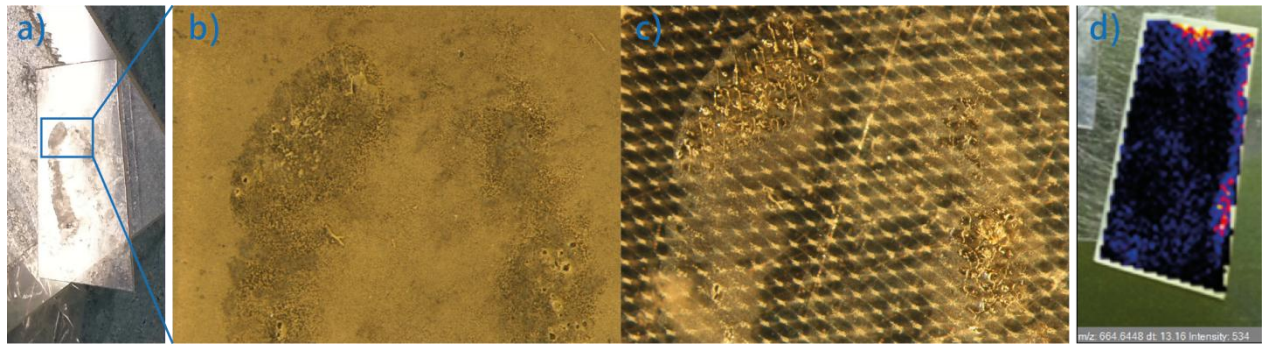


Figure 69: Bioglue on Aclar-film; a) excised area of Aclar-1 sample, b) matrix crystallization on bioglue, c) bioglue after imaging experiment

Three more IM-MS imaging experiments on samples of Aclar-1 were conducted again with matrix application by airbrush method, whereas the matrix was dissolved in ACN/0.1% TFA/isopropanol (1/1/1) in order to hopefully dissolve lipid species. Those three experiments further differed in the applied laser power of 220, 300 and 350 to test if ion destruction occurs due to too high laser power. Unfortunately the results were almost the same. No ions could be detected on the bioglue surface which only did not look burned after the experiment for a laser power of 220. Light microscopic images of the samples surfaces after the imaging experiments and exemplary lateral ion distributions for each sample are shown in Figure 70.

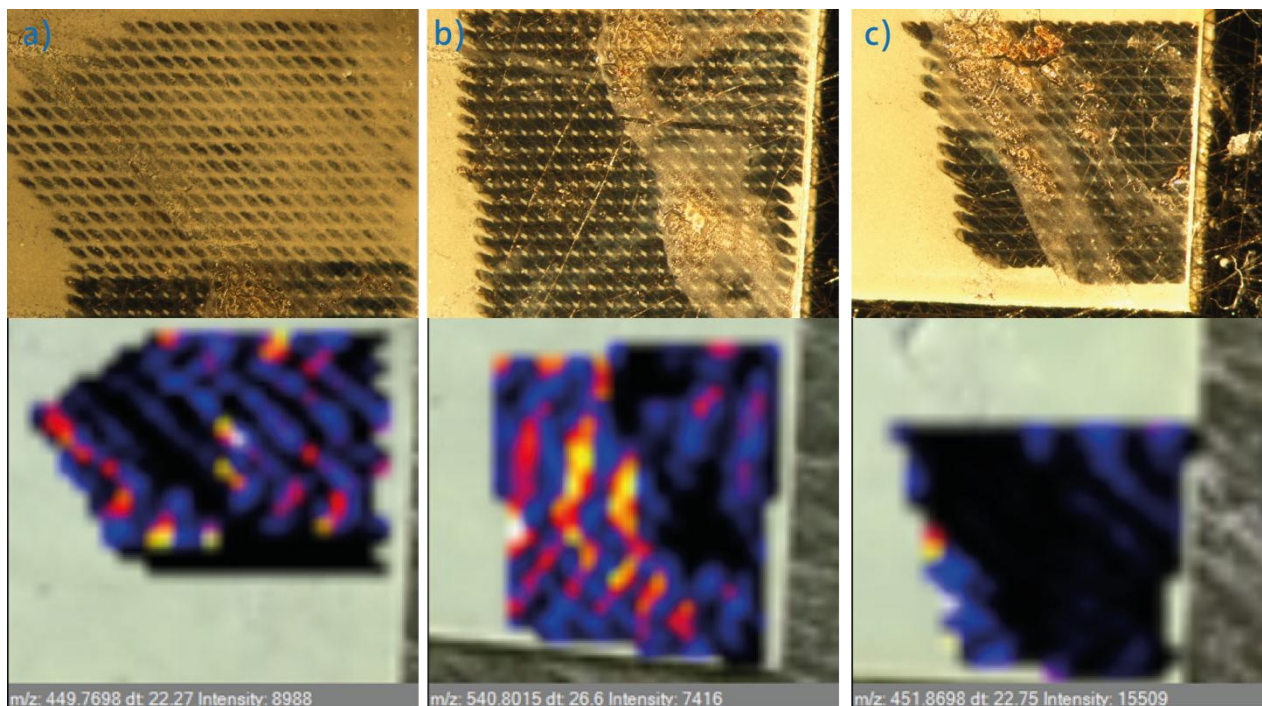


Figure 70: Light microscopic images of bioglue samples on Aclar-film after IM-MS imaging experiment and exemplary lateral distribution of detected ions; a) laser power 220, b) laser power 300, c) laser power 350

The reduced laser power of 220 appears to be too low to desorb and ionize the analyte molecules of the bioglue, but a laser power of 300 appears to be too high and probably results in the destruction of analyte molecules.

Further experiments were conducted on Aclar-1 sample using the UltrafleXtreme MALDI-TOF instrument by Bruker Daltonics (Bremen, Germany) whereas matrix dissolved in ACN/0.1% TFA/isopropanol (1/1/1) was applied by means of airbrush method. Unfortunately here again, independently from the used laser energy no  $m/z$  with a  $S/N \geq 3$  could be detected.

So far, the preliminary results obtained by Sophie Fröhlich<sup>1)</sup> regarding identified analytes of the bioglue by direct MALDI-MS analysis could not be repeated. Reasons for this maybe sample aging and therefore degraded, relevant analytes, or instrumentation issues (experiments were not repeated on the same instrument, an AXIMA TOF<sup>2)</sup>), or methodological errors. To rule out the latter, further investigation for direct analysis of the bioglue regarding laser power as well as the used matrix systems should be conducted, but where not performed within this thesis. However, the latter issue was addressed by other tissue samples.

### 3.2.6 IM-MS Imaging of Tissue Samples

To see if the optimized ion mobility settings for imaging experiments yield good results for biological tissue samples as well, a 10  $\mu\text{m}$  thin sagittal mouse brain cryo-section was used (see Figure 72/a). The sample was kindly provided on an ITO glass slide by Dr. Balazs Hegedus<sup>4)</sup> and prepared according to the washing procedure in chapter 2.11.2.1. The matrix  $\alpha$ -CHCA was mixed with aniline and applied by means of airbrush technique (see chapter 2.11.2.2). The IM-MS imaging experiment was conducted with an x- and y- laser-step-size of 170 x 170  $\mu\text{m}$  for a  $m/z$  range of 500-3 760, an IMS Gas Flow of 26 ml/min, an IMS Wave Velocity of 1 133 m/s and an IMS Wave Height of 35 V.

Processing the recorded data to analyze the lateral distribution of the main monoisotopic ions and their corresponding drift time with the software HDImaging by Waters (Manchester, UK) resulted in the following graphs in Figure 71. Figure 71/a represents the TIC normalized mass spectrum of the main detected monoisotopic ions whereas the majority has a  $m/z$  value of below 1 000. Figure 71/b represents the correlation between the detected ions and their drift time. It can be observed that there are many ions with same or similar  $m/z$  values but different drift times. A closer look into the ions with lower  $m/z$  values allows differentiating three groups

---

<sup>4)</sup> Head of Translational Thoracic Oncology Lab Anna Spiegel Center of Translational Research Department of Thoracic Surgery Medical University of Vienna, Austria

of ions (see Figure 71/c). The ions which are marked in red possess short drift times and in respect to their lateral distribution it could be observed that they mostly consist of matrix signals since they are located outside the tissue as it is shown for the exemplary  $m/z$  749.7 in Figure 72/b. This observation allows us to distinguish and eliminate matrix peaks by their short drift times. The ions marked in green possess longer drift times and almost all of those ions have similar lateral distribution on the mouse brain tissue, which could be the Cerebellum (see exemplary  $m/z$  602.5 and 840.8 in Figure 72/c/d). It can be assumed that those ions are of a similar ion class, probably a specific class of lipids since they have a kind of linear drift time correlation. The ions marked in blue seemed to consist again of two groups but cannot be differentiated so well. The ions of the blue group with a shorter drift time seem to be more evenly distributed over the tissue area like the most intense ion  $m/z$  666.0 or  $m/z$  855.0 (see Figure 72/e/f). According to previous observations in chapter 3.2.1 and 3.2.4, those ions could be peptide species whereas ions of the blue group with longer drift times could already be lipid species. Those ions are also mainly distributed in a region of the brain tissue which could be the Cerebrum. One of those ions is  $m/z$  760.5, which is a common MW for lipids and its lateral distribution is shown in Figure 72/g.

Further could ions of higher MW ( $m/z$  1 293.7,  $m/z$  1 802.0 and  $m/z$  1 833.9) be observed with a more defined lateral distribution (see Figure 72/h/i/j).

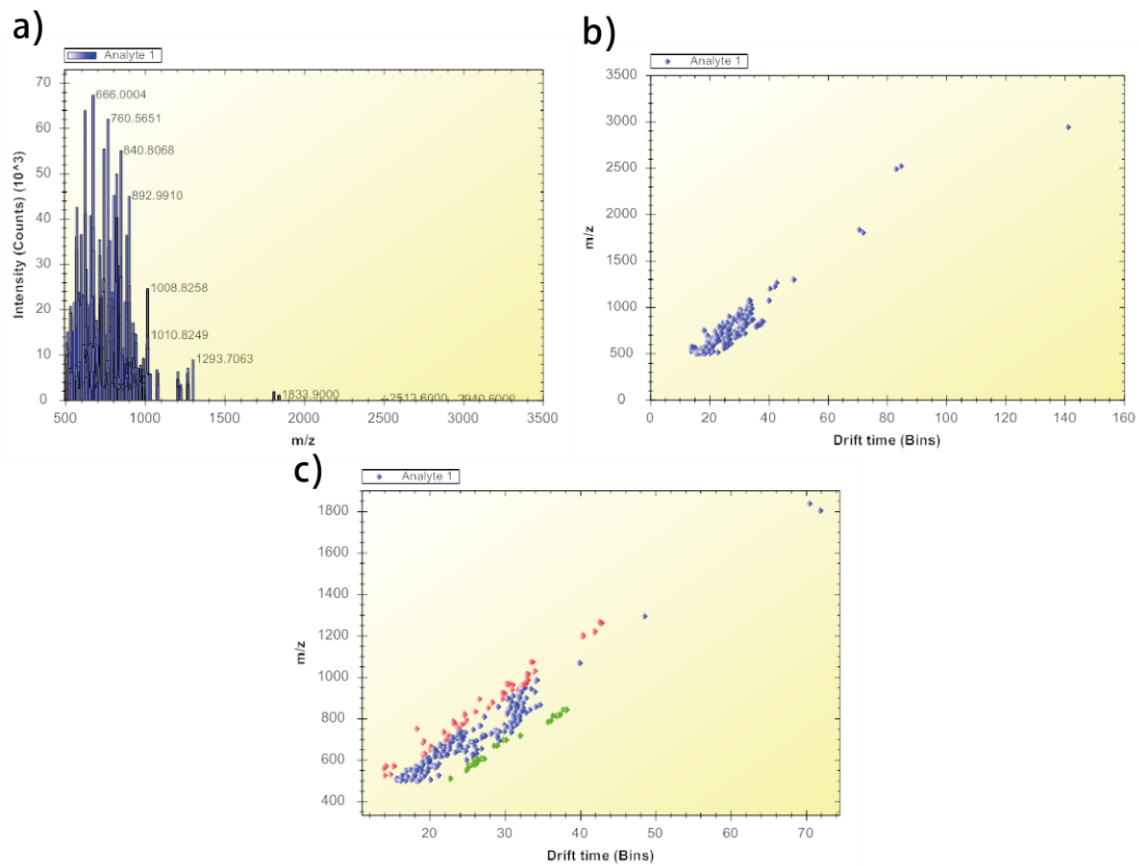


Figure 71: Processed data of IM-MS imaging of mouse brain tissue using the Synapt G2 HDMS; a) TIC normalized mass spectrum of main monoisotopic ions, b) simplified DriftScope-graph for main monoisotopic ions, c) ions with lower m/z values differentiated in three groups

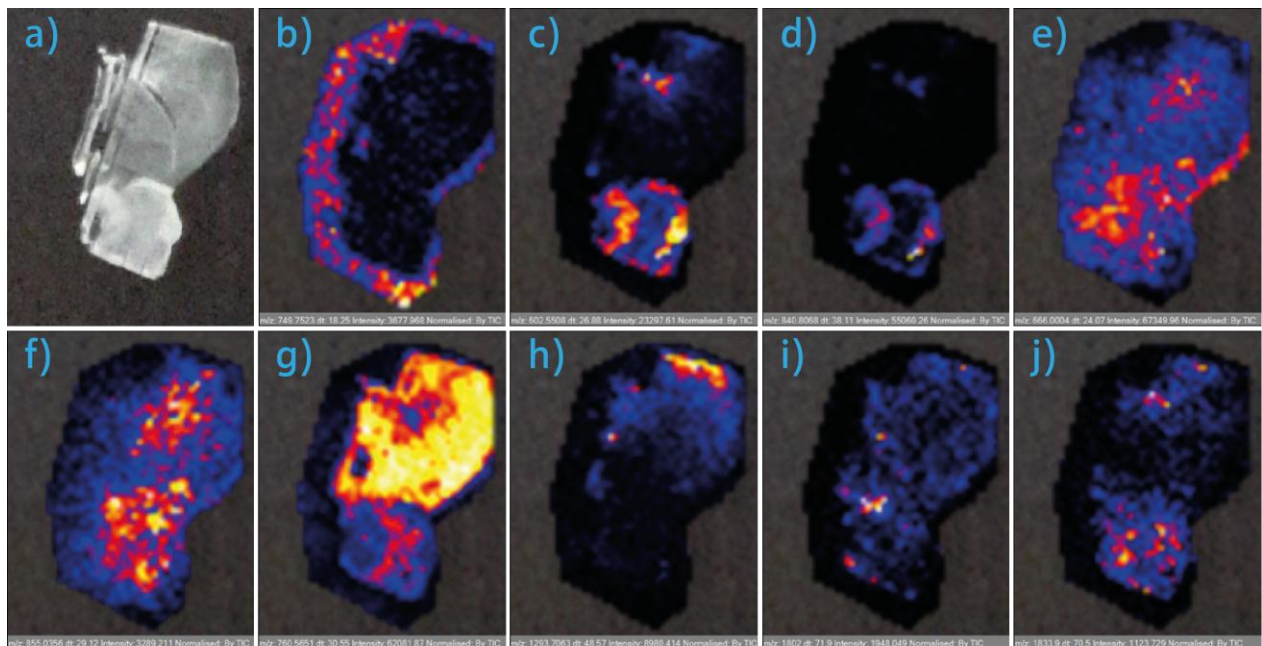


Figure 72: IM-MS imaging experiment using the Synapt G2 HDMS; a) sagittal mouse brain cryo-section; lateral ion distribution: b) m/z 749.7, c) m/z 602.5, d) 840.8, e) m/z 666.0, f) m/z 855.0, g) m/z 760.5, h) m/z 1 293.7, i) m/z 1 802.0, j) m/z 1 833.9

Some of the provided sagittal mouse brain cryo-sections were also analyzed by means of a standard MS imaging experiment by Mathias Holzlechner<sup>1)</sup> using the UltrafleXtreme by Bruker Daltonics (Bremen, Germany) whereas the same matrix system was applied (yet unpublished data). Figure 73 shows the applied matrix and its crystallization as well as the lateral distribution of the ion  $m/z$  1833.9, which has a similar distribution compared to the IM-MS imaging experiment performed with the Synapt G2 HDMS (see Figure 72/j).

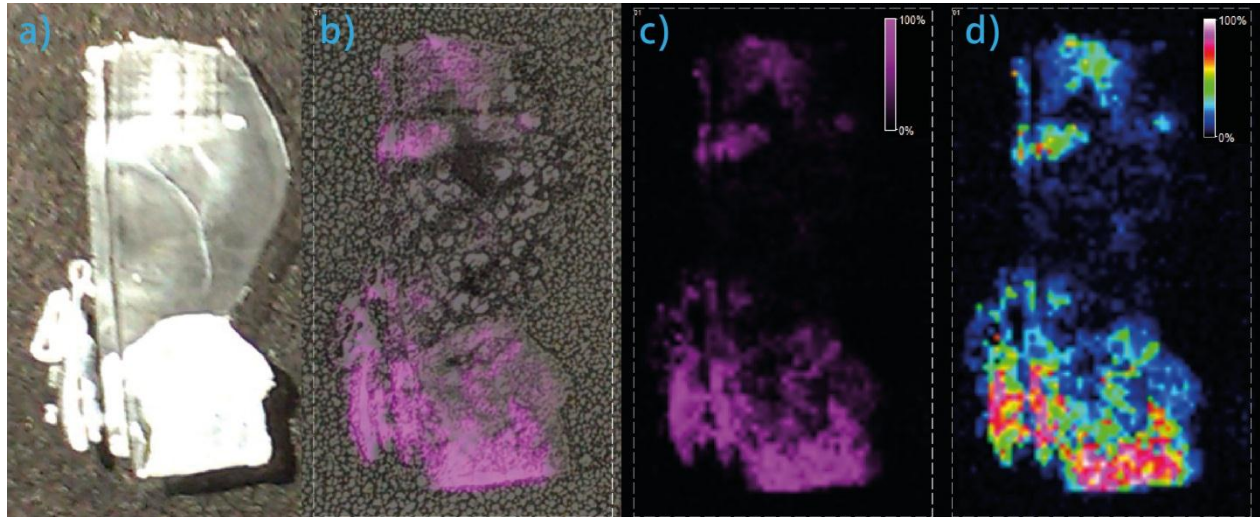


Figure 73: MS imaging experiment using the UltrafleXtreme; a) sagittal mouse brain cryo-section, b) applied matrix by means of airbrush and lateral distribution of  $m/z$  1833.9; c) lateral distribution of  $m/z$  1833.9 with single color intensity scheme; d) lateral distribution of  $m/z$  1833.9 with multi-color intensity scheme

In summary it can be said that IM-MS imaging on biological sample is possible and the results can be compared to standard MS Imaging experiments obtained from different instruments. Further does additional information about ion drift time allow to distinguish different analyte classes like matrix and peptides and in case of lipids, it seems to be possible to distinguish different lipid species as well.

Next steps should include IM-MS imaging experiments in combination with fragmentation studies to identify selected ions whereas ion mobility separation after fragmentation helps to distinguish fragment ions coming from isobaric precursor ions, or precursor ions with similar  $m/z$  values like it was shown in chapter 3.2.2.

### *P. shermani* skin gland tissue

The Triwave device settings were evaluated and for optimized parameters it was shown that IM-MS imaging can be successfully performed on biological tissue samples to gain additional information on the lateral ion distribution which helps to evaluate the results. 10  $\mu\text{m}$  thin cryo-sections of skin glands from *P. shermani* were therefore provided by Janek von Byern<sup>2)</sup> to perform an IM-MS imaging experiment to gain information about the distribution of proteins and lipids within the three different kinds of glands, the granular gland (GG) the modified granular gland (MGG) and the mucous gland (MG) which were described in chapter 1.1.

In order to detect proteins and lipids in a similar way, the tissue washing procedure from chapter 2.11.2.1 was modified according to Seeley et al. (2008). The ITO glass slide with the tissue samples, which was stored at  $-20\text{ }^{\circ}\text{C}$  was placed in a falcon with 40 ml of 70% EtOH at  $-20\text{ }^{\circ}\text{C}$  for 30 sec and afterwards placed in a vacuum desiccator for 5 min. As second washing step for 30 sec was then performed in 40 ml of 70% EtOH/10% acetic acid at room temperature followed by storage in a vacuum desiccator. Matrix application of  $\alpha$ -CHCA was performed with the airbrush method and the experiment was conducted with an x- and y- laser-step-size of  $150 \times 150\text{ }\mu\text{m}$  for a m/z range of 450-3 760, an IMS Gas Flow of 26 ml/min, an IMS Wave Velocity of 1 133 m/s and an IMS Wave Height of 38 V.

Various light microscopic images of the cryo-sections are shown in Figure 74, whereas Figure 74/a shows the skin glands on the ITO glass slide after cryo-cutting. The small mucous glands can easily be distinguished from granular and modified granular glands. Latter can only be differentiated after naphthol yellow and PAS staining (see chapter 1.1). Figure 74/b shows a similar tissue region after the washing procedure, here the glands cannot be clearly distinguished and it appears that some parts were accidentally removed during washing. The matrix crystallization after application by Airbrush is shown in Figure 74/c and Figure 74/d shows the same tissue area after the IM-MS imaging experiment. The individual laser spots, shown in Figure 74/d, can be clearly distinguished, and therefore it is obvious that the laser spot size is too large to resolve the individual gland types. Parts of the black tissue further appear to be burned by the laser, which probably again represents caramelization and indicates carbohydrates and exopolysaccharides (see chapter 3.2.5).

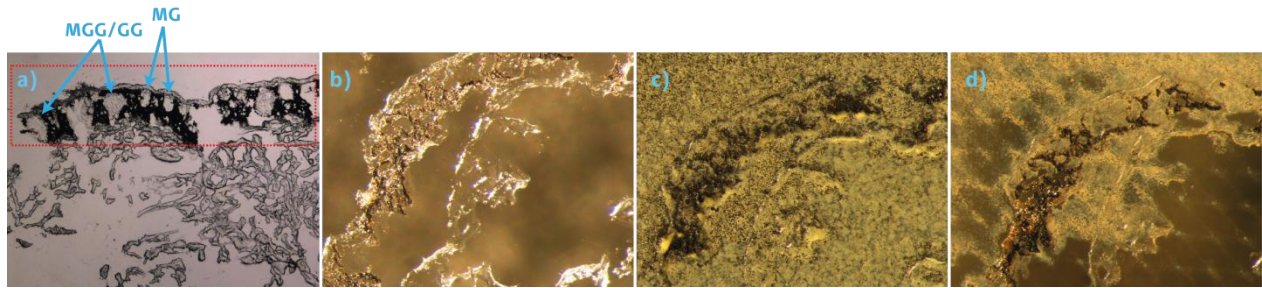


Figure 74: Light microscopic images of skin tissue cryo-sections; a) after cutting with gland assignment, b) after washing, c) after matrix application, d) after MALDI laser ablation

An overview of the whole tissue area after matrix application is shown in Figure 75/a, the epithelium with the glands can be observed in black and the rest of the biological tissue is located to the right. The sample structure observed to the left as well as above and below of the epithelium (Figure 75/a) did not show staining with PAS (Figure 75/b) which was performed by Janek von Byern<sup>2)</sup> after the IM-MS imaging experiment and therefore is assumed to results from Tissue-Tek<sup>®</sup> (tissue stabilizing agent), which was used to embed the sample. This has to be kept in mind since contaminations could have occurred during the cryo-cutting process.

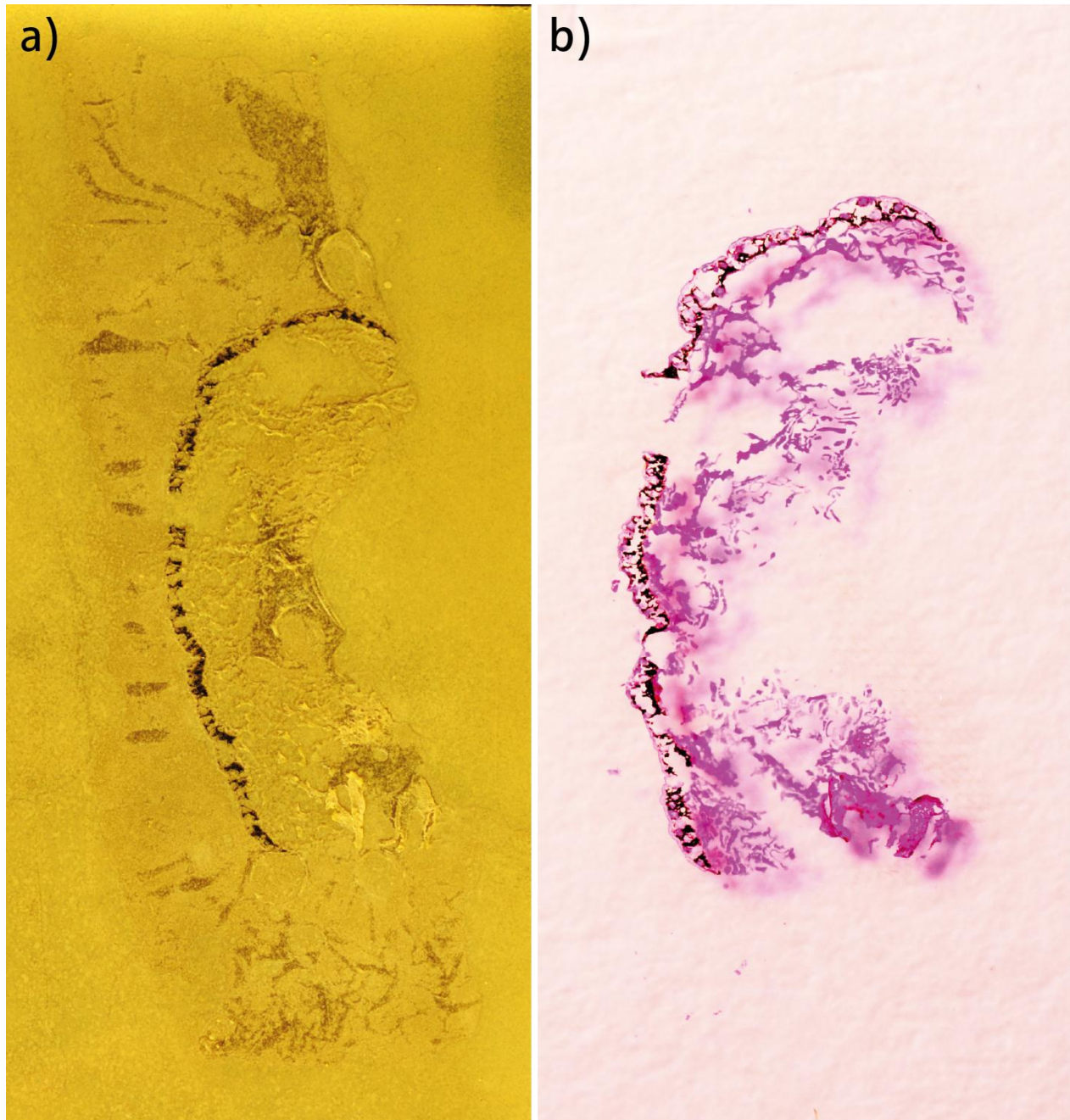


Figure 75: *P. shermani* skin tissue: a) cryo-section after matrix application by airbrush; b) PAS staining after IM-MS imaging experiment and matrix removal

Processing the recorded data with HDImaging to analyze the lateral distribution of the main monoisotopic ions and their corresponding drift time resulted in the graphs represented in Figure 76. Figure 76/a represents the TIC normalized mass spectrum of the main detected monoisotopic ions whereas no ions were detected above  $m/z$  of approx. 1300. Figure 76/b represents the correlation between the detected ions and their drift time. It can be observed that there are many ions with same or similar  $m/z$  values but different drift times, as well as that

all the detected ions have drift times below 40 bins. Compared to the observations regarding the correlation between the drift time- and lateral-distribution for the mouse brain tissue, no such distinctive correlation can be observed for the salamander skin tissue. Only the red marked ions in Figure 76/b, which are kind of grouped together, show the same lateral distribution on the tissue (see Figure 77/h). These ions also hold the highest intensities.

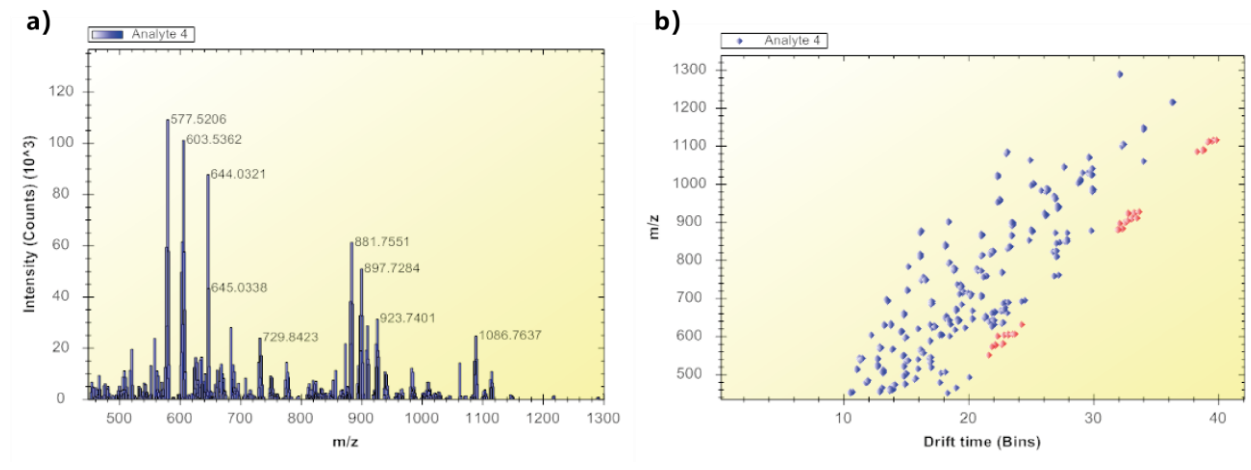


Figure 76: Processed data of IM-MS imaging of *P. shermani* skin tissue; a) TIC normalized mass spectrum of main monoisotopic ions, b) simplified DriftScope-graph for main monoisotopic ions

The lateral distributions of selected  $m/z$  values that appear to represent tissue characteristics are shown in Figure 77 as well as an image of the whole tissue section after MALDI laser ablation (Figure 77/a). On areas which apparently inhabit no biological sample and no Tissue-Tek, the matrix disappeared completely, this correlates with the distribution of  $m/z$  560.0 (Figure 77/b). The epithelium appears to be represented by the  $m/z$  values 464.4, 694.5 and 850.9 (Figure 77/c/d/e) whereas the  $m/z$  values 639.4 and 822.5 occur left and right of the epithelium and could represent Tissue-Tek contaminations (Figure 77/f/g).

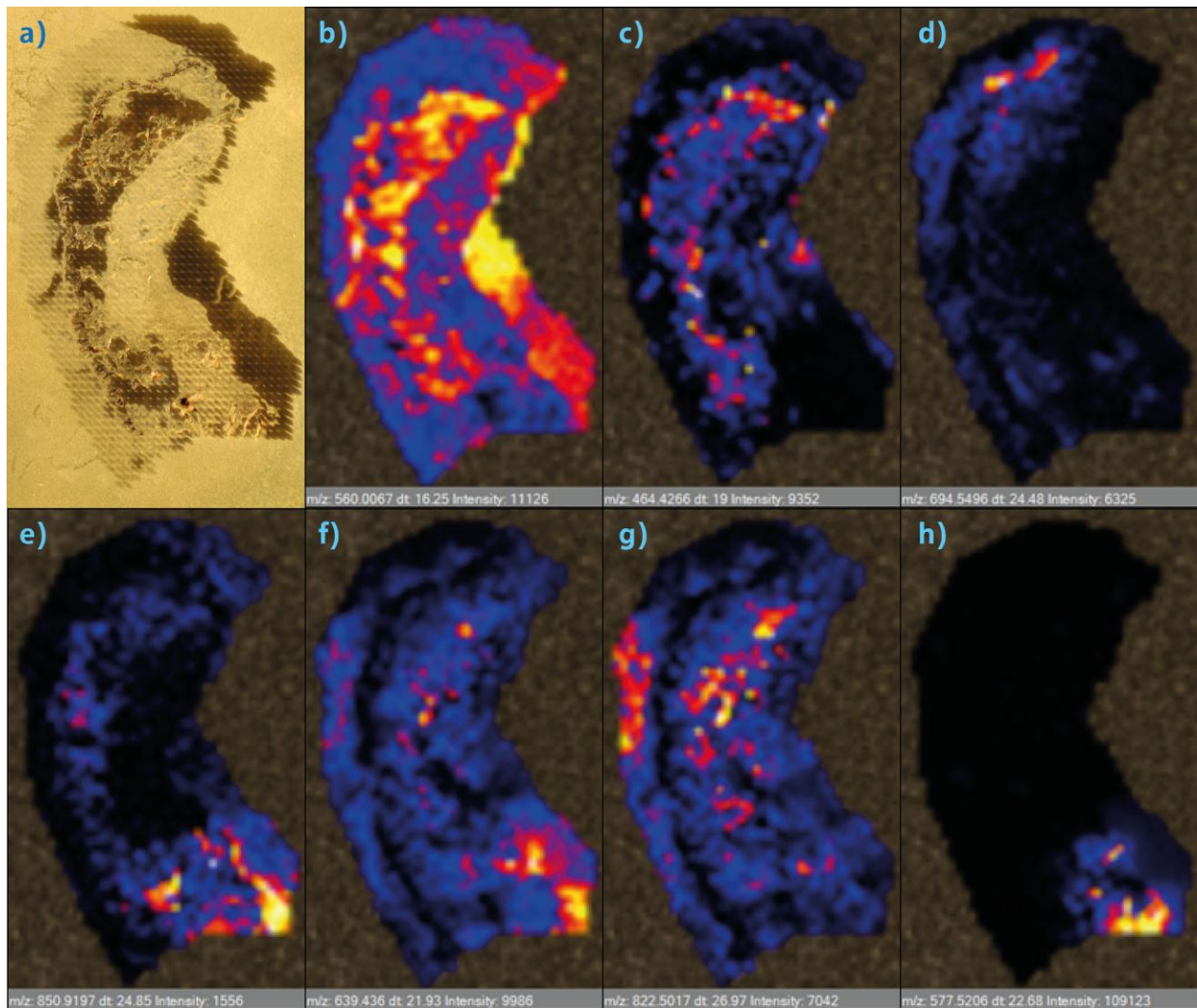


Figure 77: a) Tissue section after MALDI laser ablation; lateral distribution of: b)  $m/z$  560.0, c)  $m/z$  464.4, d)  $m/z$  694.5, e)  $m/z$  850.9, f)  $m/z$  639.4, g)  $m/z$  822.5, h)  $m/z$  577.5

To identify some of the analyte molecules of the skin tissue, a first imaging experiment for CID fragmentation after mobility separation was performed within a  $m/z$  range of 50-1 300, a collision energy in the Transfer TWIG of 90 V, an IMS Gas Flow of 38 ml/min, an IMS Wave Velocity of 1 225 m/s and an IMS Wave Height of 38 V. The DriftScope-graph for all ions of the imaging experiment is shown in Figure 78. It can be observed that the ions are not well resolved according to their drift time and therefore fragment ions cannot be assigned to their corresponding precursor ion. CID fragmentation IM-MS imaging experiments without precursor ion selection therefore have to be further optimized for the future.

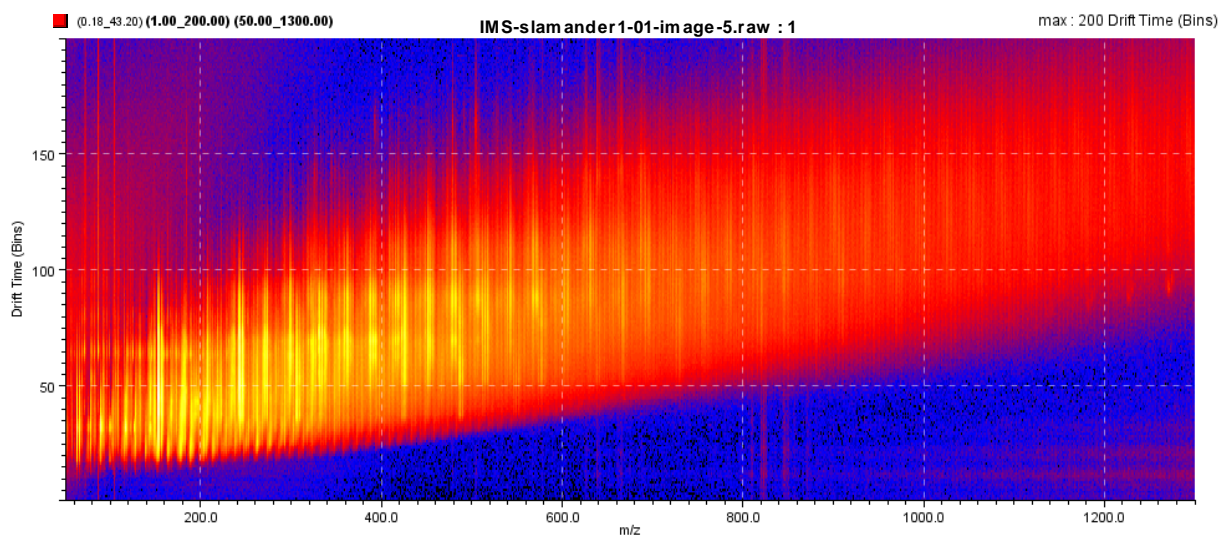


Figure 78: DriftScope-graph of IM-MSMS imaging experiment on salamander skin tissue

### 3.2.7 Summary & Conclusion

The relations between the Triwave device parameters (IMS Gas Flow, IMS Wave Velocity and IMS Wave Height) in order to gain good ion mobility separation and transmission efficiency on the same time, were successfully evaluated. A faster travelling wave is accompanied by a higher travelling wave and a lower gas flow whereas in terms of a constant wave velocity, the gas flow increases with the wave height and *vice versa*. Regarding this correlations it has to be kept in mind, that there are instrumental limitations of a maximum wave height and of course of minimal wave height and minimal gas flow. For an increased gas flow it also has to be considered that transmission efficiency is reduced above a certain pressure and fragmentation processes occur as well.

The evaluation of these parameters also showed their influence on the drift time behavior of lipid and peptide ion species as well as their influence on the drift time resolution. It was shown that lipids possess longer drift times than peptides whereas the drift time differences between the two species increase with reduced wave velocity. Unfortunately the drift time resolution increases with faster waves, therefore the chosen settings have to be considered according to the analytical task. Further it was shown that the parameters are depending on the chosen  $m/z$  range and that ions with smaller  $m/z$  values need faster waves and/or higher gas flows to gain good ion mobility separation.

Another observation was that constant gas pressures in the Triwave device are mandatory to generate reproducible and comparable results. Since the implemented Pirani gauges in the

instrument also have an accuracy of only 15%, it leads to the consequence, that if ion mobility separation is used to determine drift times in order to identify isobaric species like isomers or to distinguish folding states of proteins, always analyte mixtures should be analyzed to maintain the possibility of internal calibration of drift time, especially if only a small drift time difference is expected.

After the Triwave parameters were evaluated and optimized settings for good ion mobility separation and transmission efficiency were found, the sensitivity of the instrument as well as different CID fragmentation modes of the instrument were tested.

For the potential sensitivity of the instrument it was shown that lipids cannot be detected as sensitive as peptides since they tend to form various kinds of salt adducts, which are competing each other. It also was shown, that in fact, the actual possible sensitivity was not tested due to inhomogeneous matrix co-crystallization.

For the CID fragmentation it was shown that fragmentation of a selected precursor ion prior to ion mobility separation allows distinguishing different types of fragment ions as well as isobaric fragment ions. CID fragmentation of selected precursor ions after ion mobility separation was further shown to allow distinguishing fragment ions of isobaric precursor ions, which even was shown to be possible for larger  $m/z$  ranges and therefore allows the simultaneous identification of multiple ions. Unfortunately this last fragmentation mode could not yet be performed successfully for imaging experiments.

For IM-MS imaging experiments it was shown that for optimized parameters, it is possible to maintain ion mobility separation over the whole duration of the experiment and therefore to distinguish ions not only by their lateral distribution, but also by their drift time. This could not only be shown for a pattern of known analyte molecules, but for also unknown analyte molecules on biological tissue samples.

To implement this evaluated method for *P. shermani* samples in order to identify analyte molecules from the bioglue, the dried secret provided on Aclar-film was tried to be analyzed directly, as well to image skin tissue sections with granular and mucous glands where secret might still be present. Unfortunately no reasonable ions could yet be detected with a  $S/N \geq 3$  for the direct analysis of the dried secret. Moreover, it seems that the tissue gets burned by the laser, pointing to the possible presence of carbohydrates and exopolysaccharides. For the skin tissue sample, various analytes with distinct lateral distribution could be found but not yet identified by means of IM-MS/MS imaging. It was also observed that the different types of

glands can at the moment not be distinguished by the chosen instrumental setup, since the laser spot size exceeds the gland diameter.

For future experiment CID fragmentation for IM-MS imaging experiments without precursor ion selection have to be optimized to distinguish fragment and precursor ions. And to directly identify analyte molecules of the bioglue the applied methods also have be optimized in respect of the used laser power, the applied matrix system and the washing protocol for tissue samples.

## 4 References

- Aebersold, R. and M. Mann (2003). "Mass spectrometry-based proteomics." *Nature* **422**(6928): 198-207.
- Arnold, S. J. (1982). "A Quantitative Approach to Antipredator Performance: Salamander Defence against Snake Attack." *Copeia* **1982**(2): 247-253.
- Berlind, T., M. Poksinski, et al. (2010). "Formation and cross-linking of fibrinogen layers monitored with in situ spectroscopic ellipsometry." *Colloids Surf B Biointerfaces* **75**(2): 410-417.
- Biemann, K., C. Cone, et al. (1966). "Determination of the amino acid sequence in oligopeptides by computer interpretation of their high-resolution mass spectra." *J Am Chem Soc* **88**(23): 5598-5606.
- Bjellqvist, B., K. Ek, et al. (1982). "Isoelectric focusing in immobilized pH gradients: principle, methodology and some applications." *J Biochem Biophys Methods* **6**(4): 317-339.
- Brodie, E., Jr. (1983). Antipredator Adaptations of Salamanders: Evolution and Convergence Among Terrestrial Species. Adaptations to Terrestrial Environments. N. S. Margaris, M. Arianoutsou-Faraggitaki and R. J. Reiter, *Springer US*: 109-133.
- Brodie, E. D., L. S. Gibson, et al. (1969). "Defensive behavior and skin glands of the Northwestern Salamander *Ambystoma Gracile*." *Herpetologica* **25**: 187-194.
- Brown, R. S. and J. J. Lennon (1995). "Mass resolution improvement by incorporation of pulsed ion extraction in a matrix-assisted laser desorption/ionization linear time-of-flight mass spectrometer." *Anal Chem* **67**(13): 1998-2003.
- Cha, H. J., J. H. Moon, et al. (2007). "Resolution of infrared matrix-assisted laser desorption/ionization time-of-flight mass spectrometry using glycerol: enhancement with a disperse laser beam." *Rapid Communications in Mass Spectrometry* **21**(8): 1468-1474.
- Chait, B. T. (2006). "Chemistry. Mass spectrometry: bottom-up or top-down?" *Science* **314**(5796): 65-66.
- Cheng, C., M. L. Gross, et al. (1998). "Complete structural elucidation of triacylglycerols by tandem sector mass spectrometry." *Anal Chem* **70**(20): 4417-4426.
- Claude, E., M. Towers, et al. (2012). "Data Independent MALDI Imaging HMDSe for Visualization and Identification of Lipids Directly from a Single Tissue Section." *Waters corporation, Manchester, UK*. Application Note.
- Clauser, K. R., P. Baker, et al. (1999). "Role of accurate mass measurement (+/- 10 ppm) in protein identification strategies employing MS or MS/MS and database searching." *Anal Chem* **71**(14): 2871-2882.
- Cotter, R. J., W. Griffith, et al. (2007). "Tandem time-of-flight (TOF/TOF) mass spectrometry and the curved-field reflectron." *Journal of Chromatography B* **855**(1): 2-13.
- de Hoffmann, E. and V. Stroobant (2007). Mass Analysers. Mass Spectrometry: Principles and Applications, *Wiley & Sons, Ltd.* **3**: 85-174.
- de Hoffmann, E. and V. Stroobant (2007). Tandem Mass Spectrometry. Mass Spectrometry: Principles and Applications, *Wiley & Sons, Ltd.* **3**: 189-216.
- Dreisewerd, K. (2003). "The Desorption Process in MALDI." *Chemical Reviews* **103**(2): 395-426.
- Feldhoff, R., S. Rollmann, et al. (1999). Chemical Analysis of Courtship Pheromones in a Plethodontid Salamander. Advances in Chemical Signals in Vertebrates. R. Johnston, D. Müller-Schwarze and P. Sorensen, *Springer US*: 117-125.
- Flammang, P. (2006). Adhesive Secretions in Echinoderms: An Overview. Biological Adhesives. A. Smith and J. Callow, *Springer Berlin Heidelberg*: 183-206.

- Flammang, P., A. Lambert, et al. (2009). "Polyphosphoprotein-Containing Marine Adhesives." *The Journal of Adhesion* **85**(8): 447-464.
- Giles, K., S. D. Pringle, et al. (2004). "Applications of a travelling wave-based radio-frequency-only stacked ring ion guide." *Rapid Commun Mass Spectrom* **18**(20): 2401-2414.
- Graham, L., V. Glattauer, et al. (2006). An Adhesive Secreted by Australian Frogs of the Genus *Notaden*. *Biological Adhesives*. A. Smith and J. Callow, Springer Berlin Heidelberg: 207-223.
- Graham, L. D., V. Glattauer, et al. (2005). "Characterization of a Protein-based Adhesive Elastomer Secreted by the Australian Frog *Notaden bennetti*." *Biomacromolecules* **6**(6): 3300-3312.
- Graham, L. D., V. Glattauer, et al. (2013). "The adhesive skin exudate of *Notaden bennetti* frogs (*Anura: Limnodynastidae*) has similarities to the prey capture glue of *Euperipatoides* sp. velvet worms (*Onychophora: Peripatopsidae*)." *Comparative Biochemistry and Physiology Part B: Biochemistry and Molecular Biology* **165**(4): 250-259.
- Gross, J. and K. Strupat (1998). "Matrix-assisted laser desorption/ionisation-mass spectrometry applied to biological macromolecules." *TrAC Trends in Analytical Chemistry* **17**(8-9): 470-484.
- Hoaglund, C. S., S. J. Valentine, et al. (1998). "Three-dimensional ion mobility/TOFMS analysis of electrosprayed biomolecules." *Anal Chem* **70**(11): 2236-2242.
- Kanu, A. B., P. Dwivedi, et al. (2008). "Ion mobility-mass spectrometry." *J Mass Spectrom* **43**(1): 1-22.
- Karas, M., U. Bahr, et al. (1989). "UV laser matrix desorption/ionization mass spectrometry of proteins in the 100 000 dalton range." *International Journal of Mass Spectrometry and Ion Processes* **92**(0): 231-242.
- Karas, M. and R. Krüger (2003). "Ion Formation in MALDI: The Cluster Ionization Mechanism." *Chemical Reviews* **103**(2): 427-440.
- Kaufmann, R. (1995). "Matrix-assisted laser desorption ionization (MALDI) mass spectrometry: a novel analytical tool in molecular biology and biotechnology." *Journal of Biotechnology* **41**(2-3): 155-175.
- Keckes, J., I. Burgert, et al. (2003). "Cell-wall recovery after irreversible deformation of wood." *Nat Mater* **2**(12): 810-814.
- Kiss, A. and R. A. Heeren (2011). "Size, weight and position: ion mobility spectrometry and imaging MS combined." *Analytical and Bioanalytical Chemistry* **399**(8): 2623-2634.
- Koenig, T., B. H. Menze, et al. (2008). "Robust prediction of the MASCOT score for an improved quality assessment in mass spectrometric proteomics." *J Proteome Res* **7**(9): 3708-3717.
- Kollipara, L. and R. P. Zahedi (2013). "Protein carbamylation: in vivo modification or in vitro artefact?" *Proteomics* **13**(6): 941-944.
- Kussmann, M., E. Nordhoff, et al. (1997). "Matrix-assisted Laser Desorption/Ionization Mass Spectrometry Sample Preparation Techniques Designed for Various Peptide and Protein Analytes." *Journal of Mass Spectrometry* **32**(6): 593-601.
- Laemmli, U. K. (1970). "Cleavage of structural proteins during the assembly of the head of bacteriophage T4." *Nature* **227**(5259): 680-685.
- Largen, W. and S. K. Woodley (2008). "Cutaneous Tail Glands, Noxious Skin Secretions, and Scent Marking in a Terrestrial Salamander (*Plethodon shermani*)." *Herpetologica* **64**(3): 270-280.
- Lee, B., J. Dalsin, et al. (2006). Biomimetic Adhesive Polymers Based on Mussel Adhesive Proteins. *Biological Adhesives*. A. Smith and J. Callow, Springer Berlin Heidelberg: 257-278.
- Leinonen, R., F. G. Diez, et al. (2004). "UniProt archive." *Bioinformatics* **20**(17): 3236-3237.

- Lottspeich, F. and J. W. Engels (2009). Elektrophoretische Verfahren. *Bioanalytik, Spektrum Akademischer Verlag Heidelberg* 2009. **2**: 235-268.
- Lottspeich, F. and J. W. Engels (2009). Massenspektrometrie. *Bioanalytik, Spektrum Akademischer Verlag Heidelberg* 2009. **2**: 329-372.
- Luxembourg, S. L., L. A. McDonnell, et al. (2003). "Effect of local matrix crystal variations in matrix-assisted ionization techniques for mass spectrometry." *Anal Chem* **75**(10): 2333-2341.
- Mamyrin, B. A. (2001). "Time-of-flight mass spectrometry (concepts, achievements, and prospects)." *International Journal of Mass Spectrometry* **206**(3): 251-266.
- Mann, M. and G. Talbo (1996). "Developments in matrix-assisted laser desorption/ionization peptide mass spectrometry." *Current Opinion in Biotechnology* **7**(1): 11-19.
- McDaniel, E. W., D. W. Martin, et al. (1962). "Drift Tube-Mass Spectrometer for Studies of Low-Energy Ion-Molecule Reactions." *Review of Scientific Instruments* **33**(1): 2-7.
- McDonnell, L. A. and R. M. Heeren (2007). "Imaging mass spectrometry." *Mass Spectrom Rev* **26**(4): 606-643.
- McLean, J. A., W. B. Ridenour, et al. (2007). "Profiling and imaging of tissues by imaging ion mobility-mass spectrometry." *J Mass Spectrom* **42**(8): 1099-1105.
- Overberg, A., M. Karas, et al. (1990). "Matrix-assisted infrared-laser (2.94  $\mu$ m) desorption/ionization mass spectrometry of large biomolecules." *Rapid Communications in Mass Spectrometry* **4**(8): 293-296.
- Papayannopoulos, I. A. (1995). "The interpretation of collision-induced dissociation tandem mass spectra of peptides." *Mass Spectrometry Reviews* **14**(1): 49-73.
- Perkins, D. N., D. J. Pappin, et al. (1999). "Probability-based protein identification by searching sequence databases using mass spectrometry data." *Electrophoresis* **20**(18): 3551-3567.
- Philips, B. and R. Shine (2007). "When Dinner is Dangerous: Toxic Frogs Elicit Species-Specific responses from Generalist Snake Predator." *The American Naturalist* **170**(6): 936-942.
- Pittenauer, E. and G. Allmaier (2009). "The renaissance of high-energy CID for structural elucidation of complex lipids: MALDI-TOF/RTOF-MS of alkali cationized triacylglycerols." *J Am Soc Mass Spectrom* **20**(6): 1037-1047.
- Pittenauer, E. and G. Allmaier (2011). "A universal product ion nomenclature for [M-H]<sup>-</sup>, [M+H]<sup>+</sup> and [M+nNa-(n $\times$ 1)H]<sup>+</sup> (n=1-3) glycerophospholipid precursor ions based on high-energy CID by MALDI-TOF/RTOF mass spectrometry." *International Journal of Mass Spectrometry* **301**(1-3): 90-101.
- Pringle, S. D., K. Giles, et al. (2007). "An investigation of the mobility separation of some peptide and protein ions using a new hybrid quadrupole/travelling wave IMS/oa-ToF instrument." *International Journal of Mass Spectrometry* **261**(1): 1-12.
- Rischka, K., K. Richter, et al. (2010). Bio-inspired Polyphenolic Adhesives for Medical and Technical Applications. *Biological Adhesive Systems*. J. Byern and I. Grunwald, *Springer Vienna*: 201-211.
- Roepstorff, P. and J. Fohlman (1984). "Proposal for a common nomenclature for sequence ions in mass spectra of peptides." *Biomed Mass Spectrom* **11**(11): 601.
- Saltz, R., D. Sierra, et al. (1991). "Experimental and clinical applications of fibrin glue." *Plast Reconstr Surg* **88**(6): 1005-1015; discussion 1016-1007.
- Santos, L. F., A. H. Iglesias, et al. (2010). "Traveling-wave ion mobility mass spectrometry analysis of isomeric modified peptides arising from chemical cross-linking." *J Am Soc Mass Spectrom* **21**(12): 2062-2069.
- Schwartz, S. A., R. J. Weil, et al. (2005). "Proteomic-based prognosis of brain tumor patients using direct-tissue matrix-assisted laser desorption ionization mass spectrometry." *Cancer Res* **65**(17): 7674-7681.

- Seeley, E. H., S. R. Oppenheimer, et al. (2008). "Enhancement of protein sensitivity for MALDI imaging mass spectrometry after chemical treatment of tissue sections." *J Am Soc Mass Spectrom* **19**(8): 1069-1077.
- Shevchenko, A., M. Wilm, et al. (1996). "Mass spectrometric sequencing of proteins silver-stained polyacrylamide gels." *Anal Chem* **68**(5): 850-858.
- Shvartsburg, A. A. and R. D. Smith (2008). "Fundamentals of Traveling Wave Ion Mobility Spectrometry." *Anal Chem* **80**(24): 9689-9699.
- Stauber, J., L. MacAleese, et al. (2010). "On-tissue protein identification and imaging by MALDI-ion mobility mass spectrometry." *J Am Soc Mass Spectrom* **21**(3): 338-347.
- Stoeckli, M., D. Staab, et al. (2007). "Compound and metabolite distribution measured by MALDI mass spectrometric imaging in whole-body tissue sections." *International Journal of Mass Spectrometry* **260**(2-3): 195-202.
- Stults, J. T. (1995). "Matrix-assisted laser desorption/ionization mass spectrometry (MALDI-MS)." *Current Opinion in Structural Biology* **5**(5): 691-698.
- Tseng, Y. C., Y. Tabata, et al. (1990). "In vitro toxicity test of 2-cyanoacrylate polymers by cell culture method." *J Biomed Mater Res* **24**(10): 1355-1367.
- Turß, R. (1978). Gewebekleber in der Ophthalmologie. Kunststoffimplantate in der Ophthalmologie. W. Jaeger, J.F. Bergmann-Verlag. **75**: 181-191.
- Tyler, M. (2010). Adhesive Dermal Secretions of the Amphibia, with Particular Reference to the Australian Limnodynastid Genus Notaden. Biological Adhesive Systems. J. Byern and I. Grunwald, Springer Vienna: 181-186.
- Waters (2007). "Synapt HDMS - Theory." Waters corporation, Manchester, UK. Theory.
- Waters (2008). "Synapt MS - Customer Training Presentation." Waters corporation, Manchester, UK. Customer Training Presentation.
- Waters (2009). "Synapt Mobility - Customer Training." Waters corporation, Manchester, UK. Customer Training.
- Waters (2009). "Water Synapt G2 High Definition Mass Spectrometry." Waters corporation, Manchester, UK. Operator's Overview and Maintenance Guide.
- Waters (2010). "Water Synapt G2 MALDI-MS." Waters corporation, Manchester, UK. Operator's Overview and Maintenance Guide.
- Waters (2011). "Imaging G1 acquisition setup." Waters corporation, Manchester, UK. Acquisition Setup.
- Wiley, W. C. and I. H. McLaren (1955). "Time-of-Flight Mass Spectrometer with Improved Resolution." *The Review of Scientific Instruments* **26**(12): 1150-1157.
- Wilkins, M. R., K. L. Williams, et al. (1997). Proteome Research: New Frontiers in Functional Genomics, Springer.
- Williams, C. R., E. D. brodie Jr., et al. (2000). "Antipredator mechanisms of Australian frogs." *Journal of Herpetology* **34**(3): 431-443.
- Winkler, C., K. Denker, et al. (2007). "Silver- and Coomassie-staining protocols: detection limits and compatibility with ESI MS." *Electrophoresis* **28**(12): 2095-2099.
- Wisniewski, J. R., A. Zougman, et al. (2009). "Universal sample preparation method for proteome analysis." *Nat Meth* **6**(5): 359-362.
- Zhou, P., E. Altman, et al. (2010). "Study of matrix additives for sensitive analysis of lipid A by matrix-assisted laser desorption ionization mass spectrometry." *Appl Environ Microbiol* **76**(11): 3437-3443.